ΠΑΝΕΠΙΣΤΗΜΙΟ ΠΕΙΡΑΙΩΣ

UNIVERSITY OF PIRAEUS

Πανεπιστήμιο Πειραιώς,
Σχολή Τεχνολογιών Πληροφορικής και Επικοινωνιών,
Τμήμα Ψηφιακών Συστημάτων

Διδακτορική Διατριβή

Αξιολόγηση της Επίδοσης Επίγειων και Εναέριων Δικτύων Επικοινωνιών

Χαράλαμπος Αρμενιάκος

July 24, 2024

ΠΑΝΕΠΙΣΤΗΜΙΟ ΠΕΙΡΑΙΩΣ

UNIVERSITY OF PIRAEUS

University of Piraeus
School of Information and Communication Technologies
Department of Digital Systems

PHD Thesis

Performance Evaluation of Terrestrial and Aerial Communication Networks

Charalampos K. Armeniakos

Advisory Committee

Athanasios G. Kanatas (Supervisor)
Professor
University of Piraeus

George Efthymoglou
Professor
University of Piraeus

Aggeliki Alexiou
Professor
University of Piraeus

Approval Sheet

University of Piraeus
School of Information and Communication Technologies
Department of Digital Systems

This is to certify that the Dissertation presented by Charalampos K. Armeniakos, entitled “Performance Evaluation of Terrestrial and Aerial Communication Networks”, submitted in fulfillment of the requirement for the degree of Doctor of Philosophy, complies with the regulation of the University of Piraeus and meets the accepted standards with respect to originality.

Dissertation Committee

Athanasios G. Kanatas (Supervisor)
Professor
University of Piraeus

George Efthymoglou
Professor
University of Piraeus

Aggeliki Alexiou
Professor
University of Piraeus

George K. Karagiannidis
Professor
Aristotle University of Thessaloniki

Petros S. Bithas
Associatiate Professor
National and Kapodistrian University of Athens

Konstantinos Maliatsos
Assistant Professor
University of Aegean

Demosthenes Vouyioukas
Associatiate Professor
University of Piraeus

Αξιολόγηση της Επίδοσης Επίγειων και Εναέριων Δικτύων Επικοινωνιών

Χαράλαμπος Αρμενιάκος

(Περίληψη)

Καθώς μεταβαίνουμε με γοργούς ρυθμούς προς την εποχή δικτύων 6ης γενιάς, γίνεται περισσότερο προφανές ότι ένα βασικό χαρακτηριστικό της νέας αυτής εποχής θα είναι η αδιάκοπτη συνδεσιμότητα τόσο για τους χρήστες όσο και για συσκευές τύπου μηχανών για την υποστήριξη μιας πληθώρας εφαρμογών. Για την επίτευξη του στόχου αυτού, η ακαδημαϊκή και η βιομηχανική κοινότητα στρέφεται προς επίκαιρες τεχνολογίες όπως η μικροκυματική ζώνη συχνοτήτων και τα μη επανδρωμένα εναέρια οχηματα. Ωστόσο, η εισαγωγή αυτών των τεχνολογιών έρχεται αντιμέτωπη με ορισμένες προκλήσεις. Προκειμένου να αντιμετωπιστούν αυτές οι προκλήσεις και να προταθούν λύσεις για το σχεδιασμό των κυψελωτών δικτύων 6ης γενιάς, απαιτείται λεπτομερής αξιολόγηση της επίδοσης σε επίπεδο συστήματος, η οποία είναι και ο στόχος της παρούσας διατριβής.
Η ολοκληρωμένη αξιολόγηση της επίδοσης των επίγειων δικτύων στη μικροκυματική ζώνη συχνοτήτων,προϋποθέτει ότι οι χρήστες και οι σταθμοί βάσης είναι εξοπλισμένοι με κεραίες ικανές να σχηματίσουν κατευθυντικούς λοβούς. Ωστόσο, με την εισαγωγή των δυνατοτήτων διαμόρφωσης του λοβού ακτινοβολίας και το αναπόφευκτο σφάλμα σκόπευσης, είναι προφανές ότι και οι δύο πολικές συντεταγμένες πρέπει τώρα να ληφθούν από κοινού υπόψη στη πολιτική συσχέτισης του χρήστη με κάποιο σταθμό βάσης καθώς και στην αξιολόγηση της επίδοσης του δικτύου. Αρχικά, στην παρούσα διατριβή, λαμβάνονται υπόψη οι πολικές συντεταγμένες των σταθμών βάσης και εξάγονται σε αναλυτική μορφή η συνάρτηση πυκνότητας πιθανότητας της μέγιστης λαμβανόμενης ισχύος καθώς και ο μετασχηματισμός Laplace της συνολικής ισχύος των παρεμβολών. Ακολούθως, εκμεταλλευόμενοι θεμελιώδη εργαλεία της στοχαστικής γεωμετρίας, διεξάγεται υπολογισμός της πιθανότητας κάλυψης. Η μελέτη της πιθανότητας κάλυψης διεξάγεται για λόγους πληρότητας για ακόμα δύο ακόμα πολιτικές ζεύξης μεταξύ του δέκτη και του σταθμού βάσης που τον εξυπηρετεί, δηλ. ένα ιδανικό σενάριο αναφοράς και μία πολιτική που βασίζεται αμιγώς στη γωνιακή απόσταση. Προκειμένου να αποτυπωθεί και η επίδραση ενός ισχυρού παρεμβολέα στην επίδοση των δικτύων μικροκυματικής ζώνης συχνοτήτων, πραγματοποιείται αξιολόγηση της επίδοσης υπό την προσέγγιση ενός ισχυρού παρεμβολέα για κάθε προτεινόμενη πολιτική. Σαν σενάριο αναφοράς, ορίζεται ένα πεπερασμένο δίκτυο που λειτουργεί στη μικροκυματική ζώνη συχνοτήτων και επιπλέον υπάρχει τέλεια ευθυγράμμιση μεταξύ των κεραιών του δέκτη και του σταθμού βάσης που τον εξυπηρετεί. Στη περίπτωση αυτή, προκειμένου να εξαχθούν επιπρόσθετα συμπεράσματα σε επίπεδο συστήματος, παρουσιάζονται τρία βασικά σενάρια παρεμβολών και ακολούθως πραγματοποιείται αξιολόγηση της επίδοσης του δικτύου για κάθε ένα από αυτά.
Συνεχίζοντας την ανάλυση σε κομβικές τεχνολογίες που καθορίζουν τα δίκτυα 6ης γενιάς, το ερευνητικό ενδιαφέρον στρέφεται στην ενσωμάτωση των μη επανδρωμένων εναέριων οχημάτων στα κυψελωτά δίκτυα. Δυστυχώς, τα τρέχοντα κυψελωτά δίκτυα δεν έχουν σχεδιαστεί για να περιλαμβάνουν πρωτίστως εναέριους κόμβους. Κινητοποιημένοι από τα προαναφερόμενα, προτείνεται το

τρισδιάστατο διωνυμικό κυψελωτό δίκτυο ως υποψήφια κυψελωτή αρχιτεκτονική για τα δίκτυα μη επανδρωμένων εναέριων οχημάτων επόμενης γενιάς. Το τρισδιάστατο διωνυμικό κυψελωτό δίκτυο περιλαμβάνει αποκλειστικά εναέριους σταθμούς βάσης και χρήστες και βασίζεται στη κυψελωτή δομή του περικομμένου οκτάεδρου, το οποίο είναι η πιο κοντινή προσέγγιση μίας σφαίρας που μπορεί να πληρώσει τον τρισδιάστατο χώρο χωρίς κενά ή επικαλύψεις. Εξαιτίας της ιδιαίτερης γεωμετρίας του περικομμένου οκτάεδρου, η διεξαγωγή της αξιολόγησης της επίδοσης του δικτύου σε επίπεδο συστήματος είναι ιδιαίτερα απαιτητική. Μία βασική πρόκληση που καλούμαστε να αντιμετωπίσουμε αποτελεί ο υπολογισμός του όγκου των υποπεριοχών της κυψέλης που μπορεί να βρεθεί ένας εναέριος χρήστης. Στη συνέχεια, εκμεταλλευόμενοι την τρισδιάστατη διωνυμική στοχαστική διαδικασία για τη μοντελοποίηση της χωρικής θέσης των εναέριων χρηστών, διεξάγεται αξιολόγηση της επίδοσης ως προς την πιθανότητα κάλυψης για την περίπτωση 1) παρεμβολών εντός της κυψέλης, και 2) για τη περίπτωση παρεμβολών εντός και εκτός της κυψέλης. Για λόγους πληρότητας, η ανάλυση διεξάγεται επίσης και για μία κυψέλη της οποίας το γεωμετρικό σχήμα μοντελοποιείται ως μία σφαίρα. Τονίζεται οτι η σφαίρα μπορεί να αποτυπώσει την επίδραση που έχει ο τρισδιάστατος χώρος στην επίδοση του δικτύου ενώ την ίδια στιγμή η εξαγωγή αναλυτικών εκφράσεων των μετρικών επίδοσης γίνεται απλούστερη. Με βάση αυτή την προσέγγιση, πραγματοποιείται λεπτομερής αξιολόγηση επίδοσης υπό την θεώρηση ενός ισχυρού παρεμβολέα για ένα δίκτυο που μοντελοποιείται ως σφαίρα. Ακολούθως εξάγονται εκφράσεις σε κλειστή μορφή για την πιθανότητα κάλυψης, το ρυθμό σφάλματος bit, το λόγο μέσης ισχύος του λαμβανόμενου σήματος προς την ισχύ της παρεμβολής και την συνολική χωρητικότητα. Τέλος, προσπαθούμε να ρίξουμε περισσότερο φως στη σύγκριση της επίδοσης μεταξύ των κυψελωτών δικτύων που βασίζονται στη σφαίρα και αυτών που βασίζονται στη περικομμένο οκτάεδρο. Για το λόγο αυτό, το ερευνητικό ενδιαφέρον στρέφεται προς τη χωρική τοποθέτηση των εναέριων σταθμών βάσης και επομένως πραγματοποιείται μία σύγκριση της επίδοσης μεταξύ του κυψελωτού δικτύου που βασίζεται στο περικομμένο οκτάεδρο και ενός κυψελωτού δικτύου που βασίζεται σε τρισδιάστατες διωνυμικές κυψέλες Voronoi μέσα σε μία σφαίρα. Καθώς η πραγματική χωρική τοποθέτηση των εναέριων σταθμών βάσης δεν είναι απόλυτα προκαθορισμένη αλλά ούτε και τελείως τυχαία, η τελική σύγκριση της επίδοσης πραγματοποιείται προκειμένου να αναδείξει τα οφέλη κάθε μοντέλου ως υποψήφιο τρισδιάστατο κυψελωτό δίκτυο για μη επανδρωμένα εναέρια οχήματα με εφαρμογή σε ασύρματα δίκτυα επόμενης γενιάς.

Performance Evaluation of Terrestrial and Aerial Communication Networks

Charalampos K. Armeniakos

(ABSTRACT)

Moving with tremendous growth toward the sixth-generation (6G) networks, it becomes more and more clear that a key feature of the new era will be the uninterrupted connectivity to both users and machine-type devices for supporting a huge variety of applications. To this end, the research and industry community turns to key enabling technologies such as the millimeter-wave (mmWave) and the unmanned aerial vehicles (UAVs). However, the introduction of these technologies comes with several challenges. To investigate these challenges and propose solutions for the design of 6G cellular networks, detailed system-level analysis is required, which is the main objective of this dissertation.

First, a comprehensive performance analysis is conducted for terrestrial mmWave networks, where the user equipments (UEs) and the base stations (BSs) are equipped with antenna arrays that are able to form directional beams. Nevertheless, with the introduction of beamforming capabilities and the inevitable misalignment error between the two communications antennas, it becomes clear that both polar coordinates should now be *jointly* considered in the user association policy and the performance evaluation of the network. By jointly considering both polar coordinates, the probability density function (PDF) of the maximum received power and the Laplace transform of the aggregate interference power distributions, are derived in exact form. Subsequently, coverage probability is examined by exploiting fundamental tools of stochastic geometry. Going one step further, the analysis is also conducted for two other association schemes, i.e., an ideal baseline scenario and a purely angular distance-based association scheme. The effect of a single dominant interferer in coverage probability is also investigated for each policy scheme. As a baseline approach, a finite mmWave network under perfect alignment between the serving BS and the receiver is also considered. To elaborate more on system-level insights, three key interference scenarios are presented and the network's coverage performance is subsequently investigated.

Continuing the analysis on 6G key enabling technologies, the research interest now turns on the integration of UAVs in cellular networks. Unfortunately, current cellular architectures have not primarily been designed for integrating aerial nodes. Triggered by the aforementioned, the *binomial 3D cellular network* is proposed as a candidate cellular architecture for beyond fifth-generation (5G) UAV networks. The binomial 3D cellular network integrates merely UAV-BSs and UAV-UEs and it builds on the truncated octahedron cell-shape which is the closest approximation of a sphere which can fully tessellate the three-dimensional (3D) space with no overlaps or gaps. Due to the peculiar geometry of the truncated octahedron, conducting a performance evaluation at system-level is particularly challenging. A key challenge is the evaluation of the volume of the sub-regions of a truncated octahedron cell-shape in which a UAV-UE may fall. Accordingly, by exploiting the 3D binomial point process (BPP) for modeling the spatial locations on the UAV-UEs, performance analysis in terms of coverage probability is conducted under i) intra-cell interference only, and ii)

both intra- and a worst-case inter-cell interference scenario. For the sake of completeness, coverage probability analysis is also conducted for a finite cell modeled as a sphere which can clearly capture the effect of the 3D coverage space while on the same time retains analytical tractability. Accordingly, the analysis focuses to the performance under a dominant interferer approach in a finite cell modeled as a sphere. Closed-form expressions are obtained for the coverage probability, BER, average output SIR, and ergodic capacity. Finally, we bring more light to the debate between cellular networks which are based on the sphere cell-shape and networks which are based on the truncated octahedron cell-shape. Accordingly, the interest turns to the spatial deployment of the UAV-BS and therefore a system-level performance comparison is conducted between the truncated octahedron-based cellular network and a 3D binomial-Voronoi network in a sphere. While the actual UAV-BS 3D deployment is neither absolutely well-defined nor totally random in practice, performance comparison is conducted to highlight the benefits of each model as a candidate 3D cellular UAV network for beyond-5G wireless communication systems.

Dedication

To my parents, Konstantinos and Antigoni, my love, Eva and my supervisor, Prof. Kanatas

Acknowledgments

In the beginning of my Ph.D. journey, the first thing I started thinking about, was the journal papers I had to publish. I was passionate and I started to search for papers relevant to my research area but I got disappointed. The truth was I could not understand the fundamentals of stochastic geometry theory and I didn't know where to start. Fortunately, I got extremely lucky to have two great Professors by my side, Prof. Athanasios G. Kanatas, the supervisor of my thesis and Prof. Petros S. Bithas, who made things much easier for me than what I expected. Apart from providing me with a clear research direction, Prof. Kanatas was always by my side providing me with a methodology to work when I was confused and taught me to be humble. He always used to say "One step at a time". I am also grateful to the millions of technical discussions we had all these years. It is needless to mention that the knowledge I gained from him extends far beyond the scope of my thesis. Prof. Bithas, who is more like a friend to me than a supervisor, taught me the fundamentals of stochastic analysis by starting from zero. I was always surprised by his ability to make me relieve my anxiety, especially during the early stages of my Ph.D. journey. I am also extremely grateful for his endless patience all these years because I was not the easiest person to cooperate with. He means a lot to me. Finally, I would like to thank Prof. Konstantinos Maliatsos for his help in all research projects all these years and the constant efforts to show me the technical aspects and challenges of my research work in practise by using software defined radio!

I would also like to thank all the members of my examination committee for their time to review and handle this Ph.D. dissertation. Particularly, I want to thank Prof. George Karagiannidis from the Aristotle University of Thessaloniki for kindly accepting the invitation to be part of my examination committee.

Most importantly, I would like to deeply thank and devote this thesis to my parents, Konstantinos and Antigoni, for their constant support all these years and my brother, George for motivating me. The completion of this dissertation would not have been possible without their encouragement in this long journey. Finally, I would like to sincerely thank my girlfriend Eva for her endless patience and constant support in many difficult periods during my Ph.D. journey. Without her I would have been distracted from my goal so many times all these years. Thank you Eva!

Contents

List of Figures

List of Common Abbreviations

2D Two-Dimensional

3D Three-Dimensional

3GPP Third Generation Partnership Project

5G Fifth Generation

6G Fifth Generation

AoA Angle-of-Arrival

AoD Angle-of-Departure

AWGN Additive White Gaussian Noise

BER Bit Error Rate

BPP Binomial Point Process

BS Base Station

CCDF complementary Cumulative Distribution Function

CDF Cumulative Distribution Function

CoMP Coordinated MultiPoint

HPPP Homogeneous Poisson Point Process

i.i.d. independent and identically distributed

JCAS Joint Communication and Sensing

LoS Line-of-Sight

MGF Moment Generating Function

MIMO Multiple-input multiple-output

mmWave millimeter Wave

NLoS Non-Line-of-Sight

NOMA Non-orthogonal multiple access

NR	New Radio
PDF	Probability Density Function
pgfl	probability generating functional
PPP	Poisson Point Process
RIS	Reconfigurable Intelligent Surfaces
SINR	Signal-to-Interference-plus-Noise Ratio
SIR	Signal-to-Interference Ratio
SNR	Signal-to-Noise Ratio
THz	Terahertz
UAV	Unmanned Aerial Vehicle
UE	User Equipment

Chapter 1

Introduction

1.1 Background and Motivation

As the standardization of 5G NR technology operating in mmWave bands is over, the focus of the research community is now shifting towards performance analysis and optimization of beyond 5G wireeless communication systems for future cellular deployments. As we rapidly step towards the 6G vision seeking for even more capacity at the air interface, the research community already starts to entertain the challenge of utilizing the mmWave and THz frequency band for cellular communications having tens or even hundreds of GHz of consecutive bandwidth available. Indeed, the utilization of mmWave and THz frequency bands promises to bring the extreme capacity to the air interface enabling novel 6G-based rate-greedy applications such as virtual reality (VR), augmented reality (AR), and holographic telepresence [1]. Compared with conventional microwave communications, mmWave communications have specific peculiarities, making the deployment and operation of next-generation mmWave cellular networks more challenging [2]. Firstly, mmWave signals are more vulnerable to blockage, which directly affects the coverage performance of mmWave cellular networks. To overcome this limitation, mmWave networks are envisioned to be densely deployed to shorten the serving distance to users and, in turn, achieve an acceptable coverage and rate. Unfortunately, increasing the density of BSs leads to severe interference problems and the network tends to be interference-limited. As mmWave signals are susceptible to the surrounding environment which leads to significant path loss and in order to address the severe interference problems, beamforming techniques are adopted to achieve substantial array gains and compensate the high propagation loss. In this case, a peculiar interference scenario which may severely downgrade the performance at a desired receiver may be experienced: An interfering node might now cause fatal interference to the desired receiving node even when the interfering node is located far from the receiving node, if its highly directional antenna gain points to the desired receiving node and the AoA may fall within the 3dB beamwidth of the antenna beam. This unique characteristic of beyond 5G mmWave networks should be considered during the receiver's association policy, interference management schemes and performance optimization of the network. A fundamental objective of this dissertation is to address such challenges and provide key design insights and guidelines for beyond 5G mmWave cellular networks.

On another front, with the increasing maturity of 6G wireless communication systems and in

order to meet all those challenges introduced by the novel 6G-based applications, the UAVs have been introduced as powerful technology enablers and are envisioned to play a key role in the 6G vision. In principle, a UAV can act either as an aerial UE, or a relay to assist serving the ground UEs, or even a BS, also known as a UAV-BS. UAVs possess several advantages over their conventional terrestrial counterparts due to their mobility, ease of deployment, cost-effectiveness, and a high probability of establishing LoS links. UAVs were considered an essential part of the 5G ecosystem as part of the Non-Terrestrial-Network (NTN) domain – mainly as flying base stations, integrated access and backhaul (IAB) enablers, relays, or coverage extenders. In 6G, the role of the UAVs is significantly upgraded – especially under the context of all applications enabled and supported by the new generation of networking. Indeed, the UAVs are expected to contribute towards the "cell-free" 6G paradigm in conjunction with multi-dimensional antennas, reconfigurable intelligent or holographic surfaces, perform energy harvesting and contribute within the JCAS framework. Despite the numerous advantages offered by the UAVs, this new technology comes with its own unprecedented challenges. For instance, for UAV-BSs, some key design problems include 3D deployment and trajectory optimization for maximizing key performance metrics. For UAV-UEs, there is a need for i) reliable and low latency communications for efficient control, and ii) determining the 3D cell association criteria. Unfortunately, existing terrestrial cellular networks have been primarily designed for supporting ground users and are not able to readily serve aerial users. Clearly, to support UAVs in wireless networking applications, there is a need for developing the 3D cellular network that incorporates both UAV-BSs and UAV-UEs. Subsequently, the 3D cell association of the UAV-UEs can be determined. Triggered by the aforementioned, part of this dissertation is dedicated to the design and performance analysis of beyond 5G 3D cellular networks able to support both terrestrial and UAV nodes.

1.2 Selected Prior Works

Terrestrial mmWave/THz Networks. Since highly directional beams are usually employed in mmWave/THz communications, the proper choice of the antenna pattern for the UE or/and the BS is crucial and should be carefully considered in the statistical characterization of interference and hence in the network's performance analysis. One work that clearly established a meaningful yet simple relation between the received power and the role of the antenna pattern is [2]. In particular, by highlighting the interference caused by highly directional beams, the authors proposed two inter-cell interference coordination (ICIC) schemes for mmWave bands: the first one was merely based on the path loss incorporating the blockage effect; the other one considers both path loss and directivity gain. Nevertheless, a comprehensive performance analysis of mmWave networks under LoS/NLoS conditions due to blockages had already been conducted by [3]. Among several insights, the authors were the first that introduced the concept of an equivalent LoS ball for investigating the performance of mmWave networks. Recently, in [4], the authors extend to a non-coherent joint transmission scheme and capture the impact of misalignment errors in the performance of THz networks. The

impact of LoS/NLoS conditions is captured by introducing a LoS equivalent point process for the first time. Nevertheless, it is clearly stated that as a simplifying assumption, the impact of beam alignment errors during the process of user association is not considered.

Beyond 5G Aerial Cellular Networks. Looking closely to the open technical literature, it is easy to observe that the majority of existing works that investigate the performance of UAV networks, assume that the UAVs are spatially distributed in 2D space, e.g, on a disc above the ground. While the aforementioned assumption usually yields mathematical tractability and can even approximate practical deployment scenarios, it clearly cannot capture the architecture of an aerial cellular network, similar to the Voronoi or the hexagonal cells of the current terrestrial cellular networks. Triggered by the aforementioned, in [5], the authors introduce the concept of a beyond 5G 3D cellular network that integrates both UAV-BSs and UAV-UEs in an entirely aerial networking platform. Is it worth mentioning that the proposed architecture served as a candidate 3D cellular network model for beyond 5G cellular UAV networks. While the spatial locations of UAV-BSs were deterministic forming a well-defined 3D lattice of cells, the spatial distribution of the drone-UEs was estimated through an algorithmic approach using a kernel density estimation method. An optimization problem for the 3D cell association was performed by exploiting optimal transport theory and no exact-form expressions were obtained. To overcome the computational complexity issues, the authors in [6] propose an entirely aerial cellular networking platform based on 3D Voronoi cells, which built on the graph tool of binomial-Delaunay tetrahedralization. Other 3D cellular networks that have been proposed build on the sphere [7],[8] which can definitely capture the effect of 3D space in modeling and performance of UAV networks but clearly cannot be considered an aerial cellular network. Up to now, the proposed beyond 5G 3D cellular networks which integrate *merely* aerial nodes are particularly few in the open literature.

1.3 Contributions

The main contributions of this dissertation are summarized as follows along with the related publications. The detailed technical contributions are provided under the "Contributions" section of each chapter.

1.3.1 The Role of Angular Distances in the Maximum Power Association Policy & in the Performance of Terrestrial mmWave Networks

The introduction of the beamforming capabilities as a central feature in 5G NR that leads to higher data rates, causes a series of beam management procedures to arise to ensure efficient handling and network operation. In a network where the UEs and the BSs are equipped with

antenna arrays that are able to form directional beams, one of the most rational criteria is to perform the association of a UE to its serving BS based on the maximum received power. However, another key feature of realistic mmWave networks is that beam misalignment is inevitable, and the direction of the UE's maximum gain may not be necessarily fully aligned with the corresponding one of the serving BS. Therefore, the selection of the serving BS will strongly depend on its location and thus, one should account for both polar coordinates of the candidate serving BSs in the determination of the maximum receiver power. The main part of Chapter 2 is dedicated to the investigation of the performance analysis of terrestrial mmWave networks. To this end, the maximum power association policy is refined to *jointly* account for both polar coordinates in the user association policy and in the calculation of the aggregate interference power.

Subsequently, the role of angular distances in the interference characteristics is highlighted. In particular, in mmWave networks, the interference characteristics are heavily dependent on the directional transceiver beams and the corresponding half power beamwidths. Consequently, the dominant interfering BS may not necessarily be the closest one to the receiver. Instead, a worst-case dominant interference scenario may be experienced by assuming the dominant interferer as the closest BS both in angular distance from the direction of the serving BS and the second nearest in Euclidean distance from the receiver. The angular distances now have a key role in the definition of the interference within the antenna array pattern. Therefore, a far interferer may cause severer interference than a closer one, due to the fact that the AoA at the receiver may fall within the 3dB beamwidth of the antenna beam. In order to merely capture the effect of interference in mmWave networks, subsection 2.6 of Chapter 2 is dedicated to the investigation of the performance of a practical BPP mmWave network under the assumption of perfect alignment between the directions of maximum gain of the serving BS and the receiver. Subsequently, by defining the SINR for the three baseline interference scenarios, the coverage probability is derived in exact form. Numerical results highlight the key role of the azimuthal angles in the definition of dominant interference and consequently in the coverage performance in mmWave cellular networks.

1.3.2 From Ground to Air: The Road towards a beyond-5G 3D Cellular UAV Network

The research work that was conducted in the rest of this dissertation is dedicated to the design and performance of beyond-5G 3D cellular UAV networks. To this end, the design and the statistical characterization of the performance of UAV netoworks is conducted for the conventional case where the maximum power-based association policy for the UAV-UEs is reduced to the widely adopted minimum path loss criterion.

In Chapter 3, the *binomial 3D cellular network*, where the spatial locations of UAV-UEs are modeled as a 3D BPP truncated octahedron cell-shapes is proposed. In particular, the binomial 3D cellular network is defined as a network composed by truncated octahedron cell-

shapes which integrates UAV-UEs, whose spatial locations are modeled as a 3D BPP. The role of the truncated octahedron cell-shape as a candidate 3D cell for beyond 5G UAV networks is highlighted. Subsequently, a comprehensive stochastic geometry-based statistical analysis is conducted and the distance distributions are derived in closed form for both a 3D BPP and a finite HPPP within a truncated octahedron. To this end, a key challenge faced, was the evaluation of the volume of the sub-regions of a truncated octahedron cell-shape in which a UAV-UE may fall. Accordingly, performance analysis in terms of coverage probability is conducted under i) intra-cell interference only, and ii) both intra- and a worst-case inter-cell interference scenario. For the sake of completeness, this analysis is also conducted for a finite cell modeled as a sphere which is a 3D model that retains analytical tractability. Among several intermediate results in the coverage probability analysis, the Laplace transform of the aggregate interference was derived for the binomial 3D cellular network. Among several system-level insights, is was revealed that the conventional spherical model provides a more optimistic performance trend in terms of coverage, as compared to the truncated octahedron cell-shape mode.

To reduce the complexity that the binomial 3D cellular network introduces, Chapter 4 of this dissertation is dedicated to the impact of more tractable 3D models in the performance of beyond 5G UAV networks. In particular, the 3D BPP is exploited to model the spatial locations of a realistic UAV network, where a finite number of UAVs is assumed to be deployed inside a sphere. Notably, a sphere cell-shape can fully capture the effect of 3D coverage space while on the same time yields analytical tractability. Subsequently, by exploiting the dominant interferer approach, a detailed SIR-based performance analysis is conducted in terms of coverage probability, average SIR, BER and ergodic capacity and closed-form expressions for the aforementioned metrics are derived.

Having investigated the performance of both binomial 3D cellular network and a 3D UAV network modeled as a sphere and having demonstrated the trade-offs of each architecture, in Chapter 5 performance comparison of wireless aerial 3D cellular network models is conducted. In particular, by employing the 3D PPP for modeling the spatial locations of UAV-UEs, performance analysis in terms of coverage probability and average rate is conducted in a truncated octahedron-based cellular network. Next, performance analysis is conducted for a finite realistic 3D binomial-Voronoi UAV network. This network model introduces randomness in both the spatial deployment of the UAV-BS and the cell structure, while in the same time allows for a tractable analysis. Also, the performance in a 3D binomial-Voronoi network is compared to the one in a regular network with uniformly random selection policy. While the actual UAV-BS 3D deployment is neither absolutely well-defined nor totally random in practice, performance comparison is used to obtain insights and highlight the benefits of each model as a candidate 3D cellular UAV network for next-generation wireless communication systems.

1.4 Fundamentals of Stochastic Geometry Theory & Mathematical Constructs

In this subsection, we briefly present helpful fundamentals of stochastic geometry theory and preliminary mathematical constructs which are extensively exploited in this dissertation.

1.4.1 Homogeneous Poisson Point Process

The HPPP is considered as the most popular point process due to its tractability and analytical flexibility and thus, it is widely adopted for the performance analysis of wireless networks.

In general, a HPPP Ψ of density λ is a point process in $\mathbb{R}^d$ such that:

- For every compact set $W \subset \mathbb{R}^d$, $N(W)$ has a Poisson distribution with mean $\lambda|W|$ and is characterized by a PMF as

$$\mathbb{P}[N(W) = m] = \frac{(\lambda|W|)^m}{m!} e^{-\lambda|W|}, \tag{1.1}$$

  where $|\cdot|$ denotes the Lebesgue measure or the d-dimensional volume of the subset W and $N(\cdot)$ is the counting measure, i.e., the number of points falling in W.

- If $W_1, ..., W_n$ are disjoint bounded sets, then $N(W_1), ..., N(W_n)$ are independent random variables.

1.4.2 Binomial Point Process

The BPP is a basic process whereby a fixed number of nodes M is identically and independently distributed on a compact set $W \subset \mathbb{R}^d$. For a fixed number M of nodes inside a given network area W, if $k \leq M$ nodes are located in a certain subset $V \subset W$, the remaining area $W \setminus V$ contains necessarily $M - k$ nodes, which introduces dependence between points of W. In this case, the HPPP is clearly not a proper choice. Instead, the BPP can be exploited for the spatial modeling of nodes in finite wireless networks, where the number of nodes which is deployed in the network is predetermined.

The properties of the HPPP and the BPP are particularly useful for simulating point processes. For example, conditioned on a compact set $W \subset \mathbb{R}^d$, the only distinction between a HPPP and a BPP in W is that different realizations of a HPPP consist of a different number of points.

1.4.3 A Fundamental Mathematical Tool for Calculating Interference Power Distribution: Laplace Transform

In stochastic geometry theory, it is often mathematically convenient to statistically characterize the aggregate interference power distribution of the aggregate interference I through the Laplace transform of I to calculate the coverage probability. In the following, we present two baseline tutorials for deriving the Laplace transform of the aggregate interference power distribution under two conventional setups in HPPP and BPP networks which undergo Nakagami-m fading. As it will become clear, there are fundamental conceptual differences in the statistical characterization of I between a HPPP and a BPP network.

Laplace Transform of I in Homogeneous Poisson Networks under Nakagami-m Fading

Let Φ be a homogeneous Point process with density λ denoting the spatial locations of the BSs in a wireless network. Consider an oversimplified scenario where I is given by $I = \sum_{\boldsymbol{x}\in\Phi^!} p h_x \|\boldsymbol{x}\|^{-\alpha}$, where $\Phi^!$ denotes the point process of the interfering BSs which is obtained as the set of all BSs excluding the serving BS for the receiver at the origin $\mathbf{o}$. By adopting the minimum path loss criterion, the serving BS is conventionally the closest BS to the receiver. The channels are assumed to experience Nakagami-m fading and therefore $h_x \sim \Gamma(m, 1/m)$, $\|\cdot\|^{-\alpha}$ denotes the path loss function with path loss exponent α and p is the transmit power of the BSs. Unfortunately, by adopting ordered distances in the receiver's association policy, the distances between the receiver and the interfering BSs are no longer independent random variables. However, conditioned on the serving distance $\|x_0\|$, the distances between the receiver and the interfering BSs are now i.i.d. random variables. The Laplace transform definition conditioned on the serving distance $\|x_0\|$ yields

$$\begin{aligned}
&\mathcal{L}_I(s|\|x_0\|) \triangleq \mathbb{E}_{\Phi^!,h_x}[e^{-sI}|\|x_0\|] = \mathbb{E}_{\Phi^!,h_x}\Big[e^{-s\sum_{\boldsymbol{x}\in\Phi^!} p h_x \|\boldsymbol{x}\|^{-\alpha}}\Big|\|x_0\|\Big] \\
&\overset{(a)}{=} \mathbb{E}_{\Phi^!}\Big[\prod_{\boldsymbol{x}\in\Psi^!_{bs}} \Big(1+\frac{s\,p\|\boldsymbol{x}\|^{-\alpha}}{m}\Big)^{-m}\Big|\|x_0\|\Big] \\
&\overset{(b)}{=} \exp\Bigg(-\lambda\iint_{\boldsymbol{\Omega}}\Big(1-\Big(1+\frac{s\,p\,\|\boldsymbol{x}\|^{-\alpha}}{m}\Big)^{-m}\Big)\mathrm{d}\boldsymbol{x}\Bigg) \\
&\overset{(c)}{=} \exp\Bigg(-\lambda\int_0^{2\pi}\int_{\|x_0\|}^{\infty}\Big(1-\Big(1+\frac{s\,p\,\|x\|^{-\alpha}}{m}\Big)^{-m}\Big)x\mathrm{d}\phi_x\mathrm{d}x\Bigg),
\end{aligned}$$

where (a) follows from the MGF of the gamma random variable h_x, (b) follows from the pgfl of the HPPP with respect to the MGF obtained in step (a). Here, $\boldsymbol{\Omega}$ denotes the set of spatial locations $\boldsymbol{x} \in \Phi^!$ where the interfering BSs can lie and it is mathematically defined as $\boldsymbol{\Omega} = \{(x,y) \in \mathbb{R}^2 \setminus b(\mathbf{o}, \|x_0\|)\}$, where $b(\mathbf{o}, \|x_0\|)$ denotes a ball of radius $\|x_0\|$ centered at

o. Finally, (c) follows from a transformation to polar coordinates $\boldsymbol{x} = (x, \phi_x)$.

Laplace Transform of I in BPP Networks under Nakagami-m Fading

We consider a wireless network of N BSs uniformly distributed in a finite compact set $\mathcal{A}$ forming a BPP Ψ. For simplicity, it is assumed $\mathcal{A} = b(\mathbf{o}, R)$, with R being the maximum deployment distance. While the devices can be strategically placed to optimize the network utility, in the absence of exact traffic patterns, these optimal locations are not known, which justifies the BPP assumption. The receiver located at **o** is assumed to be associated with the closest BS located at distance r. The aggregate interference I is assumed to be given by $I = \sum_{i=1}^{N-1} p h_i {d_i}^{-\alpha}$, where $\{d_i\}_{i=1:N-1}$ denotes the unordered set of distances between the receiver and the $N-1$ interfering BSs. Following similar conceptual lines as in the previous subsection, the Laplace transform definition conditioned on the serving distance r yields

$$\begin{aligned}
\mathcal{L}_I(s|r) &\triangleq \mathbb{E}_I[e^{-sI}|r] = \mathbb{E}_{d_i,h_i}\left[e^{-s\sum_{i=1}^{N-1} p h_i {d_i}^{-\alpha}}\middle| r\right] \\
&\overset{(a)}{=} \mathbb{E}_{d_i}\Big[\prod_{i=1}^{N-1}\Big(1+\frac{s\,p{d_i}^{-\alpha}}{m}\Big)^{-m}\Big| r\Big] \\
&\overset{(b)}{=} \Big[\mathbb{E}_{d_i}\Big[\Big(1+\frac{s\,p{d_i}^{-\alpha}}{m}\Big)^{-m}\Big| r\Big]\Big]^{N-1} \\
&\overset{(c)}{=} \Big[\int_r^R \Big(1+\frac{s\,pd^{-\alpha}}{m}\Big)^{-m} f_{d_i|r}(d)\mathrm{d}d\Big]^{N-1},
\end{aligned}$$

where (a) follows from the MGF of the gamma random variable h_i, (b) follows from conditionally i.i.d. distances of interferers from the receiver, and (c) follows after applying the definition of expectation and using the conditional PDF of d_i.

1.5 List of Publications

This dissertation had led to several *related* journal and conferences as listed below.

Journal Publications

[J1] **H. K. Armeniakos**, A. G. Kanatas and H. S. Dhillon, "Comprehensive Analysis of Maximum Power Association Policy for Cellular Networks Using Distance and Angular Coordinates," *IEEE Trans. Wireless Commun.*, doi: 10.1109/TWC.2024.3388845, 2024.

[J2] **C. K. Armeniakos** and A. G. Kanatas, "Performance Comparison of Wireless Aerial 3D Cellular Network Models," *IEEE Commun. Lett.*, vol. 26, no. 8, pp. 1779-1783, Aug. 2022.

[J3] **C. K. Armeniakos**, P. S. Bithas and A. G. Kanatas, "Finite Point Processes in a Truncated Octahedron-Based 3D UAV Network," *IEEE Trans. Veh. Technol.*, vol. 71, no. 7, pp. 7230-7243, Jul. 2022.

[J4] **C. K. Armeniakos**, P. S. Bithas and A. G. Kanatas, "SIR Analysis in 3D UAV Networks: A Stochastic Geometry Approach," *IEEE Access*, vol. 8, pp. 204963-204973, Nov. 2020.

Conference Proceedings

[C1] **H. K. Armeniakos**, A. G. Kanatas and H. S. Dhillon, "Analysis of Cell Association in mmWave Networks based on Euclidean and Angular Distances," *IEEE Int. Symp. Person Indoor Mobile Radio Commun.*, Sep. 2023,

[C2] **C. K. Armeniakos** and A. G. Kanatas, "Angular Distance-Based Performance Analysis of mmWave Cellular Networks," in *Proc. IEEE Global Commun. Conf.,* Dec. 2022.

1.6 Organization

The rest of this dissertation is organized as follows. By refining the maximum power-based association policy for terrestrial mmWave networks, in Chapter 2, a comprehensive performance analysis in mmWave networks is conducted. Going beyond terrestrial communications, in Chapter 3, by exploiting the 3D BPP for modeling the spatial locations of UAV-UEs in a truncated octahedron-based 3D cellular network, the foundations of the binomial 3D cellular network are presented and coverage probability analysis is conducted. In Chapter 4, the research interest turns to the investigation of tractable 3D models and an SIR-based performance analysis is conducted under a dominant interfering UAV node in a sphere. Having highlighted the trade-offs of each model as candidate cellular structures for beyond 5G 3D cellular network, in Chapter 5, a performance comparison between the truncated octahedron-based cellular network and a 3D binomial-Voronoi network in a sphere is finally conducted to reveal system-level insights. Finally, in Chapter 6, concluding remarks, open challenges and future research directions are presented. The potential of integration of 6G key enabling technologies to the developed frameworks is also discussed.

Chapter 2

Comprehensive Analysis of Maximum Power Association Policy for Cellular Networks Using Distance and Angular Coordinates

2.1 Introduction

Due to the rapid proliferation of the smart devices and novel rate-greedy applications, mobile data traffic has witnessed a tremendous growth. As the 5G cellular networks become more ubiquitous and we start thinking of the 6G, the networks will continue to expand to higher frequency bands to address the need for extreme capacity. Recently, mmWave and sub-THz networks, operating at frequencies between 24 and roughly 330 GHz, have attracted considerable attention from both academia and industry due to the enormous available bandwidth [1], [9]. However, the extremely high data rates achieved in mmWave and sub-THz bands come with challenging propagation characteristics, with the path loss being a key issue. To overcome these limitations, first, mmWave networks are envisioned to be densely deployed to achieve acceptable coverage [2]. However, increasing the density of BSs leads to severe interference problems which in turn may cause a significant number of transmission failures. Next, steerable antenna arrays with highly directional antenna beams are needed to achieve high power gain and improved coverage. In this case, the antennas' 3 dB beamwidth becomes a key design parameter. In addition, mmWave channels are sensitive to the dynamically changing propagation environment (moving pedestrians, passing cars, blockages, etc.). Thus, 5G NR mmWave wireless networks rely on adaptive beamforming and beam selection techniques for optimizing the performance.

In a network where the UEs and the BSs are equipped with antenna arrays that are able to form directional beams, one of the most rational criteria is to perform the association of a UE to its serving BS based on the maximum received power. Therefore, the statistical behaviour of the desired received signal power should be investigated by considering both polar coordinates. As we will discuss shortly, if one ignores practical beam management considerations, cell association decisions can be made purely based on the Euclidean distances. However, in this Chapter, it is rigorously argued that if one accounts for practical issues

such as the limited capability of UEs to perform a perfect beam alignment or an imperfect channel estimation, or a codebook-based beamforming with limited number of beams, then one needs to consider *angular distances*.

2.1.1 Related Works and Motivation

With the rise of 5G and beyond communication systems, the use of multiple antennas at the BSs and the UEs has introduced beamforming capabilities as a central feature in 5G NR that leads to higher data rates. However, a series of beam management procedures are needed to ensure efficient handling and network operation. The selection of the best receiving beam is performed by measuring the average received signal power in each beam through exhaustive scanning in a set of candidate serving BSs. The maximum power-based association policy is governed by the distance dependent path loss and the transmitting and receiving antenna gain patterns. However, either a binary valued antenna pattern, called flat-top pattern [10]−[12], or ideal conditions with realistic patterns, i.e., perfect channel estimation and beam training, that imply full alignment between BS's transmitting and UE's receiving beams has been assumed in most cases. In this *ideal baseline scenario*, the cell association decision is purely based on the Euclidean distance between the two nodes [2], [13]−[18].

Many works in the literature have studied beam management techniques and procedures for 5G NR networks by adopting tools from stochastic geometry, since it captures the spatial randomness of network elements [19]−[22]. Modeling the spatial locations of BSs and/or UEs as point processes allows the use of powerful tools from stochastic geometry to derive tractable analytical results for several key performance metrics. Therefore, in [23], the authors study among others both the initial beam selection during BS handover and beam re-selection technique in a mmWave cell. However, the interference from other BSs is ignored. To address this issue, the authors in [24] develop a stochastic geometry framework and conduct a detailed performance analysis in terms of the average achievable rate and success probability. Going beyond coverage probability and the achievable rate, in [25], the authors studied the average number of beam switching and handover events, in mmWave vehicular networks. Beam management techniques were also considered. In [26], both the impact of beamwidth in the reliability and throughput of a THz network and the impact of the highly directional antennas on the beam management procedures was investigated.

In realistic mmWave networks, *beam misalignment* is inevitable, and the direction of the UE's maximum gain may not be necessarily fully aligned with the corresponding one of the serving BS [27]. More specifically, beam misalignment can occur between the transmitting and receiving beams after channel estimation during the 5G NR beam management-based UE's association policy [28] due to the following reasons: 1) use of codebook-based beamforming at the UEs with limited number of beams, 2) imperfect channel estimation, which results in estimation errors in the angle-of-arrival (AoA) or angle-of-departure (AoD), 3) imperfections

in the antenna arrays, which includes array perturbation and mutual coupling, 4) mobility of the transceivers, and 5) environmental vibrations such as from wind or moving vehicles. Indeed, by considering codebook-based beamforming at the UE, the receiver is agnostic to the conditions that provide maximum power and the UE will perform scanning within a distance-limited finite area to select the serving BS among a set of candidate serving BSs. Therefore, it becomes clear that the selection of the serving BS will strongly depend on its location and thus, one should account for both polar coordinates of the candidate serving BSs in the determination of the maximum receiver power. Considering the aforementioned, misalignment needs to be carefully accounted for in the mathematical analyses if one is to capture realistic 5G NR beam management-based association procedures. Notably, while path-loss is just dependent on the frequency and Euclidean distance, misalignment error, which is now a function of the angular distance between the candidate serving BSs and the UE, should be explicitly considered in the measurement of the received power in the UE's association policy. The authors in [4] and [16] model the misalignment error as a random variable following the truncated Gaussian distribution, whereas the authors in [29], derived an empirical PDF for the misaligned gain based on simulations. However, the consideration of codebook-based beamforming at the UE necessitates a more nuanced analysis. This chapter proposes for the first time a stochastic geometry framework to study the performance in a mmWave cellular network by adopting 5G NR beam management-based procedures and jointly considering the impact of both the Euclidean and angular distances of the BSs in the UE's association policy. The use of the angular distance is critical for the accurate estimation of the receiving antenna gain using 3GPP antenna patterns and allows to depart from the ideal baseline scenario.

Along similar lines, many works have captured the effect of the angular coordinate in the calculation of interference power and correspondingly in performance analysis of cellular networks by adopting realistic antenna patterns. In [30], the authors considered the effect of beam misalignment utilizing a 3GPP-based antenna pattern in a stochastic geometry framework. In [31], the authors investigated the impact of directional antenna arrays on mmWave networks. Among other insights, the role of realistic antenna patterns in the interference power is demonstrated. In [32], a multi-cosine antenna pattern is proposed to approximate the actual antenna pattern of a uniform linear array (ULA) and the impact in the interference power is highlighted. In [33], the authors adopt an actual three dimensional antenna model and a uniform planar array, which is mounted on UAVs, to examine the impact of both azimuth and elevation angles on the interference power.

On another front, the idea of the dominant interferer has been introduced in the literature to facilitate the calculation of the SINR and provide a realistic and mathematically tractable approximation of the accurate aggregate interference [34]–[37]. The notion of angular distances and their implication on the identification of the dominant interferer has recently been highlighted in [38] and [39]. Triggered by the previous discussions, a dominant interfering BS may not necessarily be the closest one to the receiver. Indeed, a far interferer may cause severer interference than a closer one, due to the fact that the AoA at the receiver may fall

within the 3dB beamwidth of the antenna beam. Towards this direction, a worst-case dominant interference scenario may now be experienced by assuming the dominant interferer as the closest BS both in angular distance from the direction of the serving BS and the second nearest in Euclidean distance from the receiver. The distribution of the angular coordinates now play a key role in the interference within the mainlobe or the sidelobe of the antenna array pattern.

In summary, even though angular coordinates have appeared in the stochastic geometry-based analysis, their manifestation in the received power as a consequence of realistic beam management procedure and the overall effect on the system performance has not been studied, which is the primary objective of this chapter. Accordingly, this chapter proposes a stochastic geometry framework to study the implications of beam misalignment error in the association policy and the corresponding performance of a mmWave cellular network by adopting realistic 5G NR beam management-based procedures and practical equipment limitations. Extensive comparisons of the ideal baseline scenario with several association policies are provided, and evaluation of diverse dominant interferer-based scenarios is conducted.

2.1.2 Contributions

The key aspects that this chapter addresses are highlighted next.

Angular distance distributions

By exploiting fundamental concepts of stochastic geometry theory, both the nth nearest node and joint angular distance distributions within a finite ball are derived in closed form for a 2D finite HPPP. As it will be shown, these distances play a key role in the definition of dominant interferer in mmWave networks.

Refining the maximum power association policy in a mmWave stochastic geometry framework

By employing the HPPP for modeling the spatial locations of the BSs, a number of BSs with known density are deployed in a mmWave cellular network. The typical UE, which is equipped with a realistic 3GPP-based antenna pattern, exploits directional beamforming capabilities under imperfect alignment to communicate with the serving BS. In this chapter, beam misalignment at the UE may occur due to limited codebook-based beamforming at the UE and/or from imperfect channel estimation and/or potentially antenna arrays imperfections [1], and clearly depends on the random spatial location of the serving BS. Accordingly,

[1] According to the beam management procedure of the 3GPP NR for mmWave frequencies [27], our framework is fully consistent with the Non- Standalone-Uplink (NSA-UL) scheme and beam misalignment

as a key contribution, a realistic beam management-based association policy that jointly considers both the Euclidean and angular distances of the BSs, is proposed for the UE. The proposed policy takes into account both the directional beamforming and the beam misalignment error at the UE through the adoption of a 3GPP-based antenna pattern. Two other association schemes, i.e., an ideal baseline scenario and a purely angular distance-based association scheme, are also proposed as special cases for completeness.

Coverage probability analysis

Performance analysis in terms of coverage probability is conducted under the three association schemes and analytical expressions are obtained. As key intermediate results, the PDF of the maximum received power and the Laplace transform (LT) of the aggregate interference power distributions, are derived in exact form. It is worth mentioning that the computation of the LT of the aggregate interference power distribution presented in this chapter considers the regions of the network on which the interfering BSs may lie and it is based on both distance and angular coordinates.

Special case: Dominant interferer approach

A coverage probability analysis is conducted under the assumption of a single dominant interferer for the maximum received power association policy. As a key result, the joint PDF of the maximum received power from the serving BS and the received power from the dominant interferer is derived. Conventionally, the dominant interferer is considered as the nearest BS based on the Euclidean distance. By extending the definition of the dominant interferer as the nearest BS in angular distance w.r.t. a reference line in mmWave networks, coverage probability analysis is conducted for the two special cases under the assumption of a dominant interferer for which exact-form expressions are derived. To this end, the PDF of the ratio of the nearest BS, in angular distance, antenna gain to that of the second nearest BS, as well as the PDF of the ratio of the corresponding path-losses are derived as insightful intermediate results. Subsequently, the corresponding analytical expressions for the CDF of the achieved SIR are obtained in exact form.

Special case: BPP 5G mmWave networks & a dominant interferer approach

A BPP-based stochastic geometry framework is proposed to capture the effect of dominant interference scenarios in the performance of mmWave networks. To this end, performance analysis in terms of coverage probability is conducted under three interference scenarios: i) a worst-case dominant interference scenario, where the dominant interferer is the BS

can occur during the beam measurement phase as a result of possible array imperfections at the UE and/or imperfect channel estimation.

that is both the nearest in azimuthal angle from the direction of the serving BS, and the second nearest in Euclidean distance from the receiver; ii) a dominant interferer, as the BS that is the closest in azimuthal angle from the direction of the serving BS and uniformly distributed in an annulus formed by the the serving distance and a ball radius R, and iii) the aggregate interference in the network. The PDF of the receiver's gain at the closest interfering BS in angular coordinates and the Laplace transform of the aggregate interference power distribution , are derived as intermediate results in the performance analysis.

2.2 Mathematical Preliminary & Constructs: Angular Distances

In this section, the mathematical constructs of angular distances in 2D HPPP wireless networks defined over a finite region, are presented. These will provide a firm foundation for the understanding and analysis of the coverage probability in mmWave cellular networks.

2.2.1 Angular Distance Distributions

As stated in [38], the investigation of the distributions of the angular distances is based on defining the nth nearest point in angle ϕ from a reference line. Consider an HPPP Φ with intensity λ over $b(\mathbf{o}, r)$, where $b(\mathbf{o}, r)$ denotes a ball of a finite radius r centered at the origin o. Let ϕ_n denote the random variable representing the angular distance from an arbitrary reference line to the nth nearest point of Φ in the coordinate ϕ, as shown in Fig. 2.1a. Without loss of generality, the reference line is assumed to be the x-axis. Let $\mathcal{A}_{r,n}$ denote the event that $b(\mathbf{o}, r)$ contains at least n points of Φ.

Lemma 2.1. *Conditioned on $\mathcal{A}_{r,n}$, the PDF of the nth nearest point in angular distance in $b(\mathbf{o}, r)$ is given by*

$$f_{\phi_n|\mathcal{A}_{r,n}}(\phi) = \frac{(\lambda r^2)^n \phi^{n-1}}{2^n(\Gamma(n) - \Gamma(n, \lambda\pi r^2))} e^{-\frac{\lambda\phi r^2}{2}}, \quad \phi \in [0, 2\pi], \tag{2.1}$$

where $\Gamma(\cdot)$ is the Gamma function defined as in [40, eq. (8.310.1)] and $\Gamma(\cdot,\cdot)$ denotes the incomplete gamma function defined as in [40, eq. (8.350.2)].

Proof. See Appendix A.1 □

In mmWave cellular networks, it is often of interest the absolute angular distance, $|\phi|$, for the coordinate ϕ. This definition is particularly useful when dealing with angular distances from the direction of the maximum directivity in an antenna beampattern [38]. Let $|\phi| \in [0, \pi]$, as shown in Fig. 2.1b.

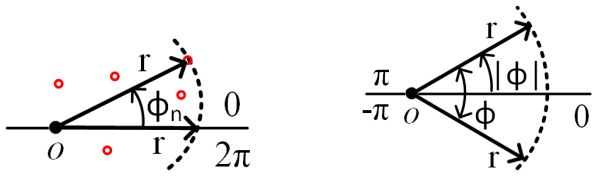

(a) $\phi_n \in (0, 2\pi)$ (b) $|\phi| \in (0, \pi)$

Figure 2.1: The nth nearest point in angular distance in a disk sector.

Corollary 2.2. *Conditioned on $\mathcal{A}_{r,n}$, the PDF $f_{|\phi_n|||\mathcal{A}_{r,n}}(|\phi|)$ is given by*

$$f_{|\phi_n||\mathcal{A}_{r,n}}(\phi) = \frac{(\lambda r^2)^n |\phi|^{n-1}}{\Gamma(n) - \Gamma(n, \lambda\pi r^2)} e^{-\lambda|\phi| r^2}, \quad |\phi| \in [0, \pi]. \tag{2.2}$$

Proof. Letting $\phi = 2|\phi| \in [0, 2\pi]$, then $W(|\phi|, r) = |\phi| r^2$. Then, the proof follows the same steps as the proof for obtaining (2.1). □

2.2.2 Joint Distributions

As mentioned in subsection 2.1.1 of this chapter, a UE may now be connected to the closest BS in angular distance. In this case, the dominant interfering BS may not necessarily be the closest one to the UE, but the closest BS in angular distance w.r.t the line of communication link. This inspires the investigation of joint distributions of angular distances.

Let $|\varphi_n|$ denote the absolute angular distance from o to the nth nearest point in absolute angular distance.

Lemma 2.3. *Conditioned on $\mathcal{A}_{r,2}$, the joint PDF of $|\varphi_1|, |\varphi_2|$ is given by*

$$f_{|\varphi_1|,|\varphi_2|\big|\mathcal{A}_{r,2}}(|\varphi_1|, |\varphi_2|) = \frac{(\lambda r^2)^2 \, e^{-\lambda r^2 (|\varphi_2| - \pi)}}{e^{-\lambda\pi r^2} - \lambda\pi r^2 - 1}, \tag{2.3}$$

where $|\varphi_1| \in [0, \pi]$ and $|\varphi_2| \in [|\varphi_1|, \pi]$.

Proof. See Appendix A.2. □

2.3 System Model

This subsection presents the considered mmWave cellular network and the key modeling assumptions made in this chapter.

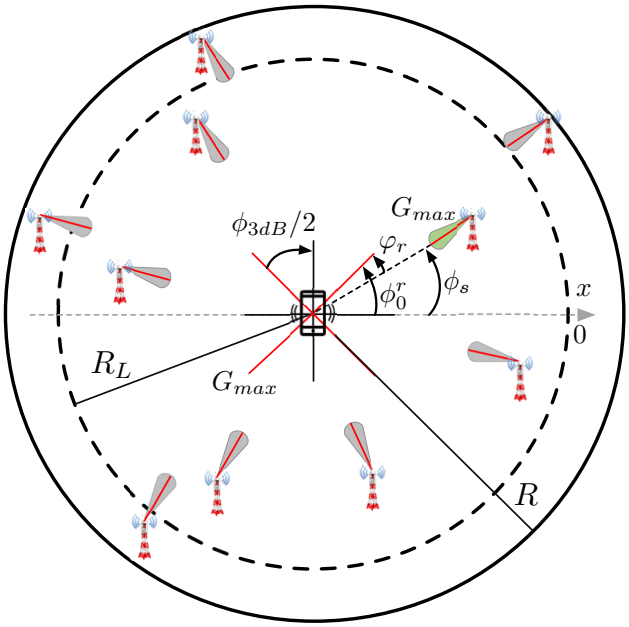

Figure 2.2: Illustration of the system model.

2.3.1 Network Model

Consider a mmWave downlink cellular network, where the locations of the BSs is modeled as a HPPP $\Phi_{bs} \subset \mathbb{R}^2$ with intensity λ_{bs}. Let (r_x, ϕ_x) denote the location of a BS located at $x \in \Phi_{bs}$, in terms of polar coordinates. The locations of UEs are independently distributed according to some stationary point process Φ_{ue}. Also, a BS serves one UE at a time per resource block and all BSs are assumed to transmit at the same power p. Let (r_s, ϕ_s) denote the location of the serving BS $x_0 \in \Phi_{bs}$ at a given time. Without loss of generality, the receiving UE is assumed to be located at the origin $\mathbf{o} = (0, 0)$ at that time. After averaging the performance of this UE over Φ_{bs}, the receiving UE becomes the typical receiver, which will be interchangeably referred to as just the *receiver* in this chapter.

2.3.2 Beamforming and Antenna Modeling

A BS located at $x \in \Phi_{bs}$ is assumed to exploit beamforming techniques to communicate with the receiver. In this work, a worst-case interference scenario is considered in the mmWave network as the maximum gain of all BSs' antennas is assumed to be always directed towards the receiver. Please note that similar scenarios have already been employed in the literature [41]. The receiver is assumed to be equipped with an antenna array able to produce 2^m receiving beams. The maximum gain directions of these beams, i.e., the centers of the corresponding 3 dB beamwidths, are given by $\phi_m = \frac{2\pi}{2^m}$ with $m \in \mathbb{N}$. Then, the maximums of the BS and UE beams will not necessarily be aligned because of the discretization on

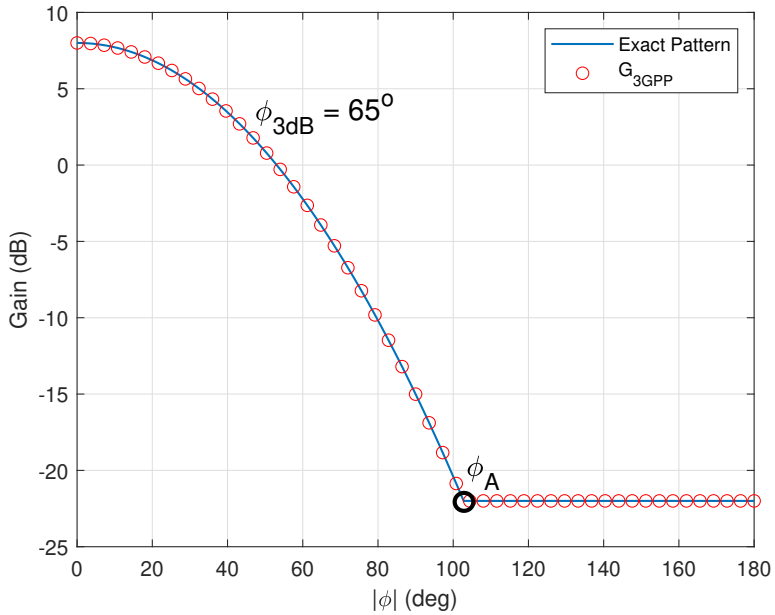

Figure 2.3: Illustration of the gain of the 3GPP-based antenna pattern given by (2.4) vs the approximation of the 3GPP array pattern given by (2.6) for $\phi_{3dB} = 65^o$ and $\phi_0^r = 0$.

the UE side, which is the reason angular distances appear in the analysis. In this work, a realistic 3GPP-based antenna pattern recommended for 5G mmWave communications [42] is adopted for the receiver and therefore, the actual antenna gain within the 3dB beamwidth range is not constant. When directed towards ϕ_0^r, this antenna has a radiation power pattern (in dB) given by

$$G_{3gpp}(\phi - \phi_0^r) = G_{max} - \min\left\{12\left(\frac{\phi - \phi_0^r}{\phi_{3dB}}\right)^2, SLA\right\}, \tag{2.4}$$

where ϕ_{3dB} is the 3dB beamwidth of the receiver's antenna and $SLA = 30$dB is the front-to-back ratio. The multiplicative antenna gain factor is denoted by $g_{3gpp}(\phi - \phi_0^r)$. In this work, the direction of maximum gain ϕ_0^r is modeled as a discrete random variable with probability mass function (pmf) given by

$$\phi_0^r = \begin{cases} \phi_0^1 = \frac{\pi}{2^m}, & \text{w.p. } p_\phi = \frac{1}{2^m} \\ \phi_0^2 = \frac{\pi}{2^m} + \frac{\pi}{2^{m-1}}, & \text{w.p. } p_\phi = \frac{1}{2^m} \\ \vdots & \\ \phi_0^{2^m} = \frac{\pi}{2^m} + \underbrace{\frac{\pi}{2^{m-1}} + \ldots + \frac{\pi}{2^{m-1}}}_{(2^m-1) \text{ terms}}, & \text{w.p. } p_\phi = \frac{1}{2^m} \end{cases}, \tag{2.5}$$

A representative example of ϕ_0^r is shown in Fig. 2.2, with $2^m = 4$ beams enabled at the UE. Unfortunately, the use of the array pattern of (2.4) may lead to extremely intractable analysis [31]. For this reason, the array pattern is approximated by the two-branch expression given by [43],

$$g(\phi - \phi_0^r) = \begin{cases} g_{max} 10^{-\frac{3}{10}\left(\frac{2(\phi-\phi_0^r)}{\phi_{3dB}}\right)^2}, & |\phi - \phi_0^r| \leq \phi_A \\ g_s, & \phi_A \leq |\phi - \phi_0^r| \leq \pi \end{cases} \tag{2.6}$$

where g_{max} and g_s are the multiplicative gain factors of G_{max}, and $G_s = G_{max} - SLA$, correspondingly, whereas $\phi_A = (\phi_{3dB}/2)\sqrt{(10/3)\log_{10}(g_{max}/g_s)}$. It is worth mentioning that the expression for the array pattern given by (2.6) is actually a two-branch expression of the exact 3GPP-based antenna pattern given by (2.4). Indeed, in Fig. 2.3, the gain (in dB) of the 3GPP-based antenna pattern given by (2.4) is compared to a corresponding one under the approximate expression for the gain of the 3GPP array pattern given by (2.6) for $\phi_{3dB} = 65^o$. It can easily be observed that the two expressions for the gains of the array patterns match perfectly, which verifies the fact that the expressions (2.4) and (2.6) are actually equivalent.

2.3.3 Blockage Model

As seen from the receiver location, a BS can be either LOS or non-LOS (NLOS). While mmWave signals are significantly affected by blockages [44], proper modeling is essential to capture the effect of blockages on network performance. In this work, an LOS ball model is adopted since it provides a better fit with real-world blockage scenarios [45], which considers NLOS interfering links. Hence, the performance analysis for the receiver is restricted to $b(\mathbf{o}, R)$, where $b(\mathbf{o}, R)$ denotes a ball of radius R centered at the origin $\mathbf{o}$ and thus, to an almost surely (a. s.) finite HPPP $\Psi_{bs} = \Phi_{bs} \cap b(\mathbf{o}, R)$. Given a BS located at $x \in \Psi_{bs}$, the propagation between the BS and the receiver is LOS if $\|x\| < R_L$, where R_L is the maximum distance for LOS propagation and $\|\cdot\|$ denotes the Euclidean norm.

2.3.4 Path Loss and Channel Models

The LOS and NLOS channel conditions induced by the blockage effect are characterized by different path-loss exponents, denoted by α_L and α_N, respectively. Similar to [24], typical values of these path-loss exponents are $\alpha_L \in [1.8, 2.5]$ and $\alpha_N \in [2.5, 4.7]$. Then, following the standard power-law path-loss model for the path between the receiver and a BS located at $x \in \Psi_{bs}$, the random path loss function is given by

$$l(\|x\|) = \begin{cases} K\|x\|^{-\alpha_L}, & \|x\| < R_L \\ K\|x\|^{-\alpha_N}, & R_L \leq \|x\| \leq R, \end{cases} \tag{2.7}$$

where $K = \left(\frac{c}{4\pi f_c}\right)^2$ with c being the speed of light and f_c the carrier frequency.

The channels between a BS located at $x \in \Psi_{bs}$ and the receiver undergo Nakagami-m_u fading, which is a generalized model for representing a wide range of fading states. The parameter m_u is restricted to integer values for analytical tractability. The channel fading gain h_u is the fading power for the channel in LOS condition. The shape and scale parameters of h_u are m_u and $1/m_u$, respectively, i.e., $h_u \sim$ Gamma $\left(m_u, \frac{1}{m_u}\right)$. Here, $u \in \{s, x\}$, where s denotes the link between the receiver and the serving BS, and x stands for the link between the receiver and the interfering BSs at $x \in \Psi_{bs} \setminus \{x_0\}$. The PDF of h_u is given by

$$f_{h_u}(w) = \frac{m_u^{m_u} w^{m_u - 1}}{\Gamma(m_u)} \exp\left(-m_u w\right). \tag{2.8}$$

2.3.5 User Association and Beam Selection Policy

The association policy used in real networks is often based on the maximum received power. The UE is agnostic to the conditions that provide the maximum power to the receiver. One of the main contributions of this chapter is the adoption of an association policy, namely *Policy 1*, that accurately captures the real conditions. This is achieved by jointly considering both polar coordinates in the calculation of received power. With the introduction of the angular coordinate, this work investigates the use of a similar to the minimum Euclidean distance-based criterion, namely, the minimum angular distance-based one. This is henceforth termed as *Policy 2*. Nevertheless, for system performance analysis purposes it is highly desirable and widely accepted to consider simplified policies. Therefore, a commonly utilized policy, namely *Policy 3*, is the one that assumes only the Euclidean distance criterion. However, this policy ignores the effect of angle-dependent antenna gains and inherently imposes a discrepancy from real received power in the calculations. Consequently, Policies 2 and 3 serve as baseline schemes for comparison to Policy 1 which corresponds to the realistic maximum power association scheme. We are particularly interested in understanding in which regimes can Policy 2 or 3 closely describe the performance of Policy 1, which is clearly more realistic but analytically more complicated compared to the other two. Moreover, because of distance-based path-loss, the candidate serving BSs of the receiver are assumed to lie within $b(\mathbf{o}, R_L)$. From amongst these BSs, the serving BS is determined using the beam management procedure of 5G NR as discussed above. Therefore, the serving BS can lie anywhere within $b(\mathbf{o}, R_L)$. Finally, all the association decisions are assumed to take place within the coherence time of the channel.

Policy 1: Maximum Power-based Association Scheme

In this scheme, the receiver is associated with the BS providing the largest average received power by jointly considering both the Euclidean and the angular distance of the BSs. Specif-

ically, during this association procedure, the best receiving beam is selected by the receiver for reception. According to the beam management procedure in 5G NR, this task is the so-called beam selection procedure. In particular, all BSs periodically transmit the beamformed reference signals, either channel state information reference signals (CSI-RS) or synchronization signal blocks (SSBs), that may cover the entire set of available directions according to the receivers' needs. The measurements in mmWave networks related to the initial access are based on the SSBs. The receiver in the proposed framework monitors the reference signals and forms a list of *candidate serving BSs*, being those BSs with the largest SNR and exceed a predefined threshold, for each beam. Subsequently, the *serving BS*, defined as the BS providing the largest SNR among *all* candidate serving BSs, is chosen for transmission. The corresponding receiver's beam in which the serving BS was identified, is selected as the *receiving beam*.

A key assumption in this policy is that the BS has perfect CSI knowledge of the uplink and thus, a perfect alignment of the BS beam maximum gain direction with the line toward the receiver is achievable. However, the direction of the maximum gain of the receiver's antenna is not fully aligned with the direction of maximum gain of each BS transmitting beam. Let φ_i^x denote the angular distance between the direction of the line connecting the receiver and a BS $x \in \Psi_{bs}$ and the direction, ϕ_0^i, of maximum directivity of a receiver's beam i. Therefore, for a BS $x \in \Psi_{bs}$, ϕ_x denotes its polar coordinate, and φ_i^x is given by $\varphi_i^x = |\phi_0^i - \phi_x|$. By further considering the Euclidean distances of the BSs from the origin, r_x, the location of the serving BS and the receiving beam are chosen by the receiver as

$$(x_0, i) = \underset{\substack{x \in (\Psi_{bs} \cap b(\mathbf{o}, R_L)) \\ i = 1:2^m}}{\text{argmax}} \left\{ g(\varphi_i^x) r_x^{-\alpha_L} \right\}. \tag{2.9}$$

Having selected x_0 and i, the angle φ_i^x is denoted as φ_r in Fig. 2. In this case, φ_r can be modeled as a uniform random variable, i.e., $\varphi_r \sim U[0, \frac{\phi_{3dB}}{2}]$, where ϕ_{3dB} denotes the half-power beamwidth of the user receiving beam. Clearly, the serving BS may not necessarily be the nearest one to the receiver. Instead, it may lie close to the direction of the maximum directivity gain of a receiver's beam and thus providing maximum received power. The equation (2.9) indicates that the receiver performs scanning for each beam to identify the serving BS by jointly considering both the angular distance of the BSs, from the direction of each beam's maxima, and the Euclidean distance of the BSs, respectively to maximize the received power.

Policy 2: Minimum Angular Distance Association Scheme

In this scheme, the receiver is attached to the closest BS in angular distance within $b(\mathbf{o}, R_L)$. Specifically, for each beam, the receiver performs exhaustive scanning and calculates the minimum angle between the direction of the beam's maxima and the direction of the line connecting the receiver and each BS. Then, from a list of 2^m angles, the receiver attaches

to the BS with the minimum angular distance φ_c and the corresponding beam is selected as the receiving beam. Mathematically, the location x_0 of the serving BS and the beam i are selected by the receiver as

$$(x_0, i) = \underset{\substack{x\in(\Psi_{bs}\cap b(\mathbf{o},R_L))\\ i=1:2^m}}{\operatorname{argmin}} \Big\{\{|\phi_0^i - \phi_x|\}\Big\}, \tag{2.10}$$

and φ_c is given by

$$\varphi_c = \min_{i=1:2^m}\Big\{\min_{x\in(\Psi_{bs}\cap b(\mathbf{o},R_L))}\{|\phi_0^i - \phi_x|\}\Big\}. \tag{2.11}$$

Policy 3: Minimum Euclidean Distance Association Scheme

In this scheme, the receiver is associated with the nearest BS in Euclidean distance within $b(\mathbf{o}, R_L)$. In this case, by adopting conventional beam management-based beam steering techniques, the maximum gain of the receiver's antenna is assumed to be directed towards the serving BS and therefore perfect beam alignment is assumed. Without loss of generality, due to the isotropy and the stationarity of the Ψ_{bs}, the reference line can be considered to be along the x-axis and passing through the origin. In this case, the location x_0 of the serving BS is chosen by the receiver as $x_0 = \underset{x\in(\Psi_{bs}\cap b(\mathbf{o},R_L))}{\operatorname{argmin}} \{r_x\}$.

2.3.6 Signal-to-interference-plus-noise Ratio

The SINR under the three association schemes is now defined. Under Policy 1, the received SINR is given by

$$\text{SINR} = \frac{p\, h_s\, g_{max}\, g(\varphi_r)\, l(\|x_0\|)}{I + \sigma^2}, \tag{2.12}$$

where p is the transmitted power and I refers to the aggregate interference power and is given by $I = \sum_{x\in\Psi_{bs}^!} p\, h_x\, g_{max}\, g_{3gpp}(\varphi_I)\, l(\|x\|)$, $\Psi_{bs}^! = \big\{\Psi_{bs}\setminus\{x_0\}\big\}$, φ_I is defined as $\varphi_I = |\phi_0^r - \phi_x|$ and σ^2 is the additive white Gaussian noise power. Please note that, ϕ_0^r also determines the direction of the reference line in this policy.

Under Policy 2, the received SINR is given by

$$\text{SINR} = \frac{p\, h_s\, g_{max}\, g(\varphi_c)\, l(\|x_0\|)}{I + \sigma^2}, \tag{2.13}$$

where I is given by $I = \sum_{x\in\Psi_{bs}^!} p\, h_x\, g_{max}\, g_{3gpp}(\varphi_I)\, l(\|x\|)$ and φ_I is defined as $\varphi_I = |\varphi_c - \phi_x|$. Please note that, φ_c also determines the direction of the communication link in this policy.

Under Policy 3, the received SINR is given by

$$\text{SINR} = \frac{p\, h_s\, g_{max}\, g_{max}\, l(\|x_0\|)}{I + \sigma^2}, \tag{2.14}$$

where I is given by $I = \sum_{x \in \Psi_{bs}^{!}} p\, h_x\, g_{max}\, g_{3gpp}(\phi_x)\, l(\|x\|)$.

2.4 Coverage Probability Analysis

In this section, performance analysis in terms of coverage probability is conducted under the three association schemes. Formally, the coverage probability $\mathcal{P}_c(\gamma)$, is defined as the probability that the SINR at the receiver exceeds a predefined threshold γ, i.e.,$\mathcal{P}_c(\gamma) \triangleq \mathbb{P}(\text{SINR} > \gamma)$.

2.4.1 Coverage Probability Under Maximum Power Association Scheme

To obtain $\mathcal{P}_c(\gamma)$ in this scheme, the PDF of the maximum received power must first be derived. Let S_x^i denote the received power from a BS located at $x \in (\Psi_{bs} \cap b(\mathbf{o}, R_L))$ measured w.r.t to the i-th beam. Then, S_x^i is given by

$$S_x^i = g(|\phi_0^i - \phi_x|)\|x\|^{-\alpha_L} = g(\underbrace{|\phi_0^i - \phi_x|}_{\varphi_i^x}) r_x^{-\alpha_L} \tag{2.15}$$

and the maximum received power S is obtained as

$$\begin{aligned} S &= \max_{\substack{x \in (\Psi_{bs} \cap b(\mathbf{o}, R_L)) \\ i = 1:2^m}} \{S_x^i\} \\ &\overset{(a)}{=} \max_{x \in (\Psi_{bs} \cap b(\mathbf{o}, R_L))} \{\underbrace{g(\varphi^x) r_x^{-\alpha_L}}_{S_x}\} \overset{(b)}{=} g(\varphi_r) r_s^{-\alpha_L}, \end{aligned} \tag{2.16}$$

where (a) follows after maximization of $\{g(\varphi_i^x)\}_{x \in (\Psi_{bs} \cap b(\mathbf{o}, R_L))}^{i=1:2^m}$ over i, i.e., for each x, the best beam is determined and (b) follows from maximization over x with $r_s = \|x_0\|$. Due to exhaustive scanning of the receiver in the whole $b(\mathbf{o}, R_L)$ and conditioned on $\mathcal{A}_{R_L,1}$ in order for S to be meaningfully defined, the serving BS may lie anywhere in $b(\mathbf{o}, R_L)$[2] Therefore, r_x are independent and identically distributed (i.i.d.) in $b(\mathbf{o}, R_L)$ with PDF $f_{r_x}(r)$ of each element given by $f_{r_x}(r) = \frac{2r}{R_L^2}$, $r \in [0, R_L]$.

[2]Conditioned on $\mathcal{A}_{R_L,1}$, it is ensured that at least one LOS BS will always exist. Otherwise, the receiver would try to connect to the strongest NLOS BS, which is not of much practical interest because of significantly weaker NLOS links and is hence beyond the scope of the chapter.

Lemma 2.4. *Conditioned on $\mathcal{A}_{R_L,1}$, the PDF of the maximum received power S is given by*

$$f_{S|\mathcal{A}_{R_L,1}}(s_0) = \frac{\lambda_{bs}\pi R_L^2 f_{S_x}(s_0)\, e^{\lambda_{bs}\pi R_L^2\left(F_{S_x}(s_0)-1\right)}}{1-e^{-\lambda\pi R_L^2}}, \tag{2.17}$$

with $s_0 \in [w_{min}, \infty)$, and $f_{S_x}(w)$ is given by

$$f_{S_x}(w) = \int_{g_{3dB}}^{\psi(w)} \frac{1}{x} f_{g(\varphi^x)}(x) f_{r_x^{-\alpha_L}}\left(\frac{w}{x}\right)\mathrm{d}x, \tag{2.18}$$

with $w \in [w_{min}, \infty)$, and $f_{r_x^{-\alpha_L}}(x) = \frac{2(\frac{1}{x})^{\frac{\alpha_L+2}{\alpha_L}}}{\alpha_L R_L^2}$, $f_{g(\varphi^x)}(g) = \frac{1}{ln(10)x}\frac{10}{12\sqrt{\frac{G_{max}-10log(x)}{12}}}$, $g_{3dB} = 10^{\frac{G_{max}-3}{10}}$, $w_{min} = g_{3dB}R_L^{-\alpha_L}$ and $\psi(w) = \min\left\{\frac{w}{R_L^{-\alpha_L}}, g_{max}\right\}$.

Proof. See Appendix A.3. □

Remark 2.5. Lemma 2.4 captures the misalignment error as a random variable within $g(\varphi_r)$ and thus, it is clearly different from deriving the conventional PDF of the minimum distance-based path-loss.

Lemma 2.6. *Conditioned on the maximum received power $S = S_{th}$ from the serving BS w.r.t. a given receiving beam, the conditional Laplace transform $\mathcal{L}_I(s|S_{th}, \phi_0^r)$ of the aggregate interference power distribution is given by*

$$\begin{aligned}\mathcal{L}_I(s|S_{th},\phi_0^r) = \exp\Big(-\lambda_{bs}\iint_{\mathbf{\Omega}}\Big(1-\Big(1+\frac{s\,p\,K\,g_{max}\,g_{3gpp}(|\phi_0^r-\phi_x|)\,r_x^{-\alpha_L}}{m_x}\Big)^{-m_x}\Big)r_x\mathrm{d}\phi_x\mathrm{d}r_x\Big)\\ \times\exp\Big(-\lambda_{bs}\iint_{\mathbf{\Omega}'}\Big(1-\Big(1+\frac{s\,p\,K\,g_{max}\,g_{3gpp}(|\phi_0^r-\phi_x|)\,r_x^{-\alpha_N}}{m_x}\Big)^{-m_x}\Big)r_x\mathrm{d}\phi_x\mathrm{d}r_x\Big),\end{aligned} \tag{2.19}$$

where

$$\begin{aligned}\mathbf{\Omega} &= \{(r_x,\phi_x)\in\mathbb{R}^2 | r_x^{min}\le r_x\le R_L,\ 0\le\phi_x\le 2\pi\},\\ \mathbf{\Omega}' &= \{(r_x,\phi_x)\in\mathbb{R}^2 | r_x^{max}\le r_x\le R,\ 0\le\phi_x\le 2\pi\},\end{aligned} \tag{2.20}$$

and $r_x^{min} = \min\left\{\left(\frac{g_{3gpp}(|\phi_0^r-\phi_x|)}{S_{th}}\right)^{\frac{1}{\alpha_L}}, R_L\right\}$, $r_x^{max} = \max\left\{\left(\frac{g_{3gpp}(|\phi_0^r-\phi_x|)}{S_{th}}\right)^{\frac{1}{\alpha_N}}, R_L\right\}$.

Proof. See Appendix A.4. □

Theorem 2.7. *Conditioned on $\mathcal{A}_{R_L,1}$, the coverage probability of a receiver in a mmWave*

network inside $b(\mathbf{o}, R_L)$ *under the maximum power-based association policy is given by*

$$\mathcal{P}_c(\gamma) = \sum_{i=1}^{2^m} \sum_{k=0}^{m_s-1} \int_{w_{min}}^{\infty} \frac{(-s)^k}{k!} \left[\frac{\partial^k \mathcal{L}_{I_{tot}}(s|S_{th}, \phi_0^i)}{\partial s^k} \right]_s f_{S|\mathcal{A}_{R_L,1}}(S_{th}) p_\phi \mathrm{d}S_{th}, \tag{2.21}$$

where $s = \frac{m_s \gamma}{p\, g_{max}\, K\, S_{th}}$ *and* $\mathcal{L}_{I_{tot}}(s|S_{th}, \phi_0^i) = \exp(-\sigma^2 s)\mathcal{L}_I(s|S_{th}, \phi_0^i)$.

Proof. See Appendix A.5. □

2.4.2 Coverage Probability for minimum angular distance association scheme

In this scheme, the receiver searches and associates with the BS that has the minimum angular distance φ_c among all minimum angular distances detected from each beam's maxima. In this case, the receiver may lie anywhere in $b(\mathbf{o}, R_L)$ and φ_c also denotes the serving angular distance.

Remark 2.8. Considering infinitely large LOS ball radius, the Euclidean distance between the receiver and the serving BS may tend to infinity. In general, this scheme underestimates the performance. In a similar vein, if the receiver is associated with the nearest BS in Euclidean distance, the serving BS may lie near the boundaries of the 3dB beamwidth of the receiver's antenna, which is also not accurate and will (maybe significantly) underestimate the coverage performance. The aforementioned conceptual gap is resolved by adopting a more nuance user association policy which jointly considers both Euclidean and angular distances, that is the Policy 1.

Therefore, the serving distance $d_0 = \|x_0\|$ is now independent of the association policy and i.i.d. in $b(\mathbf{o}, R_L)$ with PDF given by $f_{d_0}(d_0) = \frac{2d_0}{R_L^2}$, $d_0 \in [0, R_L]$. The PDF of φ_c is first derived.

Lemma 2.9. *For a receiver equipped with* 2^m *sectors and conditioned on* $\mathcal{A}_{R_L,1}$ *the PDF of the closest angular distance* φ_c *is given by*

$$f_{\varphi_c|\mathcal{A}_{R_L,1}}(\varphi_c) = \frac{\lambda_{bs} 2^m R_L^2 \exp(-\lambda_{bs} 2^m \varphi_c R_L^2)}{1 - e^{-\lambda_{bs}\pi R_L^2}}, \tag{2.22}$$

for $\varphi_c \in \left[0, \frac{\pi}{2^m}\right]$.

Proof. See Appendix A.6. □

Lemma 2.10. *Conditioned on φ_c w.r.t. ϕ_0^r , the conditional Laplace transform $\mathcal{L}_I(s|\varphi_c, \phi_0^r)$ of the aggregate interference power distribution is given by*

$$\mathcal{L}_I(s|\varphi_c,\phi_0^r) = \exp\Big(-\lambda_{bs}\iint_{\boldsymbol{V}}\Big(1-\Big(1+\frac{s\,p\,K\,g_{max}\,g_{3gpp}(|\phi_0^r-\phi_x|)\,r_x^{-\alpha_L}}{m_x}\Big)^{-m_x}\Big)r_x\mathrm{d}\phi_x\mathrm{d}r_x\Big)$$
$$\times\exp\Big(-\lambda_{bs}\iint_{\boldsymbol{V}'}\Big(1-\Big(1+\frac{s\,p\,K\,g_{max}\,g_{3gpp}(|\phi_0^r-\phi_x|)\,r_x^{-\alpha_N}}{m_x}\Big)^{-m_x}\Big)r_x\mathrm{d}\phi_x\mathrm{d}r_x\Big), \tag{2.23}$$

where

$$\begin{aligned}\boldsymbol{V} &= \{(r_x,\phi_x)\in\mathbb{R}^2|0\le r_x\le R_L,\ \varphi_c\le\phi_x\le 2\pi\},\\ \boldsymbol{V}' &= \{(r_x,\phi_x)\in\mathbb{R}^2|R_L\le r_x\le R,\ \varphi_c\le\phi_x\le 2\pi\}.\end{aligned} \tag{2.24}$$

Proof. See Appendix A.7. □

Theorem 2.11. *Conditioned on $\mathcal{A}_{R_L,1}$, the coverage probability of a receiver in a mmWave network inside $b(\mathbf{o},R_L)$ under a minimum angular distance-based association policy is given by*

$$\mathcal{P}_c(\gamma)=\sum_{i=1}^{2^m}\sum_{k=0}^{m_s-1}\int_0^{\frac{\pi}{2^m}}\int_0^{R_L}\frac{(-s)^k}{k!}\left[\frac{\partial^k\mathcal{L}_{I_{tot}}(s|\varphi_c,\phi_0^i)}{\partial s^k}\right]_s p_\phi f_{d_0}(d_0)f_{\varphi_c|\mathcal{A}_{R_L,1}}(\varphi_c)\mathrm{d}d_0\mathrm{d}\varphi_c, \tag{2.25}$$

$s=\frac{m_s\gamma}{p\,g_{max}\,K\,g(\varphi_c)d_0^{-\alpha_L}}$ $\mathcal{L}_{I_{tot}}(s|\varphi_c,\phi_0^i)=\exp(-\sigma^2 s)\mathcal{L}_I(s|\varphi_c,\phi_0^i)$.

Proof. See Appendix A.8. □

2.4.3 Coverage Probability for minimum Euclidean distance association scheme

In this scheme, the receiver associates with the closest BS in Euclidean distance. Once the communication link has been established, all $x\in\Psi_{bs}^!$ interfere to the receiver with AoAs $\phi_x\sim U[-\pi,\pi]$. The Laplace transform of the aggregate interference power distribution can now be directly derived in the following Lemma.

Lemma 2.12. *The Laplace transform of the aggregate interference power distribution conditioned on the serving distance r_1 is given by*

$$\mathcal{L}_I(s|r_1)=\exp\Big(-\lambda_{bs}\iint_{\mathbf{Q}}\Big(1-\Big(1+\frac{s\,p\,K\,g_{max}\,g_{3gpp}(\phi_x)\,r_x^{-\alpha_L}}{m_x}\Big)^{-m_x}\Big)r_x\mathrm{d}\phi_x\mathrm{d}r_x\Big)$$
$$\times\exp\Big(-\lambda_{bs}\iint_{\mathbf{Q}'}\Big(1-\Big(1+\frac{s\,p\,K\,g_{max}\,g_{3gpp}(\phi_x)\,r_x^{-\alpha_N}}{m_x}\Big)^{-m_x}\Big)r_x\mathrm{d}\phi_x\mathrm{d}r_x\Big), \tag{2.26}$$

where

$$\begin{aligned}\mathbf{Q} &= \{(r_x, \phi_x) \in \mathbb{R}^2 | r_1 \leq r_x \leq R_L,\ -\pi \leq \phi_x \leq \pi\},\\ \mathbf{Q}^{'} &= \{(r_x, \phi_x) \in \mathbb{R}^2 | R_L \leq r_x \leq R,\ -\pi \leq \phi_x \leq \pi\}.\end{aligned} \tag{2.27}$$

Proof. The proof for deriving Lemma 2.12 follows similar steps as the one of Lemma 2.10. □

Theorem 2.13. *Conditioned on $\mathcal{A}_{R_L,1}$, the coverage probability of a receiver in a mmWave network inside $b(\mathbf{o}, R_L)$ under minimum Euclidean distance association policy is given by*

$$\mathcal{P}_c(\gamma) = \sum_{k=0}^{m_s-1} \int_0^{R_L} \frac{(-s)^k}{k!} \left[\frac{\partial^k \mathcal{L}_{I_{tot}}(s|r_1)}{\partial s^k}\right]_{s=\frac{m_s \gamma r_1^{\alpha_L}}{p\, K\, g_{max}^2}} f_{r_1|\mathcal{A}_{R_L,1}}(r_1) \mathrm{d}r_1, \tag{2.28}$$

where $\mathcal{L}_{I_{tot}}(s|r_1) = \exp(-\sigma^2 s)\mathcal{L}_I(s|r_1)$ *and* $f_{r_1|\mathcal{A}_{R_L,1}}(r_1) = \frac{2\pi\lambda_{bs} r_1 e^{-\lambda_{bs}\pi r_1^2}}{1-e^{-\lambda\pi r^2}}$, $r_1 \in [0, R_L]$.

Proof. The proof for deriving Theorem 2.13 follows similar steps as the proof in Theorem 2.7. □

2.5 Special Cases: Dominant Interferer Approach

The dominant interferer approach has been widely used in the literature due to its usefulness when the exact analysis is too complicated or leads to unwieldy results. For instance, in [34]–[37], the authors capture the effect of the dominant interferer while approximating the residual interference with a mean value. In this section, in order to understand the effect of the different potential definitions of the dominant interferer on the performance analysis, the coverage performance is investigated under the assumption of neglecting all but a single dominant interferer for all policies. Note that in order to define the interferer as dominant, the latter is restricted to $b(\mathbf{o}, R_L)$. Accordingly, a performance comparison between the dominant interferer approaches with the exact performance of Policy 1, is conducted. To this end, the noise power is assumed to be negligible as compared to the aggregate interference experienced at the receiver, i.e., interference-limited scenarios [3] Policy 2 and Policy 3 are considered and coverage probability, i.e., $\mathcal{P}_c(\gamma) \triangleq 1 - F_{\mathrm{SIR}}(\gamma)$, analysis is conducted in terms of the achieved SIR.

[3]Please note, that since interference from other BSs is ignored, it results in stochastic dominance of the SIR as compared to the exact SIR of the respective policy, which implies that the dominant interferer approach yields a bound on the exact coverage probability of Policy 1.

2.5.1 Coverage Probability Under Policy 1

By considering maximum power user association policy, the receiver associates with the BS providing the maximum power as described in subsection 2.3.5. Then, clearly the dominant interferer is the BS which provides the second most powerful received power after the serving BS. The received SIR for this dominant interferer analysis of Policy 1 can be written as

$$\text{SIR} = \frac{h_1 Pr_0}{h_2 Pr_I}, \tag{2.29}$$

where the maximum received power $Pr_0 = S$ and Pr_I denotes the second most powerful received power. Once the receiver attaches to the serving BS, Pr_0 and Pr_I are no longer independent. In this case, the joint PDF of Pr_0 and Pr_I is required for the coverage probability analysis, which is given next.

Lemma 2.14. *Conditioned on $\mathcal{A}_{R_L,2}$, the joint PDF of Pr_0 and Pr_I is given by*

$$f_{Pr_0,Pr_I|\mathcal{A}_{R_L,2}}(s_0, s_I) = \frac{(\lambda_{bs}\pi R_L^2)^2 e^{\lambda_{bs}\pi R_L^2\left(F_{S_x}(s_0)-1\right)} f_{S_x}(s_0) f_{S_x}(s_I)}{1-\Gamma(2, \lambda_{bs}\pi R_L^2)}, \tag{2.30}$$

where $s_0 \in [w_{min}, \infty]$ and $s_I \in [w_{min}, s_0]$.

Proof. See Appendix A.9 □

Having obtained $f_{Pr_0,Pr_I|\mathcal{A}_{R_L,2}}(s_0, s_I)$, it becomes mathematically convenient to statistically characterize the SIR as $\text{SIR} = P \cdot Q$, where $P = \frac{Pr_0}{Pr_I}$ and $Q = \frac{h_1}{h_2}$.

Lemma 2.15. *Conditioned on $\mathcal{A}_{R_L,2}$, the PDF of P is given by*

$$f_{P|\mathcal{A}_{R_L,2}}(p_0) = \int_{p_{min}(p_0)}^{\infty} p_0 f_{Pr_0,Pr_I|\mathcal{A}_{R_L,2}}(p_0 s_I, s_I)\mathrm{d}s_I, \tag{2.31}$$

where $p_0 \in [1, \infty]$ and $p_{min}(p_0) = \max\left\{\frac{w_{min}}{p_0}, w_{min}\right\}$.

Proof. The proof results directly from the formula for the PDF of ratio of two dependent random variables. □

Lemma 2.16. *Conditioned on $\mathcal{A}_{R_L,2}$, the PDF of Q is given by*

$$f_{Q|\mathcal{A}_{R_L,2}}(q) = \frac{q^{m_s-1} m_s^{m_s} m_x^{m_x} \Gamma(m_s+m_x)}{\Gamma(m_s)\Gamma(m_x)(qm_s+m_x)^{(m_s+m_x)}}, \tag{2.32}$$

where $q \in [0, \infty]$.

Proof. The proof results directly from the formula for the PDF of ratio of two independent random variables. □

Proposition 2.17. *Conditioned on $\mathcal{A}_{R_L,2}$, the coverage probability in the presence of a dominant interferer under Policy 1 is given by*

$$\mathcal{P}_c(\gamma) = 1 - \int_0^{\gamma} \int_1^{\infty} \frac{1}{x} f_{P|\mathcal{A}_{R_L,2}}(x) f_{Q|\mathcal{A}_{R_L,2}}\Big(\frac{x}{p_0}\Big) \mathrm{d}p_0 \mathrm{d}x. \tag{2.33}$$

Proof. See Appendix A.10 □

2.5.2 Coverage Probability Under Policy 2

By assuming that the receiver associates with the closest BS in angular distance, the dominant interferer is the second nearest BS in angular distance w.r.t the maxima of the receiving beam, as described in subsection 2.3.5. Without loss of generality, the receiving beam's maxima is assumed to be along the x-axis.[4] In this case, the received SIR is given by

$$\mathsf{SIR} = \frac{g(|\varphi_1|) h_1 d_1^{-\alpha_L}}{g(|\varphi_2|) h_2 d_2^{-\alpha_L}}, \tag{2.34}$$

where $f_{d_i}(d_i) = \frac{2d_i}{R_L^2}$, $i \in \{1,2\}$ denotes the distance of the serving BS and the dominant interferer, respectively, $|\varphi_1|, |\varphi_2|$ denote the nearest and the second nearest absolute angular distances of the serving and interfering BS from the direction of the receiving beam's maximum directivity, and $h_1 = h_s, h_2 = h_x$, for notational convenience, respectively. Note that in order to define the interferer as "dominant", the angle $|\varphi_2|$ is restricted to $|\varphi_2| < \phi_A$, i.e., the dominant interferer is assumed to fall in the mainlobe part of the receiver's antenna pattern. Let $T_{\phi_A,2}$ define the event that 2 BSs (assumed to lie in $b(\mathbf{o}, R_L)$) fall in the mainlobe part of the receiver's antenna. Note that $T_{\phi_A,2} \subseteq \mathcal{A}_{R_L,2}$. Once the receiver attaches to the closest BS at $|\varphi_1|$, the angular distances $|\varphi_1|, |\varphi_2|$ are no longer independent. In this case, it is mathematically convenient to statistically characterize the SIR as $\mathsf{SIR} = G \cdot W$, where $G = \frac{g(|\varphi_1|)}{g(|\varphi_2|)}$ and $W = \frac{h_1 d_1^{-\alpha_L}}{h_2 d_2^{-\alpha_L}}$.

[4] As the scope of this section is merely to address the impact of the dominant interferer in the coverage performance of mmWave networks, the exhaustive scanning procedure for the association policy proposed in subsection 2.3.5 is not considered here as the location of the dominant interferer is independent of the considered reference line.

Lemma 2.18. *Conditioned on $T_{\phi_A,2}$, the PDF of G is given by*

$$f_{G|T_{\phi_A,2}}(g) = \frac{1}{\mathbb{P}[T_{\phi_A,2}]} \int_{g_s}^{\frac{g_{max}}{g}} \frac{5\left(\lambda_{bs} R_L^2 \phi_{3dB}\right)^2}{24\, g\, g_2} \frac{\sqrt{\log_{10}\left(\frac{g_{max}}{g_2}\right)\log_{10}\left(\frac{g_{max}}{g\, g_2}\right)}}{\ln\left(\frac{g_{max}}{g_2}\right)\ln\left(\frac{g_{max}}{g\, g_2}\right)} \times \exp\left(\frac{\lambda_{bs} R_L^2 \phi_{3dB} \sqrt{10\log_{10}(g_{max}/g_2)}}{2\sqrt{3}}\right) \mathrm{d}g_2, \tag{2.35}$$

with $g \in [1, g_{max}/g_s]$ and

$$\mathbb{P}[T_{\phi_A,2}] = \frac{1 - e^{-\lambda_{bs} R_L^2 \phi_A} - \lambda_{bs} R_L^2 \phi_A e^{-\lambda_{bs} R_L^2 \phi_A}}{1 - \frac{\Gamma(2, \lambda_{bs}\pi R_L^2)}{\Gamma(2)}}. \tag{2.36}$$

Proof. See Appendix A.11. □

Lemma 2.19. *Conditioned on $\mathcal{A}_{R_L,2}$, the PDF of W is given by*

$$f_{W|\mathcal{A}_{R_L,2}}(w) = \int_0^\infty \frac{4 w_2^{-\frac{4}{\alpha_L}-1} (m_s m_x)^{-\frac{2}{\alpha_L}}}{w^{\frac{2}{\alpha_L}+1} \alpha_L^2 R_L^4} \times \frac{\left[\Gamma\left(\frac{2}{\alpha_L}+m_s\right) - \Gamma\left(\frac{2}{\alpha_L}+m_s, \frac{m_s w w_2}{R_L^{-\alpha_L}}\right)\right]\left[\Gamma\left(\frac{2}{\alpha_L}+m_x\right) - \Gamma\left(\frac{2}{\alpha_L}+m_x, \frac{m_x w_2}{R_L^{-\alpha_L}}\right)\right]}{\Gamma(m_s)\Gamma(m_x)} \mathrm{d}w_2, \tag{2.37}$$

with $w \in (0, \infty)$.

Proof. See Appendix A.12. □

Proposition 2.20. *Conditioned on $\mathcal{A}_{R_L,2}$ and $T_{\phi_A,2}$, the coverage probability in the presence of a dominant angular distance-based interferer under Policy 2 is given by*

$$\mathcal{P}_c(\gamma) = 1 - \int_0^\gamma \int_1^{\frac{g_{max}}{g_s}} \frac{1}{g} f_{W|\mathcal{A}_{R_L,2}}(x/g) f_{G||T_{\phi_A,2}}(g) \mathrm{d}g \mathrm{d}x. \tag{2.38}$$

Proof. See Appendix A.13. □

2.5.3 Coverage Probability Under Policy 3

In this scenario, according to Policy 3 the dominant interferer is the second closest BS in Euclidean distance to the receiver. In this case, the received SIR is given by

$$\mathrm{SIR} = \frac{g_{max} h_1 r_1^{-\alpha_L}}{g(|\varphi_2|) h_2 r_2^{-\alpha_L}}, \tag{2.39}$$

where r_1, r_2 denote the distances of the serving and the dominant interfering BS from the receiver and $|\varphi_2|$ here denotes the absolute angular distance of the interfering node as seen from the receiver. For the dominant interferer scenario, the property of PPP is exploited: If $|\varphi_2| \sim U[0,\pi]$, $|\varphi_2|$ remains uniform in the subset $[0,\phi_A]$ i.e., $|\varphi_2| \sim U[0,\phi_A]$. In this scenario, r_1, r_2 are dependent. The SIR can be written as $\mathsf{SIR} = G \cdot W$, where $G = \frac{g_{max} h_1}{g(|\varphi_2|) h_2}$ and $W = \frac{r_1^{-\alpha_L}}{r_2^{-\alpha_L}}$.

Lemma 2.21. *Conditioned on $\mathcal{A}_{R_L,2}$, $f_{G|\mathcal{A}_{R_L,2}}(g)$ is given by*

$$f_{G|\mathcal{A}_{R_L,2}}(g) = \frac{5\sqrt{3}\left(\frac{m_s}{g_{max}}\right)^{m_s} {m_x}^{m_x} \phi_{3dB}}{6\sqrt{10}\ln(10)\Gamma(m_s)\Gamma(m_x)\phi_A} \int_0^{\infty} \int_{\frac{z}{g_{max}}}^{\frac{z}{g_s}} \frac{(g\,z)^{m_s-1} e^{-\frac{m_s g z}{g_{max}} - m_x x} x^{m_x-1}}{\sqrt{\log_{10}(x g_{max}/z)}} \mathrm{d}x\,\mathrm{d}z. \tag{2.40}$$

Proof. See Appendix A.14. □

Lemma 2.22. *Conditioned on $\mathcal{A}_{R_L,2}$, $f_{W|\mathcal{A}_{R_L,2}}(w)$ is*

$$f_{W|\mathcal{A}_{R_L,2}}(w) = \frac{\left(\frac{1}{w}\right)^{\frac{2+\alpha_L}{\alpha_L}}}{\alpha_L} \left(\frac{3\mathrm{erf}(\sqrt{\pi\lambda_{bs}})}{2\lambda_{bs}} - 2(1 + R_L^2 \lambda_{bs}\pi) e^{-R_L^2 \lambda_{bs}\pi} - e^{-\lambda_{bs}\pi} \right) \tag{2.41}$$

$w \in [1,\infty)$, and $\mathrm{erf}(\cdot)$ denotes the error function [40, eq. (8.250.1)].

Proof. See Appendix A.15. □

Proposition 2.23. *Conditioned on $\mathcal{A}_{R_L,2}$, the coverage probability in the presence of a dominant interferer under Policy 3 is given by*

$$\mathcal{P}_c(\gamma) = 1 - \int_0^{\gamma} \int_1^{\infty} \frac{1}{g} f_{W|\mathcal{A}_{R_L,2}}(x/g) f_{G|\mathcal{A}_{R_L,2}}(g) \mathrm{d}g \mathrm{d}x. \tag{2.42}$$

Proof. The proof follows the same steps as the proof in Proposition 2.17. □

2.6 Special Cases: A BPP mmWave Network under Perfect Alignment

In the previous subsection, the definition of the dominant interferer in mmWave networks, where the BSs were assumed to be deployed according to a FHPPP in a LOS ball, was revisited and its effect in the coverage performance was addressed. Nevertheless, in practical mmWave networks, a finite and predetermined number of mmWave small BSs is usually

deployed in a finite region. This subsection provides an in-depth performance analysis of a practical scenario where the BSs are assumed to be spatially distributed according to a BPP. In order to merely capture the effect of the dominant interferer in mmWave networks, perfect alignment between the direction of the UE's and the receiver's antenna is assumed. Moreover, in a similar to subsection 2.5 vein, the BSs are assumed to lie in $b(\mathbf{o}, R_L)$.

Towards this direction, in this subsection a coverage probability analysis is conducted under three key interference scenarios: i) a worst-case dominant interference scenario, where the dominant interferer is the BS that is both the nearest in azimuthal angle from the direction of the serving BS, and the second nearest in Euclidean distance from the receiver; ii) a dominant interferer, where the dominant interferer is defined as the BS that is the closest in azimuthal angle from the direction of the serving BS and uniformly distributed in an annulus formed by the the serving distance and a ball radius R_L, and iii) the aggregate interference in the BPP mmWave network, for completeness.

2.6.1 System Model and Assumptions

In this subsection, the BSs are spatially distributed according to a uniform BPP. Accordingly, a fixed and finite number N of BSs is uniformly and independently distributed in $b(\mathbf{o}, R_L)$. In this case, only the first branch of (2.7) is exploited, i.e., $l(\|x\|) = K\|x\|^{-\alpha_L}$, for $\|x\| \in [0, R_L]$. By further letting $\phi_0^r = 0$, the equations for the antenna patterns for both the UE and the BSs are given by (2.4) and (2.6), where $\phi \in [-\pi, \pi]$. In the following, the absolute angular distance $|\phi|$ is considered. Since $\phi \in [-\pi, \pi]$, we define $|\phi| \in [0, \pi]$. This notation is particularly useful when dealing with the angular distance from the direction of the maximum directivity in antenna beampatterns.

In order to elaborate more on practical system-level insights for the effect of the dominant interferer in the coverage performance of mmWave networks, the minimum distance-based association policy is considered for the receiver. Accordingly, the receiver is associated to the nearest BS in $b(\mathbf{o}, R_L)$ located at x_0 and is referred to as the serving BS. Since the uniform BPP in $b(\mathbf{o}, R_L)$ is rotation invariant around the origin, it is assumed without loss of generality that x-axis is aligned with the line connecting the receiver and the serving BS referred to as the communication link, as shown in Fig. 2.4. Also, the maximum gain of the N BSs' antennas is assumed to be always directed towards the receiver for the sake of mathematical tractability. Once the communication link has been established, the best receiving beam is selected by the receiver for reception. Now, according to the beam management procedures in 5G NR presented in detail in subsection 2.3.5, the beam pointing towards the serving BS is chosen by the receiver as the receiving beam. By steering the receiver's antenna, the maximum gain of the receiver's antenna is assumed to be directed towards the serving BS. The complete scenario is illustrated in Fig. 2.4.

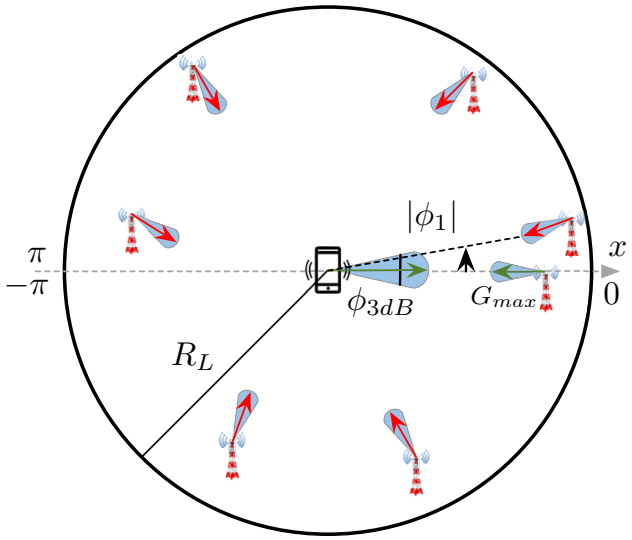

Figure 2.4: Illustration of a special case of the system model presented in subsection 2.3 with i) perfect alignment and, ii) the BSs forming a BPP in $b(\mathbf{o}, R_L)$.

2.6.2 SINR Definitions

As mentioned in the beginning of subsection 2.6, in order to capture and demonstrate the effect of the angular distances on the directional gain and consequently, on the experienced received SINR, three interference scenarios are considered: i) the worst-case dominant interferer approach, ii) a dominant interferer approach, and iii) the aggregate interference in $b(\mathbf{o}, R_L)$.

Dominant Interferer Worst-Case Approach. In this setup, the worst-case dominant interfer scenario is considered and its effect on the received SINR is accurately captured. The interference from the rest $N-2$ interfering BSs is assumed to be negligible as compared to the interference caused by the dominant interferer. In the absence of fading, the dominant interferer is the nearest BS in angle $|\phi|$ w.r.t. the line of the communication link, i.e., at $|\phi_1|$ as shown in Fig. 1, and the second nearest in Euclidean distance from the receiver, i.e., at r_2. In this case, the SINR at the receiver is given by

$$SINR_{w-dom} = \frac{p\, g_{max}\, g_{max}\, l(||x_0||)}{p\, g_{max}\, g(|\phi_1||\phi_1| < \phi_A) l(r_2) + \sigma^2}, \tag{2.43}$$

By assuming dominant interference, the angle $|\phi_1|$ is restricted to $|\phi_1| < \phi_A$, i.e., the dominant interferer is assumed to fall in the mainlobe of the receiver's antenna.

Dominant Interferer Approach. In this setup, a common dominant interferer scenario is considered and its effect on the received SINR is accurately captured. In the absence of fading, the dominant interferer is the nearest BS in angle $|\phi|$ w.r.t. the line of the communication link, i.e., at $|\phi_1|$, and uniformly distributed in $b(\mathbf{o}, R_L) \setminus b(\mathbf{o}, ||x_0||)$, at distance d_i. In this

case, the SINR at the receiver is given by

$$SINR_{dom} = \frac{p\, g_{max}\, g_{max}\, l(||x_0||)}{p\, g_{max}\, g(|\phi_1|||\phi_1| < \phi_A) l(d_i) + \sigma^2}. \tag{2.44}$$

Note that the angle $|\phi_1|$ is again restricted to $|\phi_1| < \phi_A$.

Aggregate Interference. In this setup, the aggregate interference in $b(\mathbf{o}, R_L)$ is considered in the definition of the SINR. In this case, the SINR at the receiver is given by

$$SINR_{agg} = \frac{p\, h_s\, g_{max}\, g_{max}\, l(||x_0||)}{I + \sigma^2}, \tag{2.45}$$

where I is given by $I = \sum_{i=1}^{N-1} p\, h_i\, g_{max}\, g_{3gpp}(|\varphi_i|)\, l(U_i)$ and refers to the aggregate interference power. The term $\{U_i\}_{i=1}^{N-1}$ denotes the distance between the interfering BSs and the receiver. The spatial AoA $|\varphi_i|$, determines the receiver antenna gain towards the i-th interferer, and is assumed to be uniformly distributed in $[0, \pi]$. Please note that (2.45), considers the exact expression for the antenna pattern of the BSs while calculating the aggregate interference power.

2.6.3 Performance Analysis

In this section, performance analysis in terms of coverage probability is conducted.

Coverage Probability Under Worst-Case Dominant Interference. The conditional PDF of $g(|\phi_1|||\phi_1| < \phi_A)$ is first calculated as an intermediate step in the coverage probability analysis.

Lemma 2.24. *Conditioned on $|\phi_1| < \phi_A$, the conditional PDF of the gain $g(|\phi_1|||\phi_1| < \phi_A)$ is given by*

$$f(g||\phi_1| < \phi_A) = \frac{f(g, |\phi_1| < \phi_A)}{p_{|\phi_1|<\phi_A}}, \tag{2.46}$$

where

$$f(g, |\phi_1| < \phi_A) = \frac{5}{3\, g \ln(10)} \frac{\phi_{3dB}}{2} \frac{N}{\pi^N} \sqrt{\frac{3}{10 \log_{10}\left(\frac{g_{max}}{g}\right)}} \left(\pi - \frac{\phi_{3dB}}{2} \sqrt{\frac{10 \log_{10}\left(\frac{g_{max}}{g}\right)}{3}}\right)^{N-1}, \tag{2.47}$$

where $g \in [g_s, g_{max}]$ and $p_{|\phi_1|<\phi_A} = 1 - \pi^{-N}(\pi - \phi_A)^N$.

Proof. See Appendix A.16. □

The coverage probability of the receiver can now be obtained in exact form.

Proposition 2.25. *The coverage probability of a receiver in $b(\mathbf{o}, R_L)$ in the presence of a dominant worst-case interference scenario is given by*

$$\mathcal{P}_c(\gamma) = \int_{g_s}^{g_0(r_1,r_2,\gamma,\sigma^2)} \int_{r_1}^{R_L} \int_0^{R_L} f_{r_1,r_2}(r_1,r_2) f(g, |\phi_1| < \phi_A) \mathrm{d}r_1 \mathrm{d}r_2 \mathrm{d}g, \tag{2.48}$$

where $r_1 = ||x_0||$, *and* $f_{r_1,r_2}(r_1,r_2) = N(N-1)\frac{2\,r_1}{R_L^2}\frac{2\,r_2}{R_L^2}\left(1-\left(\frac{r_2}{R_L}\right)^2\right)^{N-2}$, $g_0(r_1,r_2,\gamma,\sigma^2) = \min\{\psi(r_1,r_2,\gamma,\sigma^2), g_{max}\}$, $\psi(r_1,r_2,\gamma,\sigma^2) = \frac{c_{bs}\, g_{max}\, r_1^{-\alpha_L} - \gamma\,\sigma^2}{c_{bs}\gamma\, r_2^{-\alpha_L}}$, *and* $c_{bs} = K\, p_0\, g_{max}$.

Proof. See Appendix A.17. □

Coverage Probability Under Dominant Interference. In this approach, it is mathematically convenient to first derive the PDF of $P = g(|\phi_1|||\phi_1| < \phi_A) d_i^{-\alpha_L}$, conditioned on the serving distance $r_1 = ||x_0||$.

Lemma 2.26. *Conditioned on $|\phi_1| < \phi_A$ and $r_1 = ||x_0||$, the conditional PDF of $P = g(|\phi_1|||\phi_1| < \phi_A) d_i^{-\alpha_L}$ is given by*

$$f_P(x||\phi_1| < \phi_A, r_1) = \int_{\eta(x)}^{\theta(x)} \frac{1}{y} f_{d_i^{-\alpha_L}}(y/x|r_1) f_{g_{3gpp}}(y||\phi_1| < \phi_A) \mathrm{d}y, \tag{2.49}$$

where $x \in [g_s\, R_L^{-\alpha_L}, g_{max}\, r_1^{-\alpha_L}]$, $\eta(x) = \max\left\{g_s, \frac{x}{r_1^{-\alpha_L}}\right\}$, $\theta(x) = \min\left\{g_{max}, \frac{x}{R_L^{-\alpha_L}}\right\}$, $f_{d_i^{-\alpha_L}}(d|r_1) = \frac{2\, d^{(\alpha_L+2)/\alpha_L}}{\alpha_L(R_L^2 - r_1^2)}$ *and y is a dummy variable.*

Proof. See Appendix A.18. □

An exact expression for the coverage probability of the receiver can now be obtained.

Proposition 2.27. *The coverage probability of a receiver in $b(\mathbf{o}, R_L)$ in the presence of a dominant interference scenario is given by*

$$\mathcal{P}_c(\gamma) = \int_{g_s R_L^{-\alpha_L}}^{\omega(r_1,\gamma,\sigma^2)} \int_0^{R_L} f_P(x||\phi_1| < \phi_A, r_1) f_{r_1}(r_1) \mathrm{d}r_1 \mathrm{d}x, \tag{2.50}$$

where $\omega(r_1,\gamma,\sigma^2) = \min\left\{g_{max} r_1^{-\alpha_L}, \frac{c_{bs} g_{max} r_1^{-\alpha_L} - \gamma\sigma^2}{c_{bs}\gamma}\right\}$ *and $f_{r_1}(r_1)$ is given by*

$$f_{r_1}(r_1) = \frac{2N}{r_1}\left(\frac{r_1}{R_L}\right)^2\left(1-\left(\frac{r_1}{R_L}\right)^2\right)^{N-1}. \tag{2.51}$$

Proof. The proof is analogous to that of Proposition 2.25, with a different PDF $f_{r_1}(r_1)$ for the serving distance given by [46], required for deconditioning on the conditional coverage probability. □

Coverage Probability Under Aggregate Interference. Conditioned on the serving distance $r_1 = ||x_0||$, the Laplace transform of interference power distribution is obtained as intermediate step in the coverage probability analysis.

Lemma 2.28. *The Laplace transform of the aggregate interference power distribution conditioned on the serving distance r_1 is given by*[5]

$$\mathcal{L}_I(s|r_1) = \left[\frac{1}{\pi}\int_{r_1}^{R_L}\int_0^{\pi}\left(1+\frac{s\,c_{bs}\,g_{3gpp}(|\varphi_i|)\,u_i^{-\alpha_L}}{m_I}\right)^{-m_I}\frac{2u_i}{R_L^2-r_1^2}\mathrm{d}|\varphi_i|\,\mathrm{d}u_i\right]^{N-1}. \tag{2.52}$$

Proof. See Appendix A.19. □

The exact expression of the coverage probability for the receiver under aggregate interference can now be derived.

Proposition 2.29. *The coverage probability of a receiver in $b(\mathbf{o}, R_L)$ is given by*

$$\mathcal{P}_c(\gamma) = \int_0^{R_L}\sum_{k=0}^{m_s-1}\frac{(-s)^k}{k!}\left[\frac{\partial^k\mathcal{L}_{I_{tot}}(s|r_1)}{\partial s^k}\right]_s f_{r_1}(r_1)\mathrm{d}r_1, \tag{2.53}$$

where $s = \frac{m_s\gamma r^{\alpha_L}}{c_{bs}g_{max}}$ and $\mathcal{L}_{I_{tot}}(s|r_1) = \exp(-\sigma^2 s)\mathcal{L}_I(s|r_1)$.

Proof. The proof for deriving Proposition 2.29 follows similar lines as the one presented in [47, Appendix F]. □

2.7 Numerical Results and Discussions

2.7.1 Coverage Performance of FHPPP 5G NR mmWave Networks

In this section, numerical results are presented to evaluate and compare the performance achieved in a dense FHPPP mmWave cellular network under the different association policies as presented in subsection 2.3.5. The accuracy of the analytical results presented in this chapter is verified by comparing them with the empirical results obtained from Monte-Carlo simulations. For all numerical results, the following parameters have been used unless stated otherwise: $R_L = 75$ meters, $\alpha_L = 2$, $\alpha_N = 3.5$, $f_c = 26.5$ GHz as in [24] and $R = 100$ meters. As per the 3GPP specifications $p = 45$ dBm, $\sigma^2 = -74$ dBm, $\lambda_{bs} = 0.0008$ BSs/m^2 and

[5] Although the Laplace transform of the aggregate interference was derived using the realistic pattern given by (2.1) because of its compact form, the same result can be derived by using (2.2). However, the Laplace transform using the two-branch expression in (2.2) results in a non-compact form and hence it is omitted here for brevity.

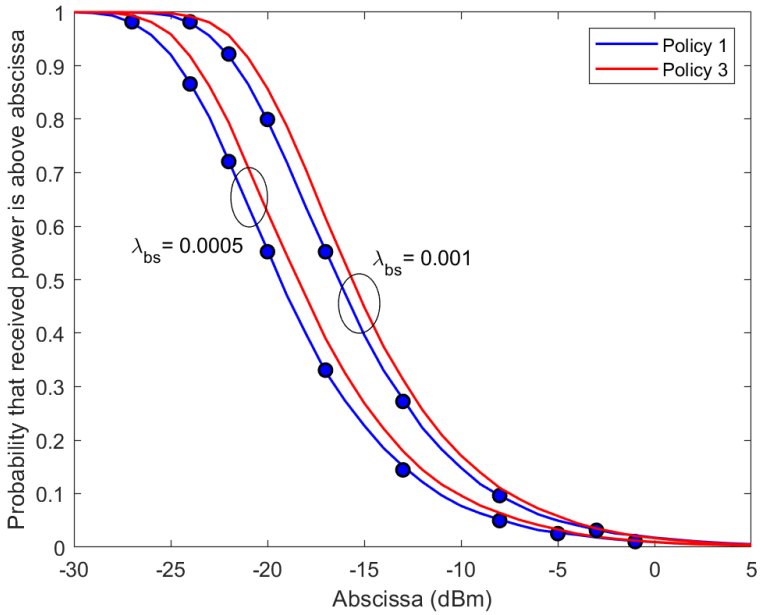

Figure 2.5: CCDF of received power under Policy 1 and Policy 3, for different values of λ_{bs}. Markers denote the analytical results.

$m_u = 2$. The receiver is assumed to be equipped with a directional antenna with 4 sectors[6], i.e., $m = 2$ and $\phi_{3dB} = \pi/2$.

Fig. 2.5 presents the CCDF of the maximum received power under Policy 1, defined as in (2.16) and evaluated through Lemma 2.3, for different values of λ_{bs}. To address and highlight the impact of realistic association schemes in the performance of mmWave networks, the results are compared through simulations to the received power of Policy 3, defined as $S_r = g_{max} r_1^{-\alpha_L}$, where the receiver is associated to the nearest LOS BS and no misalignment error exists. It is observed that Policy 3 overestimates the received power compared to the maximum received power achieved under Policy 1, especially for small values of the abscissa. Interestingly, notice that the misalignment error exists even in denser mmWave networks. Consequently, associating to the nearest LoS BS is not realistic, even in dense mmWave networks.

Fig. 2.6 compares the coverage probability versus γ_{th} under Policy 1 and Policy 3 for several numbers of beams/sectors produced by the receiver antenna. It is observed that the

[6]Very large codebooks can be considered at the receiver, thereby resulting in a huge number of narrow beams. However, [48] states that the SSB-based requirements upper-bound the number of RX beams to 8. Besides, to avoid the high overhead and complexity issues associated with wide spatial domain coverage with a huge number of very narrow beams, on which CSI-RSs are transmitted, it is reasonable to consider only subsets of those beams, usually based on the locations of the active receiver. This is also important for UE power consumption considerations.

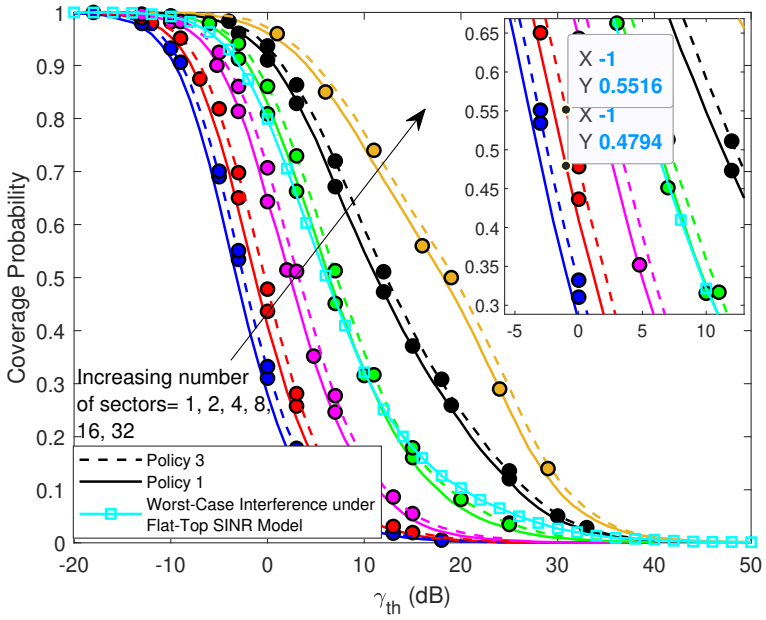

Figure 2.6: Coverage probability versus γ_{th} under Policy 1 and Policy 3, for different number of sectors. Simulation results under a flat-top antenna pattern are also presented for completeness.

coverage performance of the network under Policy 3 is overestimated and the difference in coverage performance is not negligible (e.g. for $\gamma_{th} = -1$ dB, the coverage probability under Policy 3 is 0.55, while the coverage probability under Policy 1 is 0.48). Note that in Policy 1, the receiver performs exhaustive scanning in each sector to select the BS that provides the maximum power. The number of beams/sectors of the receiver's antenna affects both the desired received power and the interference power falling within the 3dB beamwidth of the receiver's antenna pattern, while in Policy 3 the number of sectors only determines the interference power. Indeed, by increasing the number of sectors in Policy 1, the receiver minimizes the misalignment error. At the same time, the receiver's beams become highly-directional, thus decreasing the interference power, and the coverage performance approaches the corresponding one under Policy 3. The cyan curve depicts coverage performance for the worst-case interference scenario under the flat-top antenna pattern approximation. It is observed that the coverage performance under the flat-top pattern approximation is overestimated w.r.t. the performance under Policy 1, especially in the higher SINR regime. Therefore, the joint effect of the approximation of the flat-top antenna pattern and perfect alignment on the coverage performance under Policy 1, is captured.

Fig. 2.7 compares the coverage probability versus γ_{th} under Policy 1 and Policy 2 when the receiver's antenna is equipped with different number of sectors. In both of the association schemes, the receiver performs maximum power-based and angular distance-based exhaustive

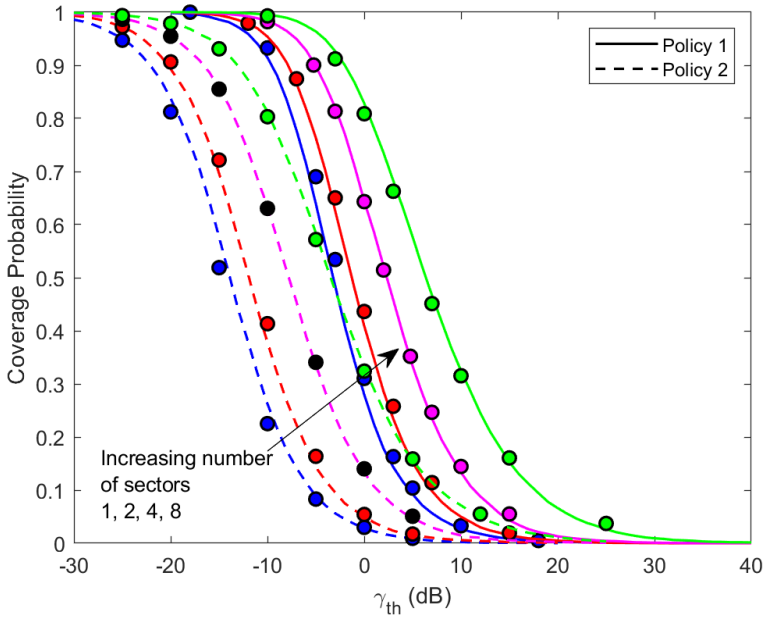

Figure 2.7: Coverage probability versus γ_{th} under Policy 1 and Policy 2, for several numbers of sectors. Markers denote the analytical results.

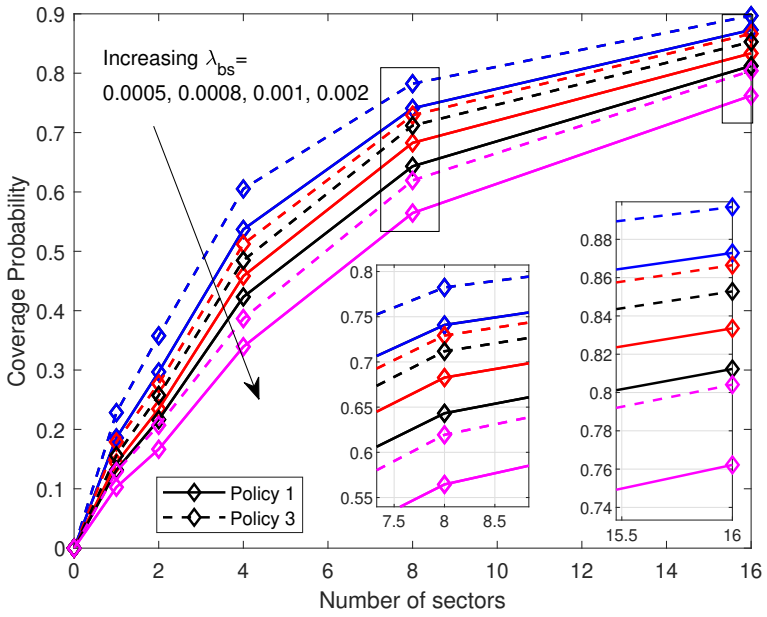

Figure 2.8: Coverage probability versus number of sectors under Policy 1 and Policy 3, for different values of λ_{bs} and $\gamma_{th} = 3$dB.

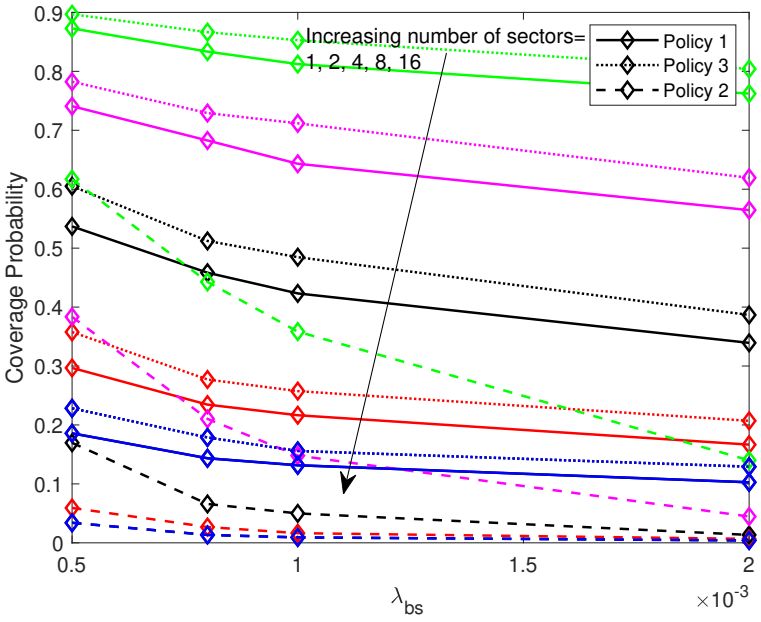

Figure 2.9: Coverage probability versus λ_{bs} for different number of sectors under the three policies, for $\gamma_{th} = 3$dB.

scanning, respectively to select the serving BS. It is observed that when only angular distance-based scanning is performed, the coverage performance is significantly underestimated. This result indicates that: i) Considering merely angular distance-based criteria for estimating the coverage performance is inaccurate ii) The path-loss plays a crucial role in the performance of mmWave networks.

Fig. 2.8 compares the coverage probability versus the number of sectors of the receiver's antenna under Policy 1 and Policy 3, derived analytically in Theorem 2.7 and Theorem 2.13, respectively, for different values of λ_{bs} and target $\gamma_{th} = 3$ dB. One can observe that the coverage performance under ideal baseline scenario overestimates the corresponding one under Policy 1, which accounts for the misalignment error, for all BSs' deployment densities. With the increase of the number of sectors, the UE's beams in Policy 1 become more directional which alleviates beam misalignment effects and the coverage performance approaches the corresponding one under the ideal baseline scenario. This also highlights the need for explicitly modeling of misalignment error for realistic antenna patterns, even a small misalignment error will impact the performance and hence, the angular distances become crucial in realistic performance analysis of mmWave networks.

Fig. 2.9 shows the coverage probability versus λ_{bs} for different number of sectors of the receiver's antenna, under the three policies. It is observed that Policy 3 slightly overestimates the coverage performance of the network for all number of sectors. On the other hand, it is clearly observed that Policy 2 significantly underestimates the network's cover-

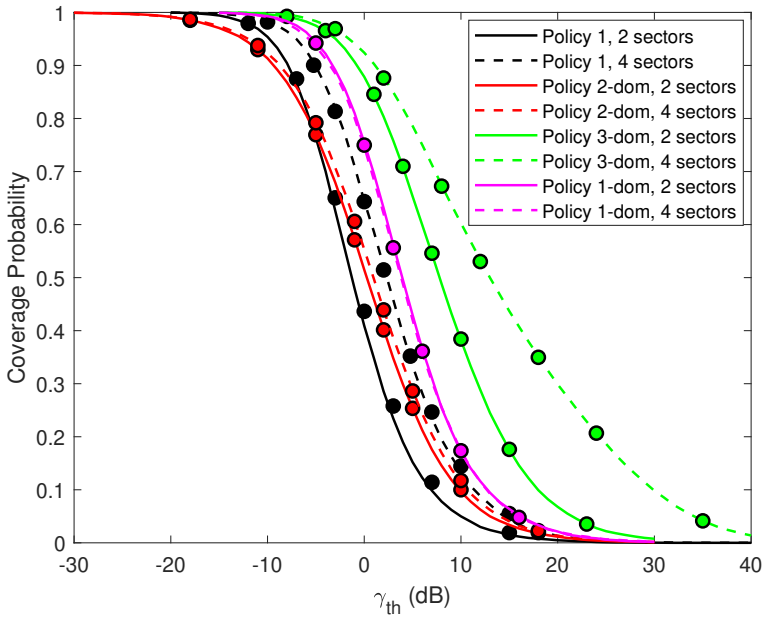

Figure 2.10: Coverage probability versus number of sectors under Policy 1 and Policy 3, for different values of λ_{bs} and $\gamma_{th} = 3$dB.

age performance. This result clearly confirms that path-loss cannot be ignored during the determination of the serving BS.

Fig. 2.10 shows the coverage probability versus γ_{th} under Policy 1, Policy 2 and Policy 3 for the dominant interferer. Moreover, the coverage performance under Policy 1 and aggregate interference is depicted, when the receiver's antenna is equipped with different number of sectors. Quite interestingly, it is observed that the coverage performance under Policy 2 with a single dominant interferer approximates the performance under Policy 1 with aggregate interference, especially when the number of sectors is small. In this case, the angular distance-based criterion results in realistic network performance. On the other hand, the performance under Policy 3 in the presence of a single dominant interferer clearly overestimates the corresponding one under Policy 1, which leads to the following system-level outcome: *In a LOS ball of a mmWave network under beam misalignment error at the receiver, by attaching to the closest BS in angular distance and considering the dominant interferer as the closest BS in angular distance w.r.t. the line of communication link, results in a more accurate approximation of the coverage performance compared to the policy of attaching to the closest LOS BS and considering the dominant interferer as the second nearest BS.* Notably, the performance of Policy 2 under dominant interferer approach yields a better approximation of the network's coverage than the corresponding performance under Policy 1 under dominant interferer approach.

Fig. 2.11 shows the coverage probability versus γ_{th} under Policy 1 and Policy 2 dominant

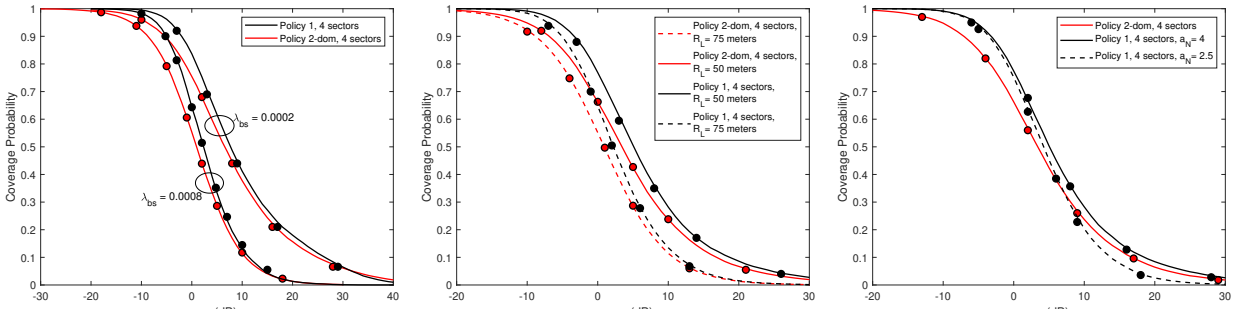

(a) Different values of λ_{bs}. (b) Different values of R_L (c) Different values of α_N.

Figure 2.11: Coverage probability versus γ_{th} under Policy 1 and Policy 2 dominant interferer approach. Markers denote the analytical results.

interferer approaches. This figure investigates different network setups for which the performance under Policy 2 dominant interferer approach yields a close approximation for the network's coverage performance. In Fig. 2.11a, coverage probability versus γ_{th} under Policy 1 and Policy 2 dominant interferer approach for different values of λ_{bs}, is illustrated. It is observed that the performance under Policy 2 dominant interferer approach closely approximates the network's coverage performance for both dense and sparse mmWave networks, especially in the higher SINR regime. In Fig. 2.11b, coverage probability versus γ_{th} under Policy 1 and Policy 2 dominant interferer approach for different values of R_L, is illustrated. In a similar vein, it is observed that the performance under Policy 2 dominant interferer approach is a good approximation of the network's coverage performance for both values of R_L, especially in the higher SINR regime. Finally, in Fig. 2.11c, coverage probability versus γ_{th} under Policy 1 and Policy 2 dominant interferer approach for different values of a_N in Policy 1, is illustrated. Clearly, the performance under Policy 2 dominant interferer approach yields a close approximation of the network's coverage performance for both values of a_N, especially as the interference power outside the LOS ball becomes weaker.

Remark 2.30. Note that the received power under Policy 2 would tend to zero for infinitely large LOS ball radius R_L. However, infinite radius is practically impossible to occur in realistic mmWave networks where typical values are smaller than 100 meters [24].

2.7.2 Coverage Performance of BPP 5G NR mmWave Networks

In this section, numerical results of the performance analysis in terms of coverage probability in the special case of a BPP 5G NR mmWave network without misalignment error, as described in subsection 2.6.2, are presented under the three interference scenarios defined in subsection 2.6.2. The CDF of the receiver's antenna gain towards the closest BS in angle ϕ, is also demonstrated to capture the effect of the dominant interference on the performance of the proposed framework. The default system parameters are $f_c = 26.5$GHz, $\alpha_L = 2$,

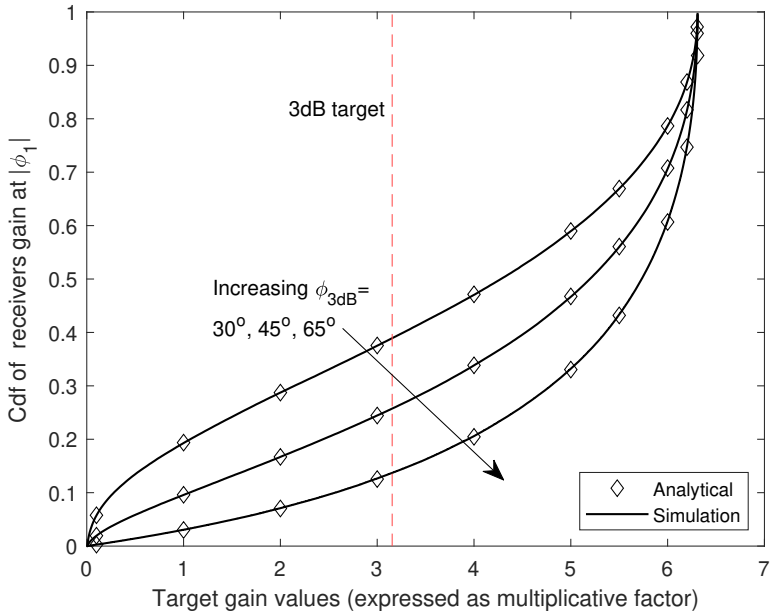

Figure 2.12: The cumulative distribution function (cdf) of the receiver's gain at the closest BS in angular coordinates, for different values of ϕ_{3dB}.

$R_L = 75$ meters as in [24], $N = 10$ and $m_v = 4$ in order to approximate a no fading scenario. As per the 3GPP specifications and in order to be consistent with subsection 2.7.1, $p = 45$ dBm, $\sigma^2 = -74$ dBm and $\phi_{3dB} = 65°$ and $\phi_A = 102.8°$.

Fig. 2.12 compares the CDF of the receiver's antenna gain at an angle that corresponds to the closest interfering BS in angle ϕ, obtained through numerical integration of the PDF derived in Lemma 2.24, for different values of ϕ_{3dB}. The range of the gain values is $[g_s, g_{max}]$. It is observed that as the half power beamwidth, ϕ_{3dB}, of the receiver's antenna increases, the probability that the gain towards the closest BS falls below a target gain value decreases. Indeed, with the increase of ϕ_{3dB} the closest BS is more likely to fall in the mainlobe of the receiver's antenna. Therefore, the receiver antenna gain towards the closest interfering BS in angle ϕ is concentrated to higher values, which in turn, increases the interference. On the other hand, as the directivity of the receiver's antenna increases, the closest interfering BS is less likely to fall within the mainlobe of the receiver's antenna and thus the probability that the gain values are smaller, increases. The red dashed line is used to denote the half power beamwidth region and the corresponding probability that the receiver's gain at ϕ_1 falls within ϕ_{3dB} gain region. Finally, as observed, in all cases the analytical results match the simulations perfectly, which verifies the accuracy of Lemma 2.24.

Fig. 2.13 illustrates the coverage probability, derived in Propositions 2.27-2.29, versus the SINR thresholds γ under the three interference scenarios. A first observation is that the coverage performance in the presence of a dominant interfering BS, underestimates the overall

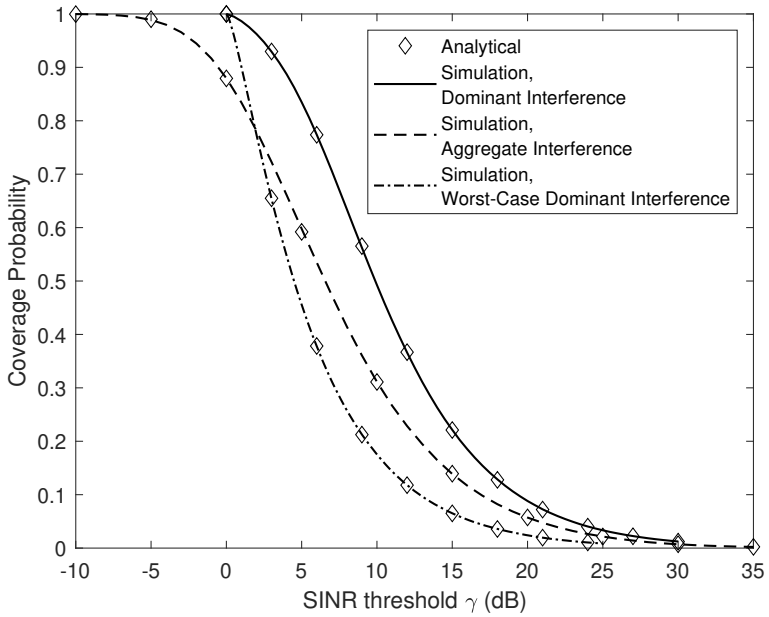

Figure 2.13: Coverage probability versus SINR threshold under the three interference scenarios.

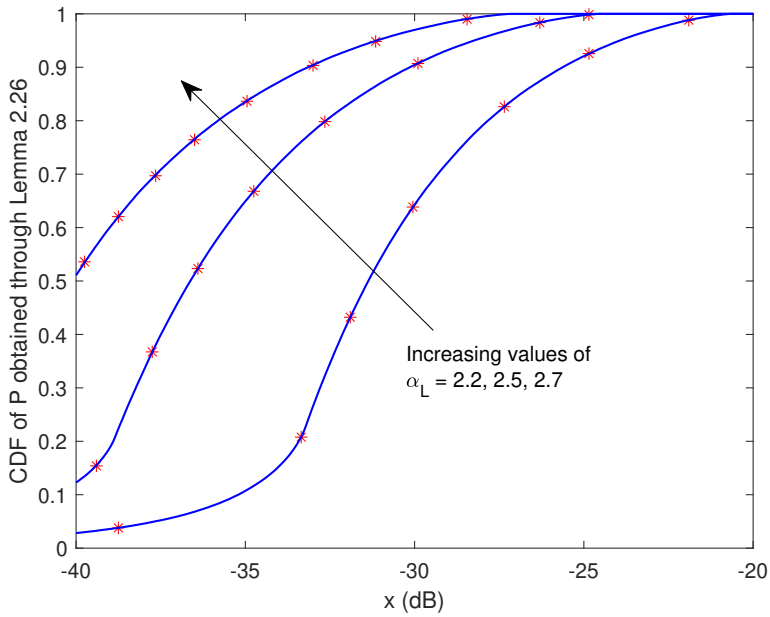

Figure 2.14: CDF of the random variable P obtained by numerical integration of Lemma 2.26 versus abscissa for different values of α_L and $r_1 = 20$ meters.

coverage performance, especially for the smaller values of γ. Indeed, while both the interfering BSs and the dominant interferer can lie anywhere in $b(\mathbf{o}, R_L) \setminus b(\mathbf{o}, ||x_0||)$, the receiver's gain towards the $N-1$ interfering BSs seem to affect the coverage performance considerably, as most BSs fall in the mainlobe of the receiver's antenna. Although the overall coverage performance is more pessimistic than the one under the dominant interferer assumption, the approximation of the dominant interferer is valid. On the other hand, the coverage performance in the presence of the worst-case dominant interference scenario is overestimated. This is because the interfering BS is the closest BS both in Euclidean and in angular distance. In contrast, the $N-1$ interfering BSs can lie anywhere in $b(\mathbf{o}, R_L) \setminus b(\mathbf{o}, ||x_0||)$ and some of them may lie outside the mainlobe of the receiver's antenna. Finally, in all scenarios, the analytical results match the simulations perfectly, which verifies the accuracy of Proposition 2.25, Proposition 2.27 and Proposition 2.29.

Fig. 2.14 illustrates the CDF of the random variable P derived through numerical integration of Lemma 2.26, for different values of α_L. The serving BS is assumed to be located at distance $r_1 = 20$ meters from the receiver. Recalling (2.44), it is easy to observe that the random variable P actually indicates the interference power received from the dominant interferer. A first observation is that the probability that P is below a target value x of the interference power increases as the propagation conditions getting worse. This is more profound for the smaller values of x. Moreover, it is observed that the statistical behavior of the CDF of P becomes different as α_L increases. This is because of the large distance from the receiver that the dominant interferer may lie. Indeed, given that the serving BS is at distance $r_1 = 20$ meters from the receiver, the dominant interferer lies in the annulus $b(\mathbf{o}, R_L) \setminus b(\mathbf{o}, r_1)$ and it is assumed to lie in the mainlobe part of the receiver's antenna. In this case, i) the gain of the receiver's antenna in the definition of P is multiplicative, however ii) even small a degradation in the propagation conditions, severely affect the path-loss. The aforementioned result indicates that the effect of path-loss has a dominant role in the performance of BPP mmWave cellular networks.

2.8 Chapter Summary

In this chapter, we presented an in-depth and unified stochastic geometry framework to study the performance analysis of a 5G NR mmWave cellular network by jointly considering the polar coordinates of the BSs with respect to the typical user. To this end, both the Euclidean and the angular distances of the BSs in a maximum power-based association policy for the UE are considered to account for realistic beam management considerations. For completeness, two other association schemes are considered, which merely accounted for the minimum angular and Euclidean distance association policy. Subsequently, coverage probability analysis was conducted for all policies and exact-form expressions were obtained. Several key intermediate results, such as the Laplace transform of the aggregate interference power distribution, were also derived. Next, the key role of angular distances is highlighted by revisiting

the dominant interferer approach using angular distance-based criteria instead of Euclidean distance-based, and conducting a dominant interferer-based coverage probability analysis. Among others, the numerical results revealed that considering angular distance-based criteria for determining both the serving and the dominant interfering BS, can approximate the coverage performance more accurately as compared to utilizing Euclidean distance-based criteria. Nevertheless, it was shown that a merely angular distance-based association policy is not accurate and therefore considering merely the directional characteristics in the receiver's association policy severely underestimates the coverage performance. In other words, the effect of path-loss cannot be neglected in 5G NR mmWave networks. Finally, a practical case of a BPP mmWave network under the assumption of perfect alignment was studied and three dominant interference scenarios were studied, namely i) a worst-case dominant interferer scenario, ii) a dominant interferer scenario, and iii) the aggregate interference. Numerical results showed that angular distances play a key role in the definition of the dominant interferer in mmWave networks. Indeed, the closest BS in angular distance from the receiver and uniformly distributed in an annulus, has a strong impact on the overall coverage performance and tends to approximate the coverage probability under aggregate interference for the demanding values of SINR. To the best of our understanding, this chapter offered a unified analysis of 5G NR mmWave networks while considering realistic beam management procedures and established meaningful connections between the Euclidean and angular distances. The interested readers are encouraged to extend the proposed framework.

In the next chapter, we extend the analysis beyond the study of terrestrial networks and focus on the modeling and the performance of beyond 5G UAV networks. While our goal is mainly to address conceptual gaps in the modeling of realistic beyond 5G cellular UAV networks, the assumption of the minimum path loss association policy, i.e., the conventional minimum Euclidean distance criterion is adopted in the next chapters.

Chapter 3

Finite Point Processes: Foundations of a Truncated Octahedron-Based 3D UAV Network

3.1 Introduction

As we step towards the 6G vision, UAV-based wireless communications are expected to play a fundamental role to the establishment of the next-generation wireless network infrastructures. Due to their flexibility and inherent ability for LoS communications, UAVs can provide broadband and reliable connectivity during emergency situations and disaster scenarios [49],[50]. Compared to conventional terrestrial BSs, the advantage of using UAVs as aerial BSs is their ability to adjust their altitude and enhance the likelihood of establishing LoS communication. UAVs can also function as aerial UEs, known as cellular-connected UAVs. Under the 6G umbrella, the latter can be used for a wide range of applications such as surveillance, wireless power transfer, sensing and tracking of terrestrial devices or vehicles.

Despite all these attractive opportunities, wireless networking with UAVs still faces a number of challenges. For the UAV-BSs, a key design problem is the 3D deployment as well as the air-to-air/ground channel modeling. A key challenge is to manage the service provision to UAV-UEs in a way to achieve a reliable communication, since the current terrestrial cellular networks have been primarily designed for supporting ground users. Consequently, current cellular networks fail to meet the demanding communication requirements in terms of coverage and capacity for UAV-UEs. A promising solution, is the deployment of UAV-BSs capable of providing reliable connectivity to UAV-UEs [49]. However, given the complicated 3D nature of a UAV network and the dependencies between the spatial locations of UAV-UEs and UAV-BSs, it is not straightforward to statistically characterize the performance of the network at system level. Tackling this challenge, this chapter develops a comprehensive framework with foundations in stochastic geometry to study the performance of a realistic aerial 3D cellular network which was proposed [5] as a candidate beyond 5G 3D cellular architecture. The proposed 3D cellular architecture builds upon the concept of the truncated-octahedron cell shape and integrates both UAV-BSs and UAV-UEs.

3.1.1 Related Work and Motivation

There are a number of works on UAV-based networks focusing on various design and communication challenges that involve 3D deployment and performance analysis. The authors in [51],[52], conducted a coverage and rate analysis assuming that UAVs were deployed in a plane above the ground forming a PPP. In [8], an analysis of a UAV network is performed in terms of the outage probability, where the locations of UAVs are modeled as PPP in a sphere, whereas the authors in [53] conducted a performance analysis in terms of the received rate, by considering aerial mobility models. In [54], [55] the authors exploited Poisson cluster processes to analyze the performance of UAV networks. In [56], the authors examined the performance of a MIMO NOMA assisted UAV network, where the locations of the terrestrial users were modeled as a PPP. However, a PPP does not always adequately model a realistic aerial network since different realizations of the point process consist of different number of aerial nodes. In practice, a finite number of aerial nodes is deployed in UAV networks. For these scenarios, a simple yet proper model for the spatial distribution of a finite number of UAVs is the BPP.

The BPP has received considerable attention in UAV networks. In [57], the BPP was proposed to model a finite UAV network, in which the UAVs were distributed in a disk above the ground and a detailed downlink coverage analysis of terrestrial UEs, was introduced. The authors in [58] performed an analysis of a finite UAV network by considering LoS and NLoS propagation. In [59], a similar analysis was conducted by incorporating trajectory models for the aerial BSs. The authors in [60] exploited the 2D BPP to study the outage probability in a finite UAV network, by considering NOMA mode and correlated UAV channels. In [7], the authors analyzed the performance of a binomial network with nodes placed within a sphere in order to capture the effect of 3D space. In [47], the downlink coverage probability and the rate of an aerial user in vertical heterogeneous networks, was investigated. Finally, the authors in [61] conducted a detailed performance analysis within a UAV-to-ground framework and compared the theoretical results with empirical data.

The majority of existing works propose generic 3D models, where UAV-BSs provide communication links for terrestrial UEs or terrestrial BSs that serve UAV-UEs. In fact, although many of the aforementioned works have utilized the BPP as a realistic point process for the modeling of UAV networks, they do not capture the effect of the 3D space. More specifically, either they deploy the UAVs in a 2D geometrical shapes above the ground, e.g., disc, or they use 3D geometrical shapes, e.g., the sphere, that cannot tessellate the 3D space[1]. In contrast to this, the authors in [5], set for the first time, the foundations of 3D aerial cellular networks by introducing a fundamental cellular architecture for the deployment of UAVs based on the truncated octahedron. The latter is the closest approximation to a sphere, which can tessellate the entire 3D space, and thus it can approximate the spherical radiation pattern of an isotropic antenna. In the proposed cellular architecture, the UAV-BSs are

[1]The 3D tessellation implies that the 3D space is entirely filled with no overlaps or gaps, in a similar way to the hexagonal grid in the 2D cellular networks.

deployed at the center of the truncated octahedrons, forming a 3D lattice. Moreover, the authors in [5], performed network planning and 3D cell association for minimum latency without investigating the performance in the cell. The spatial distribution of the UAV-UEs was only estimated using kernel density estimation. Therefore, the distance distributions in the truncated octahedron and fundamental network metrics such as the coverage probability and the statistical characterization of the SINR have not been investigated. Till now the performance analysis inside a truncated octahedron cell-shape, which is a major beyond 5G candidate 3D cellular architecture, remains an open problem. To overcome the mathematical complexity implied by the adoption of the truncated octahedron cell-shape, the authors in [6] utilized the BPP for the spatial deployment of aerial BSs and the Delaunay tessellation for the 3D cellular network modeling.

Triggered by the aforementioned, in this chapter the finite point process are defined for a truncated octahedron cell-shape for the first time. This also led to the definition of the binomial 3D cellular network, which is formally defined next.

Definition 3.1. A network composed by truncated octahedron cell-shapes and integrates aerial nodes, whose spatial locations are modeled as a 3D BPP, is called a binomial 3D cellular network.

3.1.2 Contributions

The contributions in this chapter are the following:

Binomial 3D cell: Modeling of a truncated octahedron-based 3D cell with finite number of UAVs-UEs

By employing the 3D BPP for modeling the spatial locations of UAVs-UEs, a fixed and finite number of UAVs-UEs is uniformly and independently distributed inside the truncated octahedron. A key contribution of this chapter is the evaluation of the volume of the sub-regions of a truncated octahedron cell-shape in which a UAV-UE may fall. These volumes play a fundamental role in the definition of the BPP and in the coverage probability analysis.

Stochastic geometry analysis in a truncated octahedron

By exploiting fundamental concepts of stochastic geometry theory, distance distributions in a truncated octahedron are statistically characterized. In particular, the n-th nearest node distance distributions are derived in closed-form for a 3D BPP within a truncated octahedron. Intermediate results for the concentration of UAV-UEs in different regions of the truncated octahedron, are also derived. The analysis also extends to the case where the spatial locations

of points are modeled as a finite HPPP. By defining the FHPPP in a truncated octahedron, expressions for the statistical characterization of distance distributions are derived.

3D cellular network coverage probability analysis

Performance analysis in terms of coverage probability under intra-cell interference is conducted. For the sake of completeness, this analysis is also conducted for a finite cell modeled as a sphere, which is a 3D model that retains analytical tractability. As intermediate results in the coverage probability analysis, uniform distance distributions in a truncated octahedron are derived and the Laplace transform of the aggregate interference power, is calculated in exact form.

Multi-cell case coverage probability analysis

Coverage probability analysis is conducted under both intra- and a worst-case inter-cell interference scenario. In particular, further to the interference from the UAV-UEs in the reference cell, a dominant interferer is also assumed to be present from each of the 14 neighboring cells, that is hovering at the center of each of the 14 faces, i.e., at the boundaries of the cell. Note that this is a worst-case scenario due to the minimum distance of the interferers from the reference UAV-BS.

3.2 Mathematical Constructs and Stochastic Geometry Analysis

Consider a 3D cell modeled as a truncated octahedron $W \subset \mathbb{R}^3$ with 14 faces and edge length R. Without loss of generality, it is assumed that W is centered at the origin $\mathbf{o} = (0, 0, 0)$ of the 3D Cartesian coordinate system, and is referred to as the *reference cell* (the black cell shown in Fig. 3.1). The 3D cellular network consists of a predefined arrangement of multiple truncated octahedron cells, as shown in Fig. 3.1. For expositional simplicity, only 4 cells out of 8 neighboring to the hexagonal faces of W and 2 cells out of 6 neighboring to the square faces of W, are depicted. By assuming the first tier of a 3D cellular network, 14 adjacent cells with respect to the reference cell are deployed, and will be referred to as the *neighboring cells*. The coordinates of the centers of the neighboring cells can be directly obtained from [5, Theorem 1]. The UAV-BS located at the center $\mathbf{o}$ of W, is referred to as the reference UAV-BS. It is noted that the deployment of the UAV-BS is not random in practice [47], which justifies such a lattice and makes the network modeling even more realistic. Consider N transmitting UAV-UEs (or simply UAV-UEs for brevity) uniformly and independently distributed in the reference cell. The spatial locations of the UAV-UEs form a BPP Φ. Let R_n denote the random variable representing the Euclidean distance from

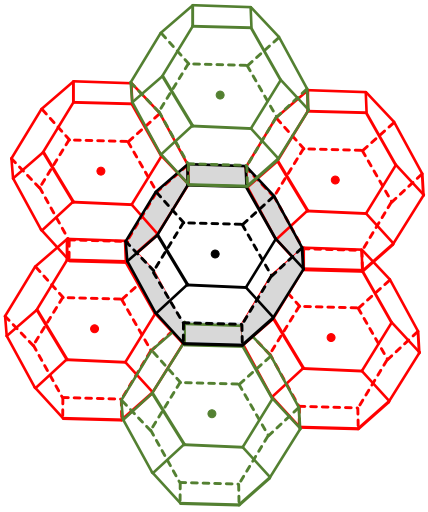

Figure 3.1: Illustration of the system model.

$\mathbf{o}$ to the n-th nearest UAV-UE of Φ, and $b_3(\mathbf{o}, r)$ represents the 3D ball of radius r centered at $\mathbf{o}$.

3.2.1 BPP: Distance Distributions in W

Definition 3.2. Let p denote the probability that a random UAV-UE of the BPP Φ falls in $b_3(\mathbf{o}, r)$. Then, p is given by [46]

$$p = \frac{|b_3(\mathbf{o}, r) \cap W|}{|W|} = \frac{O(\mathbf{o}, r)}{|W|}. \tag{3.1}$$

Accordingly, the following Lemma for obtaining $O(\mathbf{o}, r)$ is given as follows.

Lemma 3.3. *The overlap region $O(\mathbf{o}, r)$ between $b_3(\mathbf{o}, r)$ and W is given by*

$$O(\mathbf{o}, r) = \begin{cases} |b_3(\mathbf{o}, r)| - \mathcal{B}_{(i)}(r), & r < R_c \\ |W|, & r \geqslant R_c \end{cases} \tag{3.2}$$

for $i = 1, ..., 4$.

Proof. See Appendix B.1. □

In a practical 3D wireless cell modeled as a truncated octahedron, the parameter p provides insights about the probability that an arbitrary aerial node falls within the corresponding region of the cell.

Corollary 3.4. *The number of UAV-UEs $\Phi(O(\mathbf{o},r))$ or $\Phi(b_3(\mathbf{o},r))$ lying in $O(\mathbf{o},r)$ or in $b_3(\mathbf{o},r)$, respectively, follows a binomial distribution with parameters $n=N$ and p given by (3.1), i.e., $\Phi(O(\mathbf{o},r)) \sim B(n,p)$.*

Subsequently, the complementary CDF of the distance R_n is the probability that there are less than n UAV-UEs in $O(\mathbf{o},r)$ and it is defined in [46] as

$$\bar{F}_{R_n}(r) \triangleq \sum_{k=0}^{n-1} \binom{N}{k} p^k (1-p)^{n-k} = I_{1-p}(N-n+1,n), \tag{3.3}$$

where $I_x(\cdot,\cdot)$ is the regularized incomplete beta function [40, eq. (8.39)].

Following [46, eq. (3)], the PDF of the distance R_n inside W is formally presented in the following Theorem.

Theorem 3.5. *In a truncated octahedron W centered at $\mathbf{o}$, the PDF of the distance R_n from the origin $\mathbf{o}$ to its n-th nearest UAV-UE is given by*

$$f_{R_n}(r) = \frac{\mathrm{d}p}{\mathrm{d}r} \frac{(1-p)^{N-n}p^{n-1}}{B(N-n+1,n)}, \tag{3.4}$$

for $0 \le r \le R_c$, where $\frac{\mathrm{d}p}{\mathrm{d}r} = \frac{\mathrm{d}O(\mathbf{o},r)}{\mathrm{d}r}/|W|$, and

$$\frac{\mathrm{d}O(\mathbf{o},r)}{\mathrm{d}r} = \begin{cases} \frac{\mathrm{d}O_{(1)}(\mathbf{o},r)}{\mathrm{d}r} & 0 \le r \le R_{hex} \\ \frac{\mathrm{d}O_{(2)}(\mathbf{o},r)}{\mathrm{d}r} & R_{hex} < r \le R_{sq} \\ \frac{\mathrm{d}O_{(3)}(\mathbf{o},r)}{\mathrm{d}r} & R_{sq} < r \le R_{mid} \\ \frac{\mathrm{d}O_{(4)}(\mathbf{o},r)}{\mathrm{d}r} & R_{mid} < r < R_c \\ 0 & r \geqslant R_c \end{cases} \tag{3.5}$$

where $O_{(i)}(\mathbf{o},r) = |b_3(\mathbf{o},r)| - \mathcal{B}_{(i)}(r)$,

$$\begin{aligned} \frac{\mathrm{d}O_{(1)}(\mathbf{o},r)}{\mathrm{d}r} &= 4\pi r^2, \\ \frac{\mathrm{d}O_{(2)}(\mathbf{o},r)}{\mathrm{d}r} &= 4\pi r^2 - 16\pi r(r-R_{hex}), \\ \frac{\mathrm{d}O_{(3)}(\mathbf{o},r)}{\mathrm{d}r} &= \frac{\mathrm{d}O_{(2)}(\mathbf{o},r)}{\mathrm{d}r} - 12\pi r(r-R_{sq}), \end{aligned} \tag{3.6}$$

and $\frac{\mathrm{d}O_{(4)}(\mathbf{o},r)}{\mathrm{d}r}$ *is given by*

$$\frac{\mathrm{d}O_{(4)}(\mathbf{o},r)}{\mathrm{d}r} = \frac{\mathrm{d}O_{(3)}(\mathbf{o},r)}{\mathrm{d}r} + \frac{8a_{max}^{hex}\left(r^3 - R_{mid}^3\right)C(r)}{3\left(r^2 - R_{hex}^2\right)\sqrt{r^2 - R_{mid}^2}} + 8rC(r)\arccos\left(\frac{a_{max}^{hex}}{\sqrt{r^2 - R_{hex}^2}}\right)$$
$$+ \frac{8\left(r^3 - R_{mid}^3\right)\left(-\frac{12(a_{max}^{hex})^2}{\sqrt{r^2-(a_{max}^{hex})^2}} + \frac{4\sqrt{3}(a_{max}^{sq})^2}{\sqrt{r^2-(a_{max}^{sq})^2}} + \frac{2\sqrt{6}R_{sq}^2}{\sqrt{r^2-R_{sq}^2}} - \sqrt{6}R\right)}{3r^2}\arccos\left(\frac{a_{max}^{hex}}{\sqrt{r^2 - R_{hex}^2}}\right), \tag{3.7}$$

where $B(\cdot,\cdot)$ *denotes the Beta function [40, eq. (8.380.1)], and* $C(r)$ *is given by*

$$C(r) = 4\sqrt{3}\sqrt{r^2 - (a_{max}^{sq})^2} - 12\sqrt{r^2 - (a_{max}^{hex})^2} + \sqrt{6}R + 2\sqrt{6}\sqrt{r^2 - R_{sq}^2}. \tag{3.8}$$

Proof. See Appendix B.2. □

The void probability p_b^0 of the BPP Φ is defined as the probability of there being no UAV-UE of Φ in a region $O(\mathbf{o},r)$ of W and consequently

$$p_b^0 = (1-p)^N. \tag{3.9}$$

Of great interest are the nearest and farthest node distances in W, which are usually taken as the serving distance and the distance of a cell-edge user in UAV-enabled communication scenarios. The nearest node distance PDF in W is given by

$$f_{R_1}(r) = N\frac{\mathrm{d}p}{\mathrm{d}r}(1-p)^{N-1}, \tag{3.10}$$

and the distance PDF to the farthest UAV-UE from the origin $\mathbf{o}$ in W is given by

$$f_{R_N}(r) = N\frac{\mathrm{d}p}{\mathrm{d}r}p^{N-1}. \tag{3.11}$$

3.2.2 PPP: Distance Distributions in W

In the following the analysis is extended to the case of a PPP. The finite HPPP in a truncated octahedron W is formally defined.

Definition 3.6. Let Ω be a HPPP of intensity λ over the entire $\mathbb{R}^3$. Define the finite HPPP inside W as $\Psi = \Omega \cap W$.

The only distinction between Φ and Ψ in W, is that different realizations of Ψ constitute of a different number of UAV-UEs. The finite HPPP Ψ is suitable for modeling a random

number of nodes within the finite truncated octahedron W. The probability that there are k UAV-UEs inside a region $O(\mathbf{o}, r)$ of W is distributed according to the Poisson distribution

$$P_k(\mathbf{o}, r) = \mathbb{P}(\Psi(O(\mathbf{o}, r)) = k) = e^{-\lambda O(\mathbf{o},r)} T_k, \tag{3.12}$$

where $T_k = \frac{(\lambda O(\mathbf{o},r))^k}{k!}$, and the probability that there are k UAV-UEs inside the complementary region of $O(\mathbf{o}, r)$, $W \setminus O(\mathbf{o}, r)$, is given by

$$Q_k(\mathbf{o}, r) = \mathbb{P}(\Psi(W \setminus O(\mathbf{o}, r)) = k) = e^{-\lambda(|W| - O(\mathbf{o},r))} \frac{(\lambda(|W| - O(\mathbf{o}, r)))^k}{k!}. \tag{3.13}$$

Notice that the number of UAV-UEs falling into the disjoint regions of W, $O(\mathbf{o}, r)$ and $W \setminus O(\mathbf{o}, r)$, is independent. In the finite HPPP Ψ, the void probability with respect to a test set $O(\mathbf{o}, r)$ is given by

$$u_b^0 = \mathbb{P}(\Psi(O(\mathbf{o}, r)) = 0) = P_0(\mathbf{o}, r) = e^{-\lambda O(\mathbf{o},r)}. \tag{3.14}$$

The PDF of R_n for a finite HPPP Ψ along with the corresponding CDF are presented in the following Corollary.

Corollary 3.7. *In an finite HPPP Ψ inside W, the PDF of the distance R_n between the origin $\mathbf{o}$ and its n-th nearest UAV-UE, and the corresponding CDF, are given by*

$$f_{R_n}(r) = \lambda^n \frac{\mathrm{d}(O(\mathbf{o}, r)^n)}{\mathrm{dr}} \frac{e^{-\lambda O(\mathbf{o},r)}}{n\Gamma(n)}, \tag{3.15}$$

$$F_{R_n}(r) = 1 - \sum_{k=0}^{n-1} e^{-\lambda O(\mathbf{o},r)} T_k, \tag{3.16}$$

for $0 \leq r \leq R_c$.

Proof. See Appendix B.3. □

Notice that Corollary 3.7 depends only on the overlapping area between $b_3(\mathbf{o}, r)$ and W. Consequently, the previous results can be generalized for an arbitrary region V as follows.

Corollary 3.8. *Consider the finite HPPP of density λ over an arbitrary compact set $V \subset \mathbb{R}^3$ centered at the origin $\mathbf{o}$. If the region, $L(\mathbf{o}, r) = |b_3(\mathbf{o}, r) \cap V|$ can be evaluated, for every radius r, then the PDF of R_n inside V along with the corresponding CDF are given directly after substituting $O(\mathbf{o}, r)$ in Corollary 3.7, with $L(\mathbf{o}, r)$.*

Remark 3.9. For the special case where $V = b_3(\mathbf{o}, D)$, (3.15) reduces to [46, eq. (11)], i.e.,

$$f_{R_n}(r) = e^{-\frac{4\pi\lambda}{3} r^3} \frac{(4\pi\lambda r^3)^n}{n\Gamma(n)}, \quad r \in [0, D]. \tag{3.17}$$

Remark 3.10. A practical case is met when V is a 3D cell modeled as a cube, which can tessellate the entire $\mathbb{R}^3$, too [5]. Although it is not a close approximation of a sphere when compared to the truncated octahedron, it is geometrically tractable. In this case, $L(\mathbf{o}, r)$ is evaluated similar to $O(\mathbf{o}, r)$.

3.3 Coverage Probability Analysis

In this section, performance analysis in terms of coverage probability is conducted for the reference UAV-BS. In particular, the coverage performance is investigated under two interference cases: i) intra-cell interference: the reference UAV-BS experiences interference only from the UAV-UEs in W, and ii) intra- and inter-cell interference, i.e., the reference UAV-BS experiences additional interference from UAV-UEs in the neighboring cells under a worst-case scenario. For this case, a UAV-UE from each of the 14 neighboring cells of the network is supposed to hover at the center of each of the 14 faces (i.e., the boundaries) of W interfering at the reference UAV-BS. For the sake of completeness, the coverage probability analysis under intra-cell interference in W is also conducted for an aerial 3D cell, where the user locations are modeled as a 3D BPP in a sphere.

3.3.1 Communication, Channel Models and SINR Definitions

Assume a finite 3D cell, where the UAV-UEs are modeled as a 3D BPP in $b_3(\mathbf{o}, R_c)$. Then, the unordered set of distances from the reference UAV-BS to the UAV-UEs are denoted by $\{U_i\}$, $\{D_i\}$, for W and $b_3(\mathbf{o}, R_c)$, respectively, and indicate that the index i is arbitrarily assigned to the UAV-UEs. The ordered set of the distance between the reference UAV-BS and the nth nearest UAV-UE, is denoted by $\{R_n\}_{n=1:N}$ for both W and $b_3(\mathbf{o}, R_c)$. Assume that the reference UAV-BS communicates with the nth nearest node out of the N UAV-UEs. The work in this section focuses on the reverse link and therefore, the nth nearest UAV-UE is referred to as the *serving* UAV-UE and the reverse link as the *serving link*. The distance of the serving UAV-UE to the reference UAV-BS is denoted by $R_S = R_n$ and is referred to as the *serving distance*. An ALOHA-like MAC protocol is assumed for the communications inside the cell. Once the serving link has been established, the remaining $N-1$ UAV-UEs in W and in $b_3(\mathbf{o}, R_c)$ interfere to the reference UAV-BS. In order to capture the effect of a worst-case inter-cell interference scenario on coverage performance in W, a UAV-UE from each of the 14 neighboring cells is supposed to hover at the center of each of the 14 faces of W. The communication links among the interfering UAV-UEs and the reference UAV-BS are referred to as the *interfering links*.

Assume that the UAV-UEs transmit at the same power (30 dBm). The channels undergo Nakagami-m fading, which is a generalized model for various fading environments and simultaneously retains analytical tractability [57]. The amplitude of the received signal power

follows Nakagami-m distribution, while the channel fading gain $h \in \{h_S, h_i\}$, for the serving and interfering links, follows the Gamma distribution with fading parameter $m \in \{m_S, m_I\}$, respectively. The shape and scale parameters of h are m and $1/m$, respectively, i.e., $h \sim$ Gamma $\left(m, \frac{1}{m}\right)$ with PDF given by

$$f_h(x) = \frac{m^m x^{m-1}}{\Gamma(m)} \exp(-mx). \tag{3.18}$$

Note that $\mathbb{E}[h^2] = 1$. Also, the values of m_S are restricted to integers for analytical tractability.

In practice, the location of the serving UAV-UEs is usually investigated in order to cope with limitations such as the flight time and the on-board energy [62], [63]. In the following scenario, it is assumed to be fixed and henceforth $R_S = R_n = r_s$. However, the same analysis can be also applied to the case where R_S is a RV. The SINR at the reference UAV-BS is

$$SINR_{oct} = \frac{h_S r_s^{-\alpha}}{I_{oct} + \sigma^2}, \tag{3.19}$$

and the SINR at the reference UAV-BS in $b_3(\mathbf{o}, R_c)$ is

$$SINR_{sph} = \frac{h_S r_s^{-\alpha}}{I_{sph} + \sigma^2}, \tag{3.20}$$

where σ^2 is the additive white Gaussian noise power and I_{oct}, I_{sph} refers to the interference power in W and $b_3(\mathbf{o}, R_c)$, respectively. By considering the serving distance r_s, then $n-1$ nodes lie within the *near zone* $O(\mathbf{o}, r_s)$ and $b_3(\mathbf{o}, r_s)$ of the reference UAV-BS for W and $b_3(\mathbf{o}, R_c)$, respectively, while the farther nodes lie within the *far zone* $W \setminus O(\mathbf{o}, r_s)$ and $b_3(\mathbf{o}, R_c) \setminus b_3(\mathbf{o}, r_s)$ of the reference UAV-BS. for W and $b_3(\mathbf{o}, R_c)$ respectively, and interfere to the reference UAV-BS. Consequently, I_{oct}, I_{sph} can be expressed as $I_{oct} = I_{oct}^{near} + I_{oct}^{far}$ and $I_{sph} = I_{sph}^{near} + I_{sph}^{far}$, respectively, where

$$\begin{aligned} I_{oct}^{near} &= \sum_{i=1}^{n-1} h_i (U_i^{near}|r_s)^{-\alpha}, I_{oct}^{far} = \sum_{i=1}^{N-n} h_i (U_i^{far}|r_s)^{-\alpha}, \\ I_{sph}^{near} &= \sum_{i=1}^{n-1} h_i (D_i^{near}|r_s)^{-\alpha}, I_{sph}^{far} = \sum_{i=1}^{N-n} h_i (D_i^{far}|r_s)^{-\alpha}, \end{aligned} \tag{3.21}$$

where $U_i^{near}|r_s$, $D_i^{near}|r_s$, $U_i^{far}|r_s$, and $D_i^{far}|r_s$ denote the conditional distances between the reference UAV-BS and the interferers of the near and the far zone respectively, given the serving distance r_s in W and $b_3(\mathbf{o}, R_c)$. The parameter α is the path-loss exponent.

If the aggregate interference i.e., both intra- and inter-cell interference is considered, the reference UAV-BS experiences additional interference from 8 UAV-UEs hovering at the center

of the 8 hexagonal faces of W and from 6 UAV-UEs hovering at the center of the 6 square faces of W. Then, the SINR at the reference UAV-BS is given by

$$SINR_{oct,agg} = \frac{h_S r_s^{-\alpha}}{I_{oct} + I_{inter} + \sigma^2}, \tag{3.22}$$

where I_{inter} is given by

$$I_{inter} = \sum_{i=1}^{8} h_i R_{hex}^{-\alpha} + \sum_{i=1}^{6} h_i R_{sq}^{-\alpha}, \tag{3.23}$$

where R_{hex}, R_{sq} have been defined in Appendix B.1.

3.3.2 Relevant Distance Distributions

In this subsection the distance distributions between the reference UAV-BS and the UAVs inside W and $b_3(\mathbf{o}, R_c)$ are statistically characterized. This is a key intermediate step in the coverage probability analysis. The set of distances $\{U_i\}$ from the reference UAV-BS to the UAVs in W are i.i.d. with the following

$$f_{U_i}(u_i) = \frac{\mathrm{d}O(\mathbf{o}, u_i)}{\mathrm{d}u_i} / |W|, \quad 0 \le u_i \le R_c \tag{3.24}$$

The corresponding CDF is given by

$$F_{U_i}(u_i) = \frac{O(\mathbf{o}, u_i)}{|W|}. \tag{3.25}$$

The above expressions lead to the following Lemmas for the distributions of $U_i^{near}|r_s$, $U_i^{far}|r_s$.

Lemma 3.11. *Conditioned on the serving distance r_s, the distances $\{U_i^{near}|r_s\}_{i=1:n-1}$ between the reference UAV-BS and the interferers of the near zone $O(\mathbf{o}, r_s)$, are i.i.d. with the following PDF*

$$f_{U_i^{near}|r_s}(u_i) = \frac{\mathrm{d}O(\mathbf{o}, u_i)}{\mathrm{d}u_i} / O(\mathbf{o}, r_s), \quad 0 \le u_i \le r_s. \tag{3.26}$$

The corresponding CDF is given by

$$F_{U_i^{near}|r_s}(u_i) = \frac{O(\mathbf{o}, u_i)}{O(\mathbf{o}, r_s)}, \quad 0 \le u_i \le r_s. \tag{3.27}$$

Proof: The procedure for deriving (3.26) is the same as in [6, App. A] and hence it is omitted here. The corresponding CDF is obtained through integration with respect to the range of u_i and this completes the proof. □

For the sphere, conditioned on the serving distance r_s, the distances $\{D_i^{near}|r_s\}_{i=1:n-1}$ be-

tween the reference UAV-BS and the interferers of the near zone $b_3(\mathbf{o}, r_s)$ in $b_3(\mathbf{o}, R_c)$, are i.i.d., with PDF given by

$$f_{D_i^{near}|r_s}(d_i) = \frac{3d_i^2}{r_s^3}, \quad 0 \leq d_i \leq r_s. \tag{3.28}$$

Similarly, conditioned on the serving distance r_s, the distances $\{D_i^{far}|r_s\}_{i=1:N-n}$ between the reference UAV-BS and the interferers in the far zone $b_3(\mathbf{o}, R_c) \setminus b_3(\mathbf{o}, r_s)$, are i.i.d. with a PDF given by

$$f_{D_i^{far}|r_s}(d_i) = \frac{3d_i^2}{R_c^3 - r_s^3}, \quad r_s \leq d_i \leq R_c. \tag{3.29}$$

3.3.3 Coverage Probability Analysis

In this subsection, exact form expressions for the coverage probability at the reference UAV-BS, are derived under the two interference cases.

Intra-Cell Interference Case

Under the intra-cell interference case, exact and closed-form expressions for the coverage probability inside W and $b_3(\mathbf{o}, R_c)$, respectively, are extracted. Given the serving distance r_s, the conditional Laplace transform of the interference power distribution is first derived in exact form for W, and in closed form for $b_3(\mathbf{o}, R_c)$.

Lemma 3.12. *The Laplace transform of the intra-cell interference power distribution I_{oct}, I_{sph} conditioned on the serving distance r_s is given by*

$$\begin{aligned}&\mathcal{L}_{I_{oct}}(s|r_s)\\ &= \left[\int_0^{r_s} \left(1 + \frac{su_i^{-\alpha}}{m_I}\right)^{-m_I} f_{U_i^{near}|r_s}(u_i)\,\mathrm{d}u_i\right]^{n-1} \left[\int_{r_s}^{R_c} \left(1 + \frac{su_i^{-\alpha}}{m_I}\right)^{-m_I} f_{U_i^{far}|r_s}(u_i)\,\mathrm{d}u_i\right]^{N-n},\end{aligned} \tag{3.30}$$

and

$$\begin{aligned}&\mathcal{L}_{I_{sph}}(s|r_s)\\ &= \left[\int_0^{r_s} \left(1 + \frac{sd_i^{-\alpha}}{m_I}\right)^{-m_I} f_{D_i^{near}|r_s}(d_i)\,\mathrm{d}d_i\right]^{n-1} \left[\int_{r_s}^{R_c} \left(1 + \frac{sd_i^{-\alpha}}{m_I}\right)^{-m_I} f_{D_i^{far}|r_s}(d_i)\,\mathrm{d}d_i\right]^{N-n}\\ &= \left[\frac{3\,{}_2F_1\left(m_I, m_I + \frac{3}{a}; 1 + m_I + \frac{3}{a}; -\frac{{r_s}^a m_I}{s}\right)}{{r_s}^{3-am_I}\left(\frac{m_I}{s}\right)^{-m_I}(am_I + 3)}\right]^{n-1} \left[\frac{\Theta(s, R_c) - \Theta(s, r_s)}{R_c^3 - r_s^3}\right]^{N-n},\end{aligned} \tag{3.31}$$

respectively, where $\Theta(s,x) = x^3\,{}_2F_1\left(-\frac{3}{a}, m_I; \frac{a-3}{a}; -\frac{x^{-a}s}{m_I}\right)$ *with* ${}_2F_1(\cdot)$ *denoting the Gauss hypergeometric function given in [40, eq. (9.34.8)].*

Proof. See Appendix B.4. □

Remark 3.13. Lemma 3.12 captures the interference caused by both the dominant and the distant interfering UAV-UEs separately. Consequently, one can compare the interference experienced in the near and far zone of a cell modeled as a truncated octahedron and a cell modeled as a sphere.

The coverage probability is defined as the probability that the $SINR$ at the reference UAV-BS inside W and $b_3(\mathbf{o}, R_c)$ exceeds a predefined threshold γ, i.e.,

$$\begin{aligned} \mathcal{P}_c^{oct} &\triangleq \mathbb{P}(SINR_{oct} \geqslant \gamma), \\ \mathcal{P}_c^{sph} &\triangleq \mathbb{P}(SINR_{sph} \geqslant \gamma), \end{aligned} \tag{3.32}$$

respectively. The coverage probability is now obtained in exact form for W, and in closed form for $b_3(\mathbf{o}, R_c)$, in the following Theorem.

Theorem 3.14. *The coverage probability at the reference UAV-BS in* W *and* $b_3(\mathbf{o}, R_c)$ *under the intra-cell interference case and conditioned on the serving distance* r_s*, in the presence of Nakagami-m fading is given by*

$$\mathcal{P}_c^{oct} = \sum_{k=0}^{m_S-1} \frac{(-m_S\gamma r_s^a)^k}{k!} \left[\frac{\partial^k \mathcal{L}_{I_{intra}}^{oct}(s|r_s)}{\partial s^k}\right]_{s=m_S\gamma r_s^a}, \tag{3.33}$$

and

$$\mathcal{P}_c^{sph} = \sum_{k=0}^{m_S-1} \frac{(-m_S\gamma r_s^a)^k}{k!} \left[\frac{\partial^k \mathcal{L}_{I_{tot}}^{sph}(s|r_s)}{\partial s^k}\right]_{s=m_S\gamma r_s^a}, \tag{3.34}$$

respectively, where $\mathcal{L}_{I_{intra}}^{oct}(s|r_s) = \exp(-\sigma^2 s)\mathcal{L}_{I_{oct}}(s|r_s)$ *and* $\mathcal{L}_{I_{tot}}^{sph}(s|r_s) = \exp(-\sigma^2 s)\mathcal{L}_{I_{sph}}(s|r_s)$.

Proof: Following the same lines as in [47, App. F], (3.33) is derived. Moreover, using (3.31), (3.34) results to a closed form expression and this completes the proof. □

Remark 3.15. The expression derived in Theorem 3.14 considers the different locations of the serving UAV – UE. For the truncated octahedron cell, the volume of the geometrical regions in which the interfering UAV–UEs lie varies significantly. This affects the resulting interference and the coverage probability.

Intra- and Inter-Cell Interference Case

Under both intra-cell and the worst case inter-cell interference scenario, exact-form expression for the coverage probability, is derived. The Laplace transform of the inter-cell inter-

ference power distribution is first calculated as intermediate step in the coverage probability analysis.

Lemma 3.16. *The Laplace transform of the inter-cell interference power distribution I_{inter} is given by*

$$\mathcal{L}_{I_{inter}}(s) = \left(1 + \frac{sR_{hex}^{-\alpha}}{m_I}\right)^{-8m_I} \left(1 + \frac{sR_{sq}^{-\alpha}}{m_I}\right)^{-6m_I}. \tag{3.35}$$

Proof: The proof of the Laplace transform of the inter-cell interference follows the same lines as the proof in Lemma 3.12, and hence it is omitted here. □

The coverage probability is defined as the probability that the $SINR_{oct,agg}$ at the reference UAV-BS exceeds a predefined threshold γ, i.e.,

$$\mathcal{P}_{c,agg}^{oct} \triangleq \mathbb{P}(SINR_{oct,agg} \geqslant \gamma). \tag{3.36}$$

The coverage probability may now be obtained as in the following Theorem.

Theorem 3.17. *The coverage probability under an intra- and inter-cell interference case, and conditioned on the serving distance r_s, in the presence of Nakagami-m fading is given by*

$$\mathcal{P}_{c,agg}^{oct} = \sum_{k=0}^{m_S-1} \frac{(-m_S\gamma r_s^a)^k}{k!} \left[\frac{\partial^k \mathcal{L}_{I_{agg}}^{oct}(s|r_s)}{\partial s^k}\right]_{s=m_S\gamma r_s^a}, \tag{3.37}$$

where $\mathcal{L}_{I_{agg}}^{oct}(s|r_s) = \mathcal{L}_{I_{intra}}^{oct}(s|r_s)\mathcal{L}_{I_{inter}}(s)$.

Proof: The proof for deriving (3.37) follows the same lines as in [47, App. F], and hence it is omitted here. □

3.4 Numerical Results and Discussions

In this section, numerical results are presented to evaluate i) the proposed stochastic geometry analysis of the finite point processes in a truncated octahedron cell-shape, ii) the coverage performance achieved in a truncated octahedron cell-shape, and iii) the coverage performance of a multi-cell 3D network under both intra- and a worst- case inter-cell interference scenario. The accuracy of the analytical results presented in this chapter is verified by comparing them with the empirical results obtained from Monte-Carlo simulations.

3.4.1 Stochastic Geometry Analysis in a Truncated Octahedron

Fig. 3.2, depicts the probability that exactly n UAV-UEs fall inside different regions $O(\mathbf{o}, r)$. The theoretical curves were evaluated using (3.3), for different values of the radius r, whereas

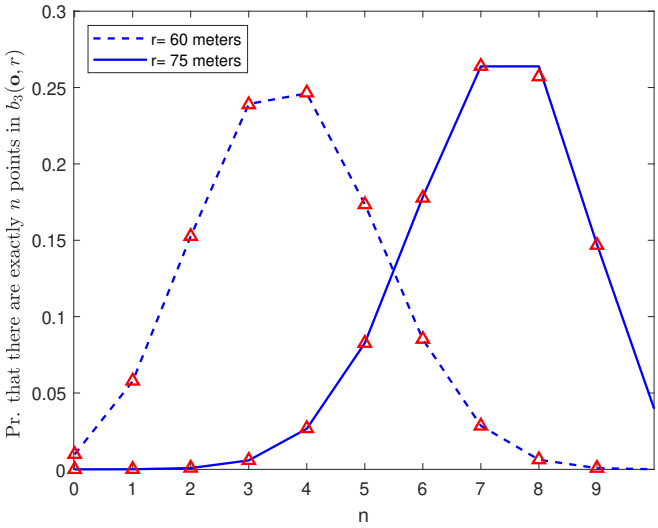

Figure 3.2: Probability of having n UAV-UEs in $O(\mathbf{o}, r)$ with $R_c \approx 95$ meters and $N = 10$. Markers denote simulation points.

for the simulation results a 3D BPP in W was deployed using the simulation procedure given in Appendix B.5. In all the following numerical results, the edge length R of W is assumed $R = 60$ meters and consequently $R_c \approx 95$ meters, $R_{hex} \approx 73$ meters, $R_{sq} \approx 85$ meters and $R_{mid} = 90$ meters, whereas $N = 10$. For $r = 60$ meters, $b_3(\mathbf{o}, r)$ is enclosed within W, while for $r = 75$ meters, $b_3(\mathbf{o}, r)$ lies outside W. As one can easily observe, the probability that there are exactly n UAV-UEs in $O(\mathbf{o}, r)$ admits a trapezoidal form. This means that for different values of r, the probability is maximized and becomes stabilized for some specific values of n. For example, for $r = 60$ meters there is approximately 50% probability that there are 3 or 4 nodes in $O(\mathbf{o}, r)$.

Fig. 3.3 compares $\bar{F}_{R_n}(r)$, for a truncated octahedron and a sphere of radius $R_{sph} = R_c$, for different values of r. A first observation is that for $r = 60$ meters and $r = 75$ meters, the probabilities that there are less than n UAV-UEs inside $O(\mathbf{o}, r)$ are noticeably smaller than the ones inside a sphere. In fact, as r increases, the difference between these probabilities becomes significantly larger. This is due to the fact that as r increases, the geometry of $O(\mathbf{o}, r)$ starts to significantly differentiate from the geometry of the corresponding sphere. For a 3D cell, this fact indicates that more aerial nodes is likely to fall within the regions of the truncated octahedron than in the sphere. A second observation is that, $\bar{F}_{R_n}(r)$ for $b_3(\mathbf{o}, 85)$ coincides with the $\bar{F}_{R_n}(r)$ of $O(\mathbf{o}, 75)$. The same applies to $b_3(\mathbf{o}, 93)$ and $O(\mathbf{o}, 85)$. In practice, this means that although the volume of the two cell-shapes is different, p is approximately the same.

Fig. 3.4 illustrates again the $\bar{F}_{R_n}(r)$ but in contrast to Fig. 3.3, the volume of the two cell-shapes is assumed to be equal. In particular, $R \approx 64.6$ meters and $R_{sph} = 90$ meters.

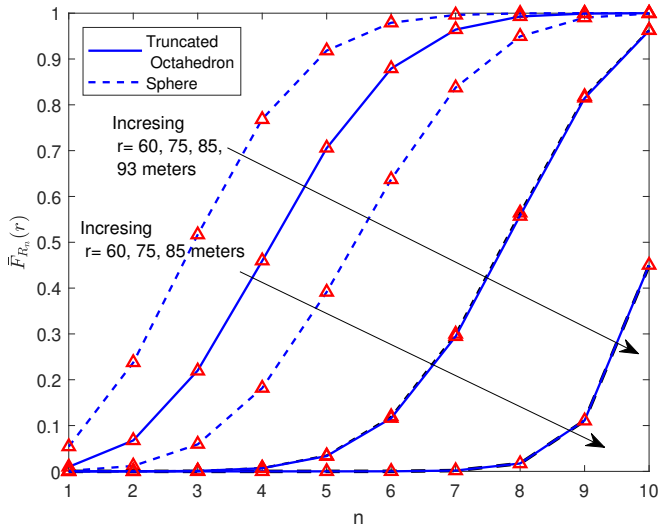

Figure 3.3: Probability of having less than n UAV-UEs in the region $O(\mathbf{o}, r)$ of W and a sphere of radius $R_c = 95$ meters and $N = 10$. Markers denote simulation UAV-UEs.

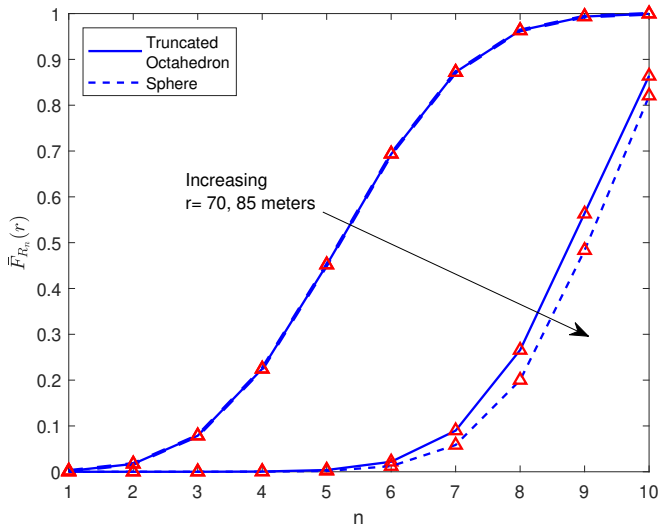

Figure 3.4: Probability of having less than n UAV-UEs in the region $O(\mathbf{o}, r)$ of W and a sphere of the same volume for $R_{sph} = 90$ meters, $N = 10$ and $R \approx 64.6$ meters. Markers denote simulation points.

Also, $R_{hex} \approx 79$ meters, while $R_c \approx 102$ meters. In this case, the probability p in (3.1) is dominated only by $O(\mathbf{o}, r)$ for both the sphere and the truncated octahedron, i.e., for $r = 70$ meters, $O(\mathbf{o}, 70) = b_3(\mathbf{o}, 70)$ and consequently $\bar{F}_{R_n}(r)$ is the same, as expected. As r increases, the difference in curves between the region $O(\mathbf{o}, r)$ and the sphere increases as

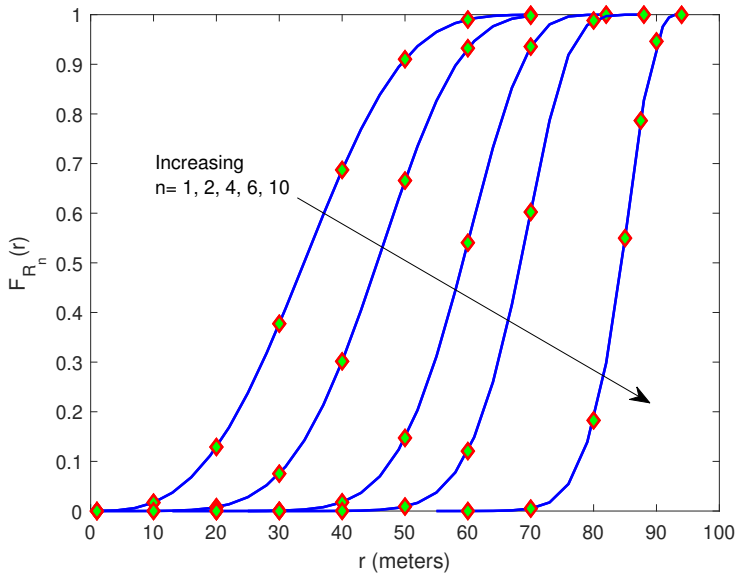

Figure 3.5: CDF of the distance R_n derived in Theorem 1 for $R_c \approx 95$ meters, $N = 10$. Markers denote simulation points.

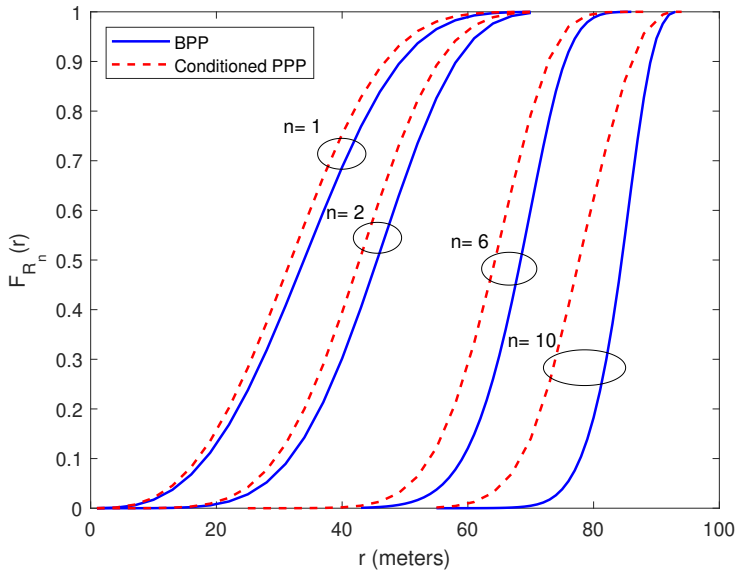

Figure 3.6: Comparison of the CDF of R_n for a conditioned PPP versus a BPP of the same density $\lambda = N/|W|$, $N = 10$ and $R_c = 95$ meters.

well, which in turn affects the aforementioned probabilities. In general, notice that up to $r = R_{hex}$, $O(\mathbf{o}, r) = b_3(\mathbf{o}, r)$.

Fig. 3.5 illustrates the CDF of R_n in a truncated octahedron, through applying numerical integration of Theorem 3.5. The CDF is plotted as a function of the distance r for different values of n. As n increases, the slope of the curves increases as well. Fig. 3.5 also illustrates the regions of the truncated octahedron, in which each UAV-UE may lie in, according to the range of r. Notice that for all values of n, the theoretical results match the simulations perfectly.

Fig. 3.6 compares the CDF of the distance R_n, obtained through numerical integration of Theorem 3.5, with the CDF for a conditioned PPP of the same density, derived in Corollary 3.7, for different values of n. It is easy to notice that the CDFs for a conditioned PPP does not accurately approach the CDFs for a BPP. In fact, as n increases, i.e., for farther neighbors, the difference between the conditioned PPP and the BPP increases as well. This is because of the different nature of the two point processes. For example, by assuming that the first nearest UAV-UE lies within a distance s from the center of the truncated octahedron, then necessarily the $N-1$ UAV-UEs lie in the remaining region. In the conditioned PPP, by contrast, this statement does not hold as the total number of UAV-UEs lying within the truncated octahedron is random.

3.4.2 Coverage Probability analysis

Fig. 3.7 compares the coverage probability, derived in Theorem 3.14, versus the SINR threshold for a cell modeled as a truncated octahedron and a cell modeled as a sphere. For both models, the serving distance $r_s = 40$ meters. The coverage probability is illustrated for different values of the path-loss factor α and shaping parameter m. A first observation is that the sphere geometry, although it is undoubtedly a mathematically tractable model, provides more optimistic results compared to a 3D cellular network modeled by a truncated octahedron. The second observation is that as the propagation conditions move to more favorable from $\alpha = 4$ to $\alpha = 2.5$, the aggregate interference power experienced at the reference UAV-BS is increased and thus the overall coverage probability is degraded. In Fig. Fig. 3.7, the coverage probability is also demonstrated for different values of the Nakagami fading parameter m. Once again, the coverage is better in a network where the UAVs-UEs are deployed within a sphere than in a network where the deployment space is a truncated octahedron for both values of m. As the fading conditions move from Rayleigh ($m = 1$) to more favorable conditions ($m = 4$), the coverage is significantly improved for both models. An interesting result is observed for the more demanding values of the SINR threshold. For both values of m, there is a crossing-point after which the coverage probability is inverted, i.e., the coverage is better for poor fading conditions. Indeed, for higher values of SINR threshold, the serving UAV node is favored under poor fading conditions, since it is the closest node to the reference UAV-BS. The aggregate interference power in poor fading conditions, by contrast, is degraded since the interfering UAVs-UEs are far from the reference UAV-BS and they are severely affected by the bad channel conditions. Notice that in all cases, Theorem 3.14 match the simulations perfectly, which validates the accuracy of the proposed coverage

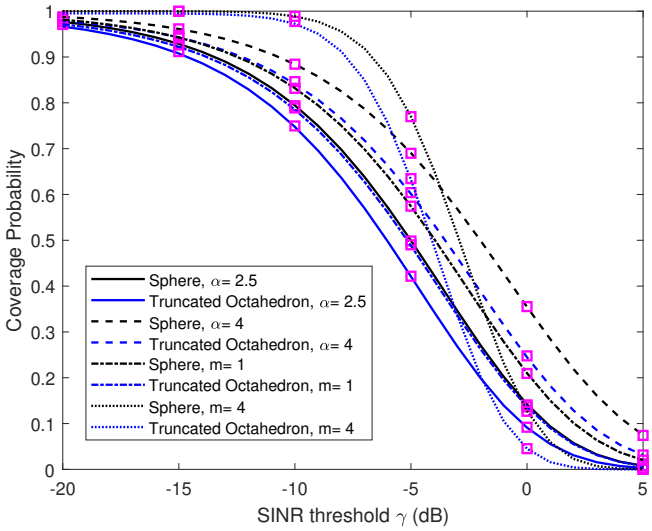

Figure 3.7: Coverage probability versus SINR threshold for different parameters and $N = 10$, $R_c = 95$ meters, and $R_S = R_1$. The curves corresponding to different values of m are derived assuming $a = 3$. Squares denote simulation points.

probability analysis.

Fig. 3.8 compares the coverage probability versus SINR threshold for both cell models under the same fading and propagation conditions $m = 4$, $\alpha = 3$, respectively, when different serving nodes are selected. For both models, $N = 10$, and $R_c = 95$ meters. When the 5-th nearest node is selected as the serving node with serving distance $r_s = 65$ meters, then 4 UAV-UEs lie within the near regions $O(\mathbf{o}, 65)$ and $b_3(\mathbf{o}, 65)$ of the reference UAV-BSs, for the truncated octahedron and the sphere, respectively, and cause severe interference to the UAV-BS. The remaining 5 UAV-UEs lie within the far region of the reference UAV-BSs and interfere less severely. As one can easily observe, the performance in terms of coverage probability is almost identical for both models. This is because the 4 interfering UAV-UEs, which interfere significantly to the reference UAV-BSs, lie within the same near region, i.e., a sphere, both for the truncated octahedron and the sphere. The impact of the interference to the coverage probability from UAV-UEs that lie within different far regions in the two models, is negligible.

The worst case performance scenario under intra-cell interference only is considered when the serving node is chosen at the cell-edge at serving distance $r_s = 88$ meters. Indeed, as seen from Fig. 3.8, the aggregate interference power experienced at the reference UAV-BS from 9 UAV-UEs, all of them located closer than the serving node, is maximized and thus the overall coverage probability is severely degraded. In this case, notice that there is a large difference in the performance when the 5-th nearest node and the cell-edge UAV-UE are chosen as the serving nodes. Moreover, it is noticed again that the spherical model provides

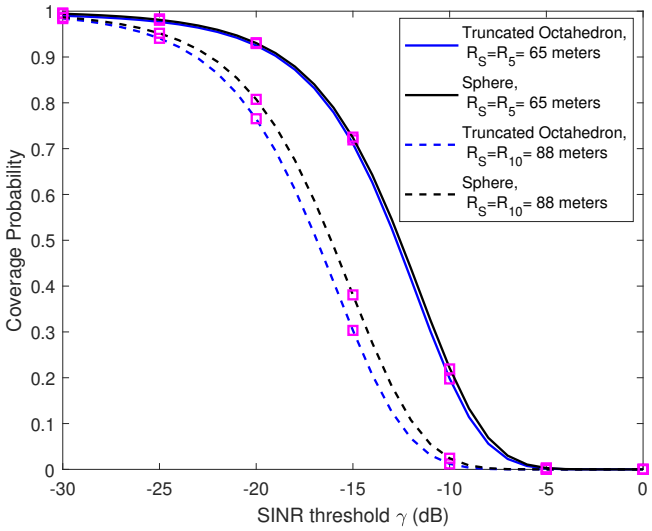

Figure 3.8: Coverage probability versus SINR threshold for different serving distances R_S. Squares denote simulation points.

a more optimistic performance trend in terms of coverage, as compared to the truncated octahedron cell-shape model. This is because of the different geometrical areas between the truncated octahedron and the sphere, in which the interfering UAV-UEs may lie.

Furthermore, Fig. 3.9 compares the coverage probability versus the SINR threshold for different serving distances R_S, under the consideration of intra-cell interference only, derived in Theorem 3.14, with the one under the consideration of the aggregate interference experienced at the reference UAV-BS, derived in Theorem 3.17. The fading and propagation conditions have been set to $m = 4$, $\alpha = 3$, respectively. The difference in coverage performance between the two interference scenarios, is significant for all serving nodes. When the 1st nearest node is selected as the serving node with serving distance $r_s = 40$ meters, the difference in the coverage performance for the two cases is considerably large and all UAV-UEs interfere at the reference UAV-BS in approximately the same degree. When the 5-th nearest node is selected as the serving node with serving distance $r_s = 65$ meters, the difference in the coverage performance for the two cases is still significant. In this case, the aggregate interference is affected more by the 4 dominant interfering UAV-UEs in the near region of the reference UAV-BS, while the rest of the interfering UAV-UEs, including those from the neighboring cells, lie outside the near zone of the reference UAV-BS. The same behaviour is observed when the farthest node is selected as the serving node with serving distance $r_s = 88$ meters. In fact, this is a worst-case performance scenario where the serving node lies near at a corner of the reference cell, while all interfering UAV-UEs, both in the reference cell and in the neighboring cells, hover at distance smaller than the serving distance.

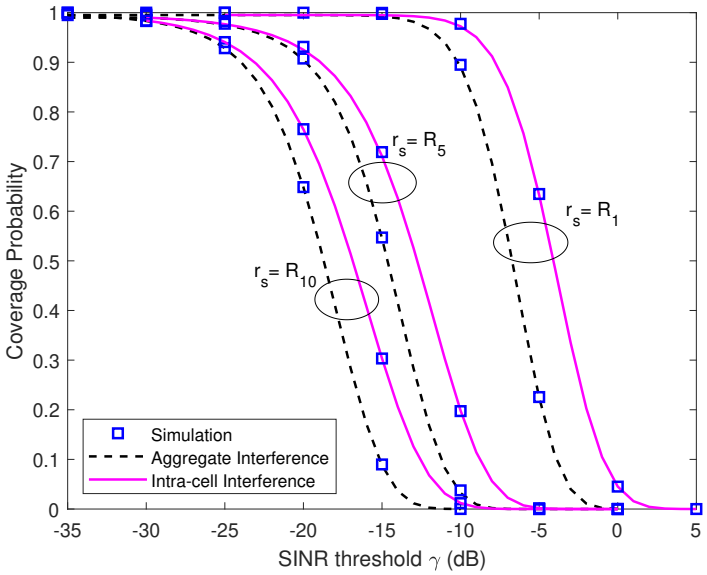

Figure 3.9: Coverage probability versus SINR threshold for different serving distances R_S and interference cases. Squares denote simulation points.

3.5 Chapter Summary

In this chapter, the performance of a 3D UAV wireless network has been analyzed using stochastic geometry tools and the cell shape of a truncated octahedron, which is the closest approximation of a sphere that can tessellate the 3D space. By modeling the spatial locations of the aerial users as a 3D BPP, stochastic geometry analysis in a truncated octahedron-shaped cell, was performed. To this end, the volume of the regions of the cell in which an aerial user may fall, was evaluated. The results then compared to a 3D cell modeled as a sphere, which is a mathematically more tractable model. Subsequently, results about the distances between aerial nodes and their concentration within the two models, were illustrated. Next, coverage probability analysis was conducted under intra-cell interference for both the truncated octahedron and the sphere. Exact form expressions were also derived for the coverage probability under both intra- and a worst case inter-cell interference scenario. The accuracy of the theoretical results was validated through simulation. The results revealed that the spherical model provides a more optimistic performance trend in terms of coverage probability, as compared to the truncated octahedron cell-shape model. In realistic finite 3D networks, this is clearly a consequence of the different geometry of the two cell-shape models and therefore, of the different probabilities regions where a UAV-UE may lie. Note that this chapter was a first yet reasonable step towards the understanding of the binomial 3D cellular network. Building upon the proposed framework, one may extend it so as to integrate UAVs with directional 3D antenna patterns, LoS/NLoS scenarios, mobility models for the UAVs, key enabling technologies for 6G wireless communications (e.g. RIS technology), etc.

As an undoubtedly more tractable cell-shape as compared to the truncated octahedron cell-shape, in the next chapter we conduct a simple yet in-depth performance analysis in terms of key performance metrics and obtain system level insights for a 3D cellular UAV network modeled as a sphere.

Chapter 4

SIR-based Performance Analysis in 3D UAV Networks

4.1 Introduction

As shown in Chapter 3, although the truncated octahedron cell-shape is undoubtedly a realistic 3D cellular network architecture, it has extremely high analytical complexity. In this chapter, a simple yet tractable stochastic geometry framework is proposed to study the performance of a 3D UAV network modeled as a sphere. In this simple scenario, a UAV-BS reference receiver is located at the center of a sphere and communicates with the nearest transmitting UAV node. If sensing-assisted communication is exploited [64], the location of the transmitting UAV node is assumed to be known, otherwise the location inside the sphere is random. The reverse link suffers from the presence of a single dominant interferer, whose location is random within the sphere. Closed-form expressions are derived for key performance metrics for two scenarios, namely for fixed and random location of the desired transmitting node.

4.1.1 Contributions

Modeling of Finite UAV Network in a Sphere & Stochastic Geometry Analysis

A finite number of UAV nodes is uniformly distributed in a sphere. Based on the BPP, a tractable stochastic geometry framework has been developed. This framework is used to calculate the SIR for realistic network scenarios with predetermined number of transmitting UAV nodes.

Closed-form Expressions

Closed-form expressions are derived for key performance indicators, namely the coverage probability, BER, average output SIR, and ergodic capacity.

4.2 System Model

Assume that a 3D UAV network comprised of one fixed and a finite number N of transceiving nodes is deployed in a sphere. The locations of the N transceiving nodes are modeled as a uniform BPP, where the nodes are independently and uniformly distributed in the sphere. In stochastic geometry terms, it is implied that the transceiving nodes are uniformly distributed in a finite compact set $A \subset \mathbb{R}^3$. For the needs of the 3D network modeling, let $A = b_3(\boldsymbol{o}, R)$ denote a 3D ball of radius R that is centered at the origin $\boldsymbol{o} \equiv (0, 0, 0)$. In contrast to prior geometrical models assumed, e.g., [57], the sphere is a simple yet realistic 3D model to describe the UAV network coverage space. To the best of the authors' knowledge, no previous work has ever captured the effect of a spherical model in the performance analysis of a finite UAV network. A UAV - base station (UAV-BS) reference receiver is assumed to be located at the origin $\boldsymbol{o}$ and communicates with the nearest node out of the N transceiving nodes. This work focuses on the reverse link analysis and therefore, the nearest transceiving node is referred to as the desired transmitting node and the reverse link as the reference link. The distance of the transmitting node to the reference receiver is denoted by R_s. The thermal noise is assumed to be negligible as compared to the interference experienced by the receiver [57]. Once the reference link has been established, the remaining transceiving nodes are uniformly distributed in $b_3(\boldsymbol{o}, R) \setminus b_3(\boldsymbol{o}, s)$. In principle, the reference link may suffer from undesired signals from many interfering nodes. However, for mathematical tractability purposes, this work considers only one dominant interfering node, which is the nearest transmitting node outside the area $b_3(\boldsymbol{o}, s)$, i.e., the second nearest node to the UAV-BS reference receiver. Such an assumption is quite common in the open technical literature, e.g., [65, 66]. Indeed, in [65], only one ground-based interferer is considered in the performance analysis, while in [66], it is stated that the CP has similar trend when multiple interfering nodes or one dominant interfering node are considered. The link between the dominant interfering node and the UAV-BS reference receiver is referred to as the interfering link and the distance of the interfering node to the reference receiver is denoted by R_I. After establishing the reference link, the distance distribution of R_I is no longer independent of the distance R_s. In this case, the PDF of the distance R_I conditioned by the distance of the reference link $R_s = y$, is given by [46]

$$f_{R_I}(r_I | R_s = y) = \frac{3{r_I}^2}{(R^3 - y^3)^{N-1}} \frac{({R^3 - {r_I}^3})^{N-2}}{B(N-1, 1)}. \tag{4.1}$$

The system model described is depicted in Fig. 4.1. The received SIR is defined as

$$SIR = \frac{P_s h_s {R_s}^{-a}}{P_I h_I {R_I}^{-a}}, \tag{4.2}$$

where $(\cdot)^{-a}$ models power path-loss with factor a, and P_s, P_I represent the transmit powers of the transmitting and dominant interfering nodes, respectively. Moreover, the random variable $h \in \{h_s, h_I\}$, models Nakagami-m channel fading for the reference and interfering

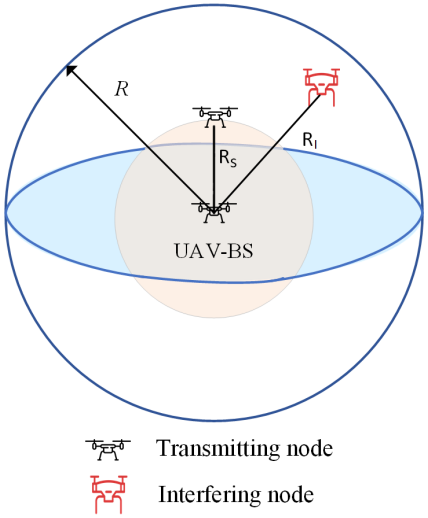

Figure 4.1: Illustration of the system model.

link, respectively, with PDF given by

$$f_h(x) = \frac{x^{m-1}}{\Gamma(m)\theta^m} \exp\Big(-\frac{x}{\theta}\Big), \tag{4.3}$$

where $m \in \{m_s, m_I\}$ is the shape parameter, $\theta \in \{\theta_s, \theta_I\}$ is the scale parameter [67] of the distribution, and $\Gamma(\cdot)$ denotes the Gamma function [40, eq. (8.310.1)]. Note that Nakagami-m fading is a generalized model that mimics various fading environments and simultaneously retains analytical tractability [57].

While the modeling assumptions and the analysis are motivated by the study of UAV networks, the proposed generic framework is designed to incorporate also terrestrial nodes. Towards this direction, two scenarios for the spatial location of the transmitting nodes, are investigated: (i) the transmitting node is assumed to be located at a deterministic distance from the UAV-BS, and (ii) the transmitting node is randomly located. The two scenarios considered, are presented in the following.

4.2.1 Scenario 1: Fixed Location of Desired Transmitting Node

For this system setup, the transmitting node is assumed to be located at a fixed distance s from the center $\boldsymbol{o}$ of A. In this case, (4.2) can be rewritten as

$$SIR = \frac{P_s h_s s^{-a}}{P_I h_I {R_I}^{-a}}. \tag{4.4}$$

An example link for this scenario is the one between a UAV and a ground-based node. Moreover, a typical use-case includes a fixed ground-based node or an aerial one acting as a relay that serves other ground-based nodes. In the latter case, the UAV transmitting node is considered to be fixed in an optimum location for maximum reliability of the link. As already mentioned, a fixed and known location of the transmitting UAV node may be considered by exploiting sensing-assisted communications.

4.2.2 Scenario 2: Random Location of Desired Transmitting Node

The UAV-BS reference receiver once again communicates with the nearest transmitting node. However, in this setup, the distance R_s, between the transmitting node and the UAV-BS reference receiver, is a random variable following a PDF given by

$$f_{R_s}(r_s) = \frac{3r_s^2}{R^{3N}} \frac{(R^3 - r_s^3)^{N-1}}{B(N,1)}. \tag{4.5}$$

For this system setup, the SIR experienced by a UAV-BS reference receiver located at the center $\boldsymbol{o}$ of A is defined as in (4.2). This scenario is a generic one, since all nodes' locations are random, i.e., it is applicable for UAVs and ground-based nodes placed randomly in the considered space.

4.3 Performance Analysis

In this section, the stochastic analysis is conducted in terms of the instantaneous SIR or simply SIR for brevity. Closed-form expressions for the CDF of the SIR for the two scenarios studied, are derived.

4.3.1 Coverage Probability

Scenario 1

As the distance of the reference link is deterministic, with $R_s = s$, the interest turns on defining the distribution of the distance R_I of the interfering link. However, as mentioned in Section II, after establishing the reference link, the distance distribution of R_I is no longer independent of the distance R_s. In this case, for $R_I \in [s, R]$, the PDF of the distance R_I conditioned by the distance of the reference link R_s, results from (4.1), after substituting $y = s$.

Let $I = P_I h_I {R_I}^{-a}$ represent the RV of the denominator of (4.4), directly proportional to the received power of the interfering signal. The conditional PDF of the RV I, given the

interfering link distance r_I, is given by

$$f_{I|R_I}(x|r_I, R_s = s) = \left(\frac{{r_I}^a}{P_I\theta_I}\right)^{m_I} \frac{x^{m_I-1}}{\Gamma(m_I)} \exp\left(-\frac{{r_I}^a x}{P_I\theta_I}\right). \tag{4.6}$$

The unconditional distribution of the RV I can now be obtained by averaging (4.6) over (4.1).

Lemma 4.1. *The PDF $f_I(x|R_s = s)$ of the RV I assuming that the reference link is fixed, is given by*

$$\begin{aligned} &f_I(x|R_s = s) \\ &= \frac{3x^{m_I-1}(P_I\theta_I)^{-m_I}\left(R^3 - s^3\right)^{1-N}}{a\Gamma(m_I)B(N-1,1)} \sum_{k=0}^{N-2} \binom{N-2}{k} R^{3N-3k-6}(-1)^k s^{am_I+3k+3} E_{\frac{a-am_I+3k-3}{a}}\left(\frac{s^a x}{\theta_I P_I}\right) \\ &- \frac{3x^{m_I-1}(P_I\theta_I)^{-m_I}\left(R^3 - s^3\right)^{1-N}}{a\Gamma(m_I)B(N-1,1)} \sum_{k=0}^{N-2} \binom{N-2}{k} R^{3N-3k-6}(-1)^k R^{am_I+3k+3} E_{\frac{a-am_I+3k-3}{a}}\left(\frac{R^a x}{\theta_I P_I}\right), \end{aligned} \tag{4.7}$$

where $E_n(\cdot)$ denotes the exponential integral function [68, eq. (06.34.02.0001.01)] and $B(\cdot,\cdot)$ the Beta function [40, eq. (8.380.1)].

Proof: See Appendix C.1. □

The random variable of the nominator of (4.4), $S = P_s h_s {R_s}^{-a}$, is directly proportional to the received power experienced by the UAV-BS reference receiver. The PDF of the random variable S results immediately from [67] with a simple change of variable and has similar form with (4.6). The distribution of the SIR can now be derived in the following Lemma.

Lemma 4.2. *The PDF of the SIR denoted as $f_{SIR}^{fix}(\gamma|R_s = s)$, is given by*

$$f_{SIR}^{fix}(\gamma|R_s = s) = \frac{3\gamma^{-(m_I+1)}\left(P_s s^{-a}\theta_s\right)^{m_I}\left(P_I\theta_I\right)^{-m_I}}{\left(R^3 - s^3\right)^{N-1} B(N-1,1)B(m_s,m_I)}\left(Z(s) - Z(R)\right), \tag{4.8}$$

with

$$\begin{aligned} Z(j) = &\sum_{k=0}^{N-2} \binom{N-2}{k}(-1)^k \frac{R^{3N-3k-6}}{am_s - 3k - 3} j^{am_I+3k+3}\left(\frac{P_s s^{-a}\theta_s}{P_I j^{-a}\theta_I\gamma}\right)^{-(m_s+m_I)} \\ &\times {}_2F_1\left(\frac{am_s - 3k - 3}{a}, m_s + m_I; \frac{am_s + a - 3k - 3}{a}; -\frac{P_I j^{-a}\theta_I\gamma}{P_s s^{-a}\theta_s}\right), \quad j = \{s, R\}, \end{aligned} \tag{4.9}$$

where ${}_2F_1(\cdot)$ is the Gauss hypergeometric function [40, eq. (9.100)].

Proof: See Appendix C.2. □

The corresponding CDF is now derived from (4.8) in the following Lemma.

Lemma 4.3. *The CDF $F_{SIR}^{fix}(\gamma|R_s=s)$ of a UAV-BS reference receiver served by its nearest, fixed-located node in the presence of a dominant interferer, is given in closed form by*

$$F_{SIR}^{fix}(\gamma|R_s=s)=\frac{3\gamma^{m_s}\left(P_s s^{-a}\theta_s\right)^{m_I}\left(P_I\theta_I\right)^{-m_I}}{\left(R^3-s^3\right)^{N-1}B(N-1,1)B(m_s,m_I)m_s}\sum_{k=0}^{N-2}\binom{N-2}{k}R^{3N-3k-6}\frac{(-1)^k}{am_s-3k-3}$$
$$\times\left\{\frac{s^{am_s+3k+3}}{\left(\frac{P_s\theta_s}{P_I\theta_I}\right)^{(m_s+m_I)}}\,{}_3F_2\left(\frac{am_s-3k-3}{a},m_s+m_I,m_s;\frac{am_s+a-3k-3}{a},m_s+1;-\frac{P_I\theta_I}{P_s\theta_s}\gamma\right)-\right.$$
$$\left.\frac{R^{am_s+3k+3}}{\left(\frac{P_s s^{-a}\theta_s}{P_I R^{-a}\theta_I}\right)^{(m_s+m_I)}}\,{}_3F_2\left(\frac{am_s-3k-3}{a},m_s+m_I,m_s;\frac{am_s+a-3k-3}{a},m_s+1;-\frac{P_I R^{-a}\theta_I}{P_s s^{-a}\theta_s}\gamma\right)\right\},\tag{4.10}$$

where ${}_3F_2(\cdot)$ is the generalized hypergeometric function [40, eq. (9.14.1)].

Proof: See Appendix C.3. □

Scenario 2

Next, the scenario where the distance of the reference link is no longer deterministic, is investigated. For this case, it is mathematically convenient to characterize the ratio distribution of $H=\frac{P_s h_s}{P_I h_I}$. Through simple change of variables, the PDF of H can be easily obtained as

$$f_H(y)=\frac{y^{m_s-1}\left(\frac{P_I}{P_s}\right)^{m_s}\left(\frac{1}{\theta_I}+\frac{yP_I}{P_s\theta_s}\right)^{-m_s-m_I}}{B(m_s,m_I)\theta_s^{m_s}\theta_I^{m_I}}.\tag{4.11}$$

In addition, based on [40, eq. (3.194.1)] the corresponding CDF $F_H(x)$, results immediately to

$$F_H(x)=\frac{\left(\frac{P_I\theta_I}{P_s\theta_s}x\right)^{m_s}}{m_sB(m_s,m_I)}\,{}_2F_1\left(m_s,m_s+m_I;1+m_s;-\frac{\theta_I P_I}{\theta_s P_s}x\right).\tag{4.12}$$

Note that in this setup, it is mathematically convenient to consider the product of random variables resulting in the received SIR. Towards this direction, the distribution of the ratio V of random distances R_s/R_I is first obtained. Notice that the two random variables are dependent. In this context, let $V=R_s/R_I$ represent the ratio of the distances. Through a change of variables, R_I can be expressed as $R_I=R_s/V$. The corresponding CDF and PDF of the random variable V are provided in the following Lemma.

Lemma 4.4. *The CDF and PDF of V are respectively given by*

$$F_V(v) = v^3 \text{ and } f_V(v) = 3v^2. \tag{4.13}$$

Proof: See Appendix C.4. □

Interestingly, it is noticed that the distribution of ratio V confirms i) a square dependence between distances and ii) independence from the number of nodes N and the radius R, i.e., from the area of the spherical region of the network. Based on (4.12) and (4.13), the CDF $F_{SIR}^{rand}(\gamma)$ of SIR can now be obtained as

$$F_{SIR}^{rand}(\gamma) = \mathbb{P}(SIR \leq \gamma) = \mathbb{P}(HV^{-a} \leq \gamma) = \mathbb{E}_V \left\{ F_H(\gamma V^a), \right\}, \tag{4.14}$$

where $\mathbb{E}[\cdot]$ denotes the expectation operator and $\mathbb{P}(\cdot)$ denotes probability operator.

The above equation results in the following Lemma.

Lemma 4.5. *The CDF $F_{SIR}^{rand}(\gamma)$ and the corresponding PDF $f_{SIR}^{rand}(\gamma)$ are respectively given by*

$$F_{SIR}^{rand}(\gamma) = \left(\frac{P_I\theta_I}{P_s\theta_s}\right)^{m_s} \frac{3\gamma^{m_s}\, {}_3F_2\left(m_s, m_s+m_I, m_s+\frac{3}{a}; 1+m_s, m_s+\frac{3}{a}+1; -\frac{P_I\theta_I}{P_s\theta_s}\gamma\right)}{m_s\left(am_s+3\right)B(m_s, m_I)}, \tag{4.15}$$

$$f_{SIR}^{rand}(\gamma) = \left(\frac{P_I\theta_I}{P_s\theta_s}\right)^{m_s} \frac{3\gamma^{m_s-1}\, {}_2F_1\left(\frac{3}{a}+m_s, m_s+m_I; 1+\frac{3}{a}+m_s; -\frac{P_I\theta_I}{P_s\theta_s}\gamma\right)}{(am_s+3)B(m_s, m_I)}. \tag{4.16}$$

Proof: See Appendix C.5. □

The coverage probability is mathematically be expressed as

$$P_c = \mathbb{P}(SIR > \gamma_{\text{th}}) = 1 - \mathbb{P}(SIR \leq \gamma_{\text{th}}). \tag{4.17}$$

and can now lead to the following Propositions for the coverage probability for the two scenarios.

Proposition 4.6. *Under Scenario 1, the coverage probability is expressed as $P_c = 1 - F_{SIR}^{fix}(\gamma_{\text{th}}|R_s = s)$.*

Proposition 4.7. *Under Scenario 2, the coverage probability is expressed as $P_c = 1 - F_{SIR}^{rand}(\gamma_{\text{th}})$*

4.3.2 BER

Next, the performance of the two scenarios, is evaluated in terms of the average BER for binary modulation schemes. The average BER is the metric that is most revealing about the nature of the system behavior and the one most often illustrated in works containing system performance evaluation studies [69], [70], [71]. Using the CDF-based approach proposed in [72], the average BER is obtained by integrating the derivative of conditional error probability (CEP) $P_e'(\gamma)$, over the respective CDF of the SIR of each scenario. The average BER is then given by

$$\bar{P}_{e,p} = \int_0^\infty -P_e'(\gamma) F_{SIR}^p(\gamma) \mathrm{d}\gamma, \tag{4.18}$$

where $Q(\cdot)$ is the area under the tail of the Gaussian PDF defined as [73, eq. (2-1-97)] and $p \in \{fix, rand\}$. Moreover, $P_e(\gamma) = Q(\sqrt{2\gamma})$ for binary phase-shift keying (BPSK) and $P_e(\gamma) = \frac{1}{2}e^{-\frac{\gamma}{2}}$ for differential BPSK (DBPSK).

Scenario 1

The average BER is first derived for *Scenario 1* in the following Proposition.

Proposition 4.8. *Given the fixed distance s of the reference link, the average BER for the BPSK and DBPSK modulation schemes are given by*

$$\begin{aligned}\bar{P}_{e,fix}^{BPSK} = & \\ & \frac{3\pi^{-\frac{1}{2}}\left(R^3 - s^3\right)^{1-N} \sum_{k=0}^{N-2} \binom{N-2}{k} R^{3N-3k-6}(-1)^k s^{3k+3} G_{3,4}^{4,1}\left(\frac{P_s\theta_s}{P_I\theta_I}\middle| \begin{matrix} 1-m_s, \frac{-3+a-3k}{a}, 1 \\ \frac{1}{2}, \frac{-3-3k}{a}, m_I, 0 \end{matrix}\right)}{2a\Gamma(m_s+m_I)B(N-1,1)B(m_s,m_I)} \\ & - \frac{3\pi^{-\frac{1}{2}}\left(R^3 - s^3\right)^{1-N} \sum_{k=0}^{N-2} \binom{N-2}{k} R^{3N-3k-3}(-1)^k G_{3,4}^{4,1}\left(\frac{s^{-a}P_s\theta_s}{R^{-a}P_I\theta_I}\middle| \begin{matrix} 1-m_s, \frac{-3+a-3k}{a}, 1 \\ \frac{1}{2}, \frac{-3-3k}{a}, m_I, 0 \end{matrix}\right)}{2a\Gamma(m_s+m_I)B(N-1,1)B(m_s,m_I)}. \end{aligned} \tag{4.19}$$

$$\begin{aligned}\bar{P}_{e,fix}^{DBPSK} = & \\ & \frac{3\left(R^3 - s^3\right)^{1-N} \sum_{k=0}^{N-2} \binom{N-2}{k} R^{3N-3k-6}(-1)^k s^{3k+3} G_{3,4}^{4,1}\left(\frac{P_s\theta_s}{P_I\theta_I}\middle| \begin{matrix} 1-m_s, \frac{-3+a-3k}{a}, 1 \\ 1, \frac{-3-3k}{a}, m_I, 0 \end{matrix}\right)}{2a\Gamma(m_s+m_I)B(N-1,1)B(m_s,m_I)} \\ & - \frac{3\left(R^3 - s^3\right)^{1-N} \sum_{k=0}^{N-2} \binom{N-2}{k} R^{3N-3k-3}(-1)^k G_{3,4}^{4,1}\left(\frac{s^{-a}P_s\theta_s}{R^{-a}P_I\theta_I}\middle| \begin{matrix} 1-m_s, \frac{-3+a-3k}{a}, 1 \\ 1, \frac{-3-3k}{a}, m_I, 0 \end{matrix}\right)}{2a\Gamma(m_s+m_I)B(N-1,1)B(m_s,m_I)}. \end{aligned} \tag{4.20}$$

respectively, where $G_{p,q}^{m,n}(x)$ is the Meijer G-function defined in [40, eq. (9.301)].

Proof: See Appendix C.6. □

Scenario 2

The average BER for *Scenario 2*, is formally presented in the following Proposition.

Proposition 4.9. *Given a random location R_s of the transmitting node, the average BER for binary modulation schemes is given by*

$$\bar{P}_{e,rand}^{BPSK} = \frac{3G_{3,4}^{4,1}\left(\frac{P_s\theta_s}{P_I\theta_I}\middle|\begin{matrix}1-m_s, 1, \frac{3}{a}+1\\ 0.5, 0, m_I, \frac{3}{a}\end{matrix}\right)}{2a\sqrt{\pi}\Gamma(m_s+m_I)B(m_s,m_I)} \tag{4.21}$$

and

$$\bar{P}_{e,rand}^{DBPSK} = \frac{3G_{3,4}^{4,1}\left(\frac{P_s\theta_s}{P_I\theta_I}\middle|\begin{matrix}1-m_s, 1, \frac{3}{a}+1\\ 0.5, 0, m_I, \frac{3}{a}\end{matrix}\right)}{2a\Gamma(m_s+m_I)B(m_s,m_I)}. \tag{4.22}$$

Proof: By following a similar procedure as the one presented for deriving the BER in *Scenario 1*, the previously presented closed-form expressions for the BER are deduced. □

4.3.3 Average Output SIR

In this subsection, the analysis focuses on studying the network performance in terms of the average output SIR for the generic scenario where the distance of the reference link is random. The average output SIR can be calculated by

$$\bar{\gamma} = \int_0^\infty \gamma f_{SIR}^{rand}(\gamma)\mathrm{d}\gamma. \tag{4.23}$$

The above equation results in the following Proposition.

Proposition 4.10. *Given a random location R_s of the transmitting node, the average output SIR is given by*

$$\bar{\gamma} = \frac{P_s\theta_s}{P_I\theta_I}\frac{3m_s}{(m_I-1)(3-a)}. \tag{4.24}$$

Proof: Through the change of variable $\frac{P_I\theta_I}{P_s\theta_s}\gamma = y$ in (4.16), the integral in (4.23) can be easily derived in closed form by using [68, eq. (07.23.21.0014.01)]. After applying some simplifications, (4.24) yields immediately. □

Note that (4.24) holds for $a < 3$, which is a valid and logical restriction for UAV-enabled networks, in which the path-loss factor takes values 1-3 for LoS scenarios, i.e., [57],[74].

4.3.4 Ergodic Capacity

The ergodic channel capacity quantifies the maximum achievable rate that can be supported by the subjected channel. In this subsection, the ergodic capacity is leveraged to measure the achievable rate of the network for the generic scenario where the distance from the defined UAV-BS node is random. It is defined as follows

$$\bar{C} = BW \int_0^\infty \log_2(1+\gamma) f_{SIR}^{rand}(\gamma) \mathrm{d}\gamma, \tag{4.25}$$

where BW denotes the channel's bandwidth. The ergodic capacity can now be evaluated through the following Proposition.

Proposition 4.11. *Given a random location R_s of the transmitting node, the ergodic channel capacity is given by*

$$\bar{C} = BW \frac{3}{\ln 2 \Gamma(m_s)\Gamma(m_I) a} \frac{P_I \theta_I}{P_s \theta_s} G_{4,4}^{3,3}\left(\frac{P_I \theta_I}{P_s \theta_s} \middle| \begin{matrix} -\frac{3}{a}, -m_I, -1, 0 \\ m_s - 1, -1, -1, -1 - \frac{3}{a} \end{matrix} \right). \tag{4.26}$$

Proof: See Appendix C.7. □

4.4 Numerical Results and Discussions

In this section, representative numerical examples have been prepared using the expressions derived in the previous sections, while simulation results were also used for verification purposes. The numerical results for the performance of the proposed framework in terms of coverage probability, average BER and ergodic capacity are also discussed to reveal system level insights.

4.4.1 Coverage Probability

For all system setups $\theta_s = \theta_I = 1$, in order to compare the same Nakagami fading conditions and $P_s = P_I = 0dBm$, in order to preserve equal transmit powers, unless otherwise stated. Other simulation parameters are $a = 3$ and $m_s = m_I = 2.75$ to consider the same severity of fading. Note that these values are typically considered for UAV-enabled communication scenarios and approach LoS propagation conditions [74], [75],[8]. For *Scenario 1*, a finite network of UAVs is simulated with $N = 10$, inside a sphere of radius $R = 100$ meters, and the coverage probability is evaluated for various simulation parameters. In Fig. 4.2, the coverage probability is plotted as a function of R for different values of γ_{th}. One can observe that for small values of R, i.e., for a small-sized networks, the coverage probability degrades rapidly while moving towards more demanding values of γ_{th}. In contrast to this, for large

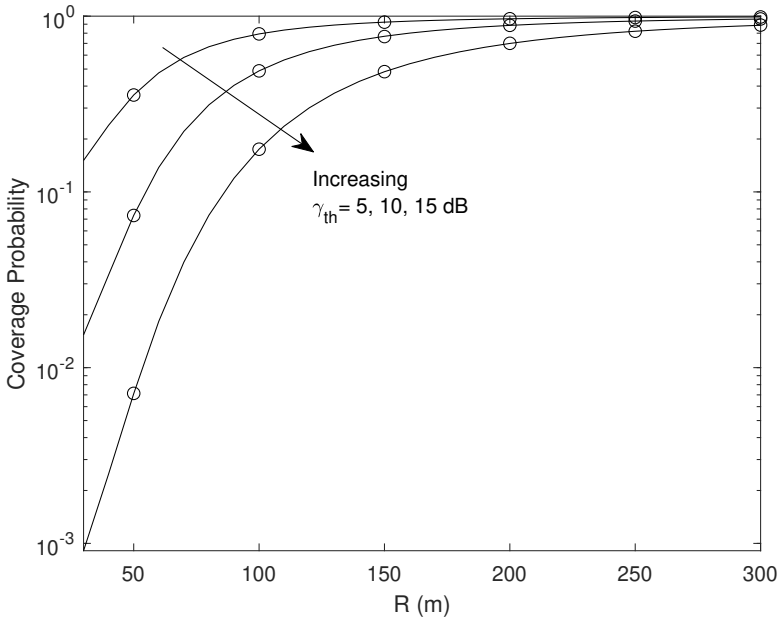

Figure 4.2: Coverage probability versus R for different values of γ_{th} for *Scenario 1* (circles denote simulation points).

values of R, i.e., for a large-sized network, the probability that acceptable communication is established is very high even for demanding values of γ_{th}. Indeed, an increase of the size of the network area increases the probability that the distance of the interfering link is longer than the one of the reference link.

In Fig. 4.3, the coverage probability of the UAV-BS reference receiver is plotted as a function of the distance s. Note that s is expressed as a percentage of R. It can be observed that the more demanding the values of γ_{th} are, the more rapid is the degradation of coverage probability as the transmitting node moves closer to the network edge. For the rest of the plots, it is assumed that $s = 20$ meters.

Fig. 4.4 is the representative plot chosen to compare the two scenarios for different values of s and N. It is observed that when $s = 20$ meters, the coverage probability of *Scenario 1* is far better than the coverage probability of *Scenario 2*, even for $N = 10$. However, with the increase of s, i.e., while moving the transmitting node towards the edge of the network, it is more likely that the distance values of the interfering and the reference link are approximately equal for *Scenario 1*. In this case, the coverage probability of *Scenario 2* outperforms the coverage probability of *Scenario 1* even for $N = 5$. Moreover, with the increase of N, the coverage probability is worsened as expected. Another important conclusion from Fig. 4.4 is the necessity for 3D modeling of UAV networks. Indeed, comparing the 2D and 3D model curves for *Scenario 2*, it is observed that the 2D BPP model provides optimistic coverage probability compared to the realistic one provided by 3D BPP. This fact, further motivates

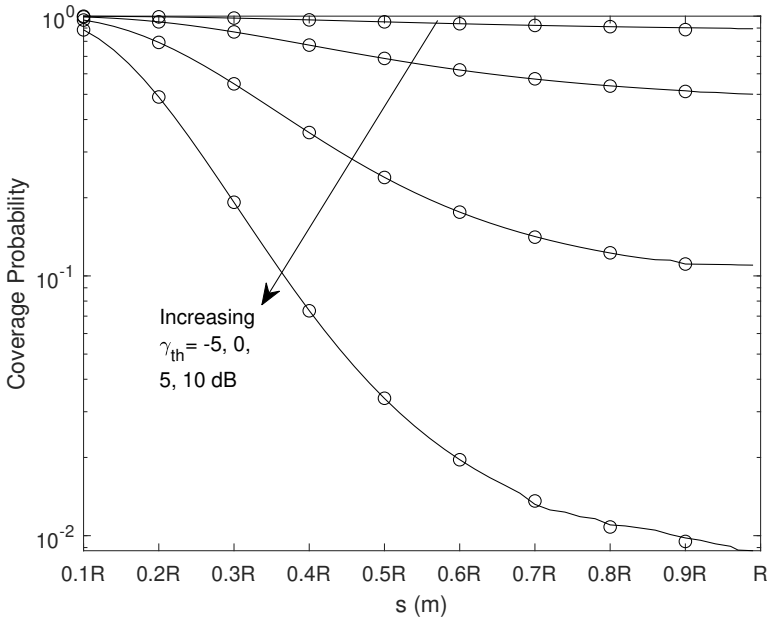

Figure 4.3: Coverage probability versus distance s (expressed as a percentage of radius R) for different values of γ_{th} for *Scenario 1* (circles denote simulation points).

the study of 3D network models.

For *Scenario 2*, the coverage probability is independent of the system parameters R, N. In Fig. 4.5, the coverage probability is plotted as a function of γ_{th} for different fading conditions and path loss exponent values. In this figure, it is shown that the better the channel conditions are, the worse the coverage probability is achieved. This observation includes, both the mean received power dominated by the path loss exponent and the fading conditions, implied by the parameters m_s, m_I. This is because the interfering link gets stronger and this is more profound for larger values of γ_{th}. The second observation is that there is a cross point for small values of γ_{th} where the behaviour of coverage probability is inverted, i.e., the coverage probability is slightly larger for better channel conditions. It should be pointed out that higher values of Nakagami-m parameter ($m_s = m_I = 4$) model sufficiently LoS propagation environment [74].

For the sake of BER performance evaluation of *Scenario 1*, a finite network of UAVs is simulated with $N = 10$, in a sphere of radius $R = 200$ meters and the average BER as a function of the transmit power P_s is computed. The utilized simulation parameters are $a = 3$ and $m_s = m_I = 2.75$. In Fig. 4.6, the average BER is plotted for different values of the serving distance s for the BPSK modulation scheme. Once again, the distance s is given as a function of the sphere radius R. It is observed that as s increases, the performance of the average BER degrades but the degradation is gradually smaller.

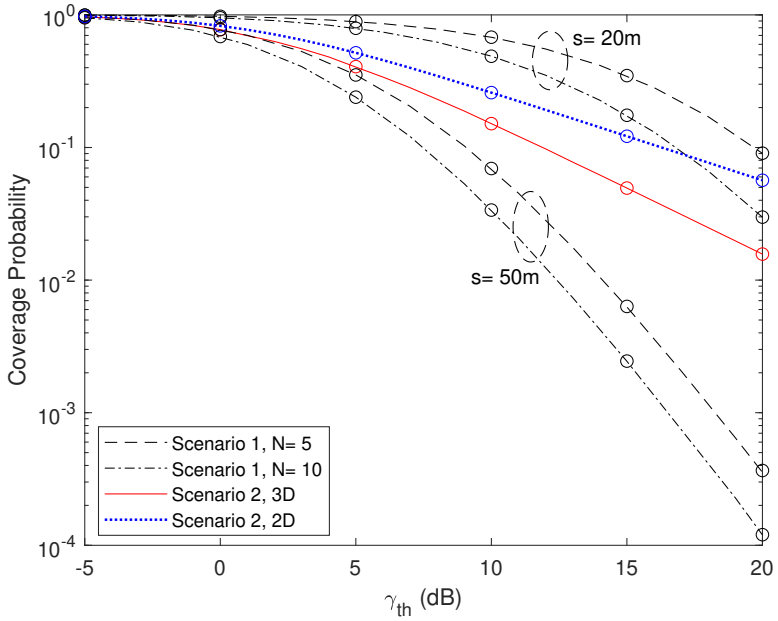

Figure 4.4: Comparison of coverage probability versus γ_{th} for the two scenarios (circles denote simulation points).

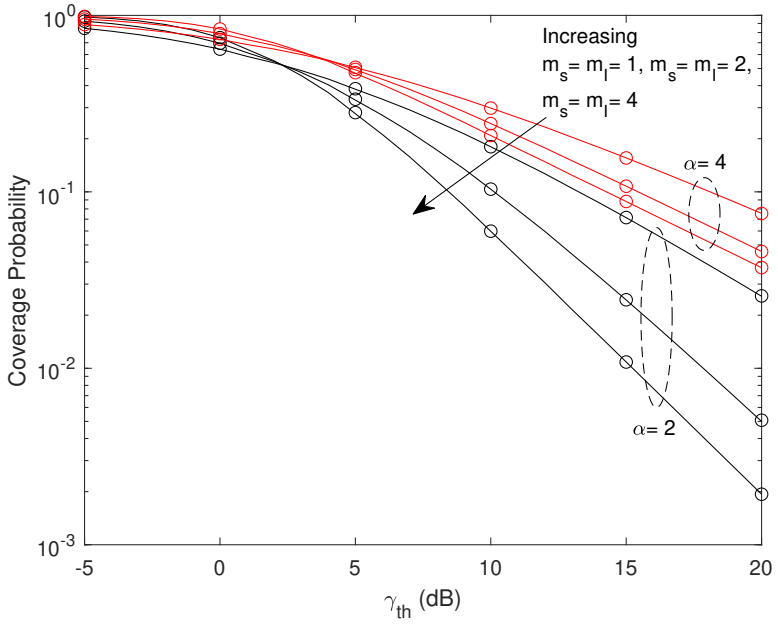

Figure 4.5: Coverage probability versus γ_{th} for different values of m_s, m_I for *Scenario 2* (circles denote simulation points).

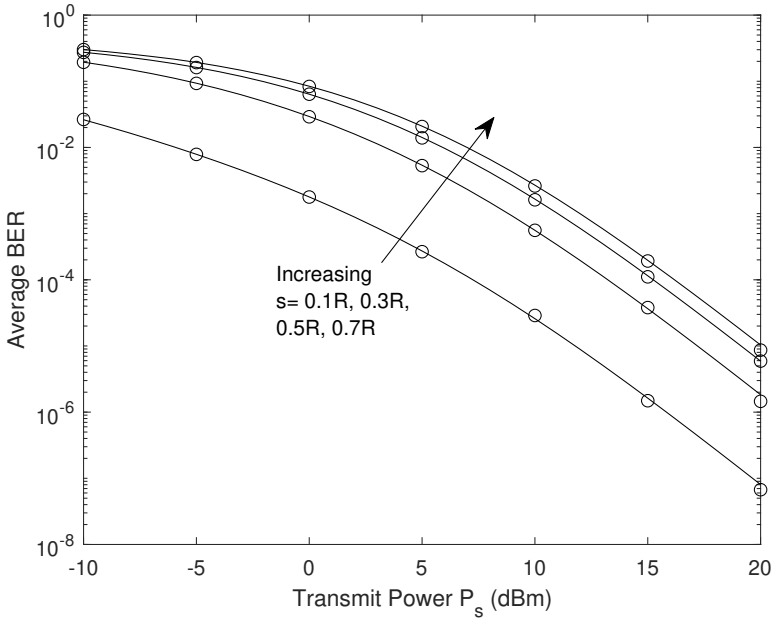

Figure 4.6: Average BER for BPSK versus P_s for *Scenario 1* (circles denote simulation points).

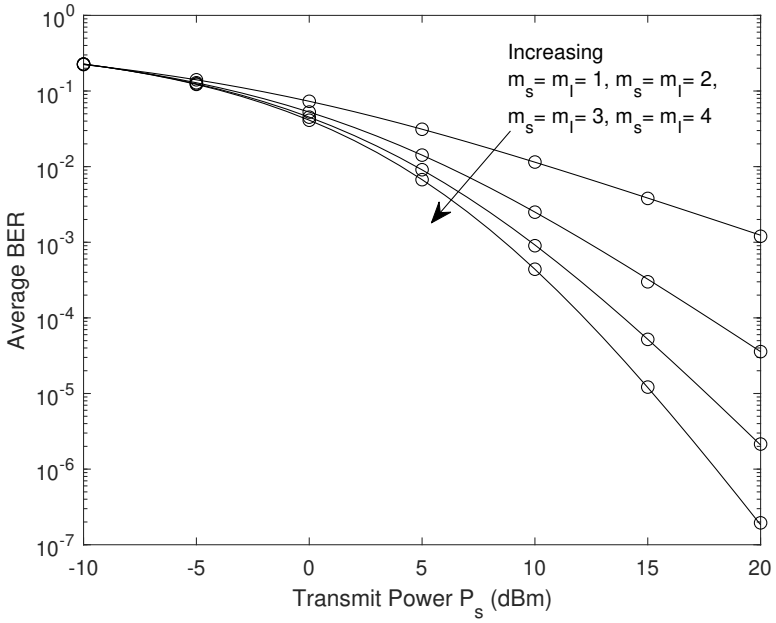

Figure 4.7: Average BER for BPSK versus P_s for *Scenario 2* (circles denote simulation points).

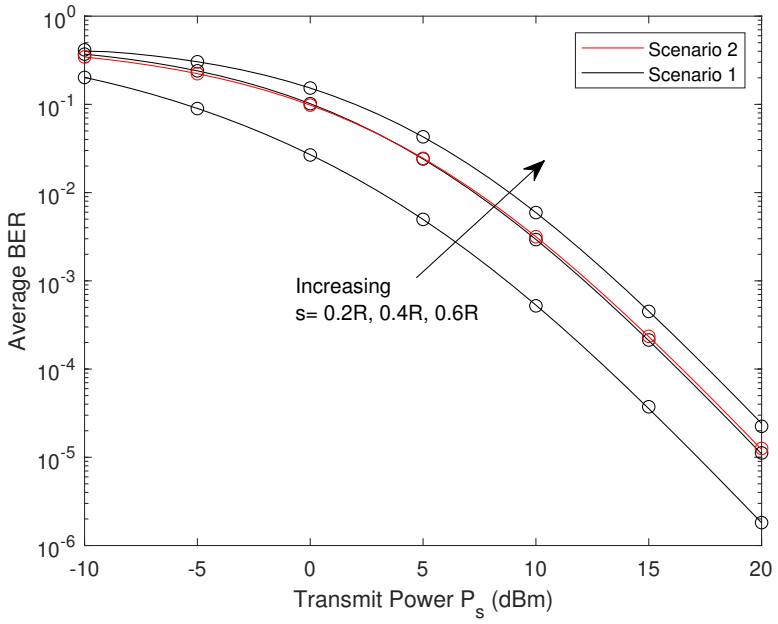

Figure 4.8: Comparison of the two scenarios in terms of average BER versus P_s for DBPSK (circles denote simulation points).

For *Scenario 2*, the average BER of binary modulation schemes is compared for different values of the channel fading parameters m_s, m_I. In Fig. 4.7, the average BER is plotted as a function of the transmit power P_s for the BPSK modulation scheme. It can be observed that as P_s increases, the average BER becomes significantly better when moving from severe fading ($m_s = m_I = 1$) to less-severe fading ($m_s = m_I = 4$) conditions. In other words, when severe fading is present, non-LoS (NLoS) propagation conditions exist and the performance of the average BER is significantly degraded.

In Fig. 4.8, the average BER is plotted as a function of the transmit power P_s for both scenarios, for the DBPSK, and for different values of s. It is observed that the performance of *Scenario 2* approximates the performance of *Scenario 1*, when $s = 0.4R$. When $s = 0.2R$, the average BER of *Scenario 1* is far better than the corresponding of *Scenario 2*. However, for $s > 0.4R$, i.e., when the transmitting node starts moving towards the edge of the network, the performance of *Scenario 2* is clearly better.

Remark 4.12. The demonstrated results enable the system designer to quantify the effects of the distance s, transmit power, and Nakagami - m fading parameter on the error performance of a UAV-BS reference receiver.

Next, the performance of the network in terms of the achievable rate is evaluated. As shown from the analytical expression, the ergodic capacity is independent of the system parameters R, N. The utilized simulation parameters are $a = 2$, $\theta_s = \frac{1}{m_s}$ and $\theta_I = \frac{1}{m_I}$, respectively,

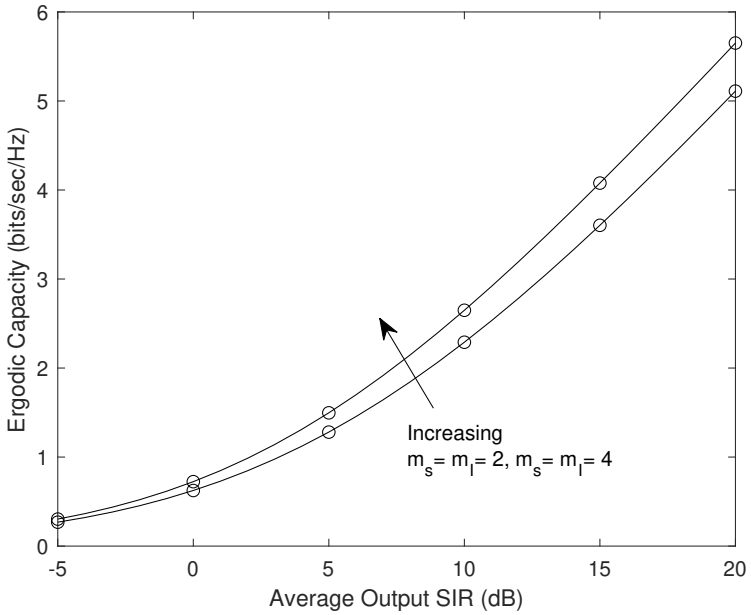

Figure 4.9: Ergodic Capacity versus average output SIR for *Scenario 2* (circles denote simulation points).

so that the expectation of Nakagami fading equals to unity and P_I= 0dBm. In Fig. 4.9, the normalized ergodic capacity $\bar{C}/BW$ is plotted as a function of $\bar{\gamma}$ for different fading conditions. For the needs of the numerical evaluation, the simulation parameter P_s is set such that a desired output SIR is achieved every time. It can be observed that with the increase of average output SIR, the achievable rate increases as expected. As the fading conditions become more favorable, capacity increases. However, it can be observed that in the low average SIR region, the increment is rather small.

4.5 Chapter Summary

In this chapter, a mathematical framework for studying the performance analysis of finite wireless 3D UAV networks is proposed. The model assumes a UAV-BS reference receiver communicating with its nearest transmitting node, while suffering from interference from a dominant interfering node. Modeling the locations of nodes as a uniform BPP, two scenarios are examined: 1) the transmitting node is at a fixed and known distance from the UAV-BS reference receiver and 2) the transmitting node is randomly located in the spherical-shaped network area. The presented framework is utilized to study the statistics of the received SIR, the coverage probability, and the average BER for binary modulation schemes for the two scenarios. Finally, the calculation of the average output SIR is leveraged to study the

ergodic capacity of the network. It is also clear that the proposed framework although simple yields high analytical tractability and therefore, can directly serve as baseline framework for the development of more complicated ones, which integrate 6G key enabling technologies. Subsequently, performance analysis in terms of key performance metrics can similarly be conducted.

Having presented both the truncated octahedron-based 3D cellular network and a more tractable 3D cellular network in Chapters 3 and 4, respectively, a simple yet direct extension is to conduct a performance comparison between the two cellular networks in the presence of multiple interfering UAV nodes to obtain key system level insights for the design and performance of beyond 5G cellular 3D network. The motivation of the next chapter is triggered by the aforementioned.

Chapter 5

Performance comparison of wireless aerial 3D cellular network models

5.1 Introduction

In Chapter 3, it became clear that realistic point processes should be employed to model the locations of UAVs in 3D networks and therefore accurately capture key performance metrics for obtaining design insights. Accordingly, a comprehensive performance analysis in terms of the uplink coverage probability in a truncated octahedron-based cellular network, was conducted. It is worth reminding that the truncated octahedron cell-shape is the closest approximation to the sphere that can tessellate the entire 3D space with the minimum number of polyhedrons in a similar manner with the hexagonal cell in the 2D cellular networks. To reduce the analytical complexity of the proposed framework, in Chapter 4, it was highlighted that i) a sphere cell-shape can reasonably approximate the radiation pattern of an isotropic base station antenna, ii)can capture the effect of the 3D space, and iii) can serve as baseline 3D cell-shape for integrating 6G key enabling technologies. Nevertheless, as rigorously argued in Chapter 3, a sphere cell-shape clearly cannot tessellate the 3D space, i.e., fill the entire 3D space with no gaps or overlaps.

To bring more light to the aforementioned debate, in this final technical Chapter, by employing the 3D PPP for the spatial locations of UAV-UEs, performance analysis in terms of coverage probability and average rate is conducted in a regular UAV network. Next, performance analysis is conducted for a finite realistic binomial-Voronoi UAV network, deployed in 3D space. This network model introduces randomness in both the spatial deployment of the UAV-BS and the cell structure, while in the same time allows for a tractable analysis. Indeed, closed-form expression for the Laplace transform of the aggregate interference is derived as intermediate step in the coverage probability analysis. Finally, the analytical and simulation results are presented to investigate the performance achieved by the proposed network models. Also, the performance in a binomial-Voronoi network is compared to the one in a truncated octahedron-based cellular network with the spatial locations of the UAV-UEs following a 3D PPP, referred to as regular network in the following, with uniformly random selection policy. While the actual UAV-BS 3D deployment is neither absolutely well-defined nor totally random in practice, performance comparison is conducted to obtain design insights and highlight the benefits of each model as a candidate 3D cellular UAV

network for beyond-5G wireless communication systems.

5.2 System and Channel Models

5.2.1 Truncated Octahedron-based Network

Consider a 3D cell modeled as a truncated octahedron, $W \subset \mathbb{R}^3$, with 14 faces and edge length R. Without loss of generality, it is assumed that W is centered at the origin $o = [x_0, y_0, z_0]^T = [0, 0, 0]^T$ of the 3D Cartesian coordinate system, and is referred to as the *reference cell*. In this case, the 3D cellular network consists of a predefined arrangement of multiple truncated octahedron cells. The desired 3D space can be tessellated with multiple copies of the truncated octahedron cell without any gap or overlap. In this work, only the first tier of the 3D cellular network is considered, i.e., $N_c = 14$ adjacent cells with respect to the reference cell are deployed, and will be referred to as the *neighboring cells*. The UAV-BSs are located at the center of the cells. The UAV-BS hovering at o in the reference cell will be referred to as the *reference UAV-BS*. The model is depicted in Fig. 5.1a. The 3D locations of the UAV-BS at the centers of the neighboring cells are given in Cartesian coordinates by the matrix [5, Theorem 1]

$$\mathbf{P}_{\{a,b,c\}} = \sqrt{2}R\mathbf{H}, \tag{5.1}$$

where $a, b, c \in \{-1, 0, 1\}$ and the matrix $\mathbf{H}$ is given by

$$\mathbf{H} = \begin{bmatrix} -1 & -1 & -1 & 1 & 1 & -1 & 1 & 1 & -2 & 0 & 0 & 2 & 0 & 0 \\ -1 & 1 & -1 & -1 & -1 & 1 & 1 & 1 & 0 & -2 & 0 & 0 & 2 & 0 \\ -1 & -1 & 1 & 1 & -1 & 1 & -1 & 1 & 0 & 0 & -2 & 0 & 0 & 2 \end{bmatrix}, \tag{5.2}$$

where each column of $\mathbf{H}$ represents the normalized 3D coordinates of the N_c UAV-BSs.

Consider the forward transmission from the UAV-BSs to UAV-UEs, the spatial locations of which are distributed according to a homogeneous PPP Φ with intensity λ. The reference UAV-BS is assumed to serve the n-th nearest UAV-UE of Φ, which is referred to as the *receiver* and without loss of generality, is assumed to hover in the reference cell. Let $\mathbf{p}_i = [x_{p_i}, y_{p_i}, z_{p_i}]^T$, $i = 1, ..., N_c$ denote the deterministic 3D location of the i-th UAV-BS obtained from the i-th column of $\mathbf{P}$. Also, let $\mathbf{w}_n = [r_n, \theta_n, \phi_n]^T$ denote the 3D location of the receiver in spherical coordinates. Then, $\mathbf{w}_n^c = [r_n \cos(\phi_n) \sin(\theta_n), r_n \sin(\phi_n) \sin(\theta_n), r_n \cos(\theta_n)]^T$ denotes the 3D location of the receiver in Cartesian coordinates. The distance U_i between the receiver and the i-th UAV-BS is denoted by $U_i = ||\mathbf{w}_n^c - \mathbf{p}_i||$. Please note that for a limited time-period the positions of both the UAV-UEs and the UAV-BSs remain fixed, and therefore, the proposed framework is also applicable to mobile UAVs.

In this Chapter, the frequency reuse factor is set to $q = 1$, a selection that corresponds to

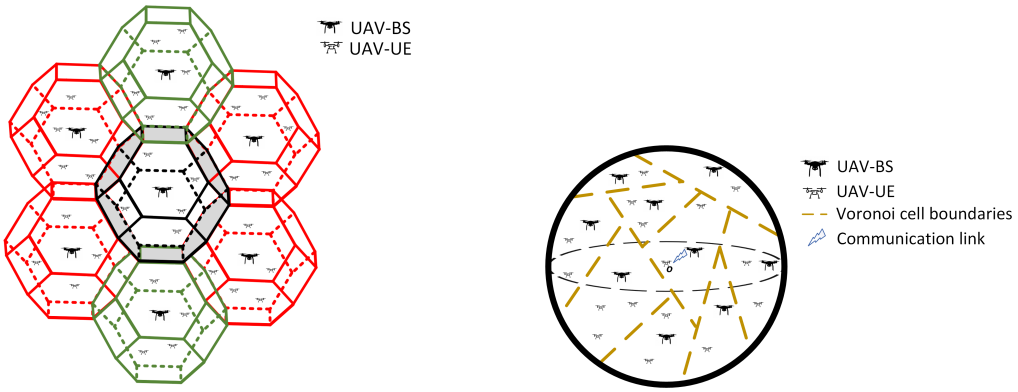

(a) The 3D cellular network with the deterministic location of the UAV-BSs at the center of truncated octahedrons and the locations of UAV-UEs modeled as a 3D PPP.

(b) The 3D cellular network modeled as a binomial-Voronoi network, where the random locations of the UAV-BSs are modeled as 3D BPP.

Figure 5.1: Illustration of the two considered network deployments depicting both UAV-BSs and UAV-UEs.

a worst-case interference scenario in which all UAV-BSs interfere with each other[1]. In this case, the 3D locations of all co-channel interfering UAV-BSs are given by (5.1). All UAV-BSs are assumed to transmit at the same power p_0, and all UAVs are equipped with an isotropic antenna. Since the UAVs are assumed to hover above rooftops, the communication links between the UAV-BSs and the UAV-UEs are considered to be in LoS condition [47]. The LoS channels are assumed to experience Nakagami-m fading [2] with different fading parameter m. Therefore, the channel power gains h_v follow a Gamma distribution, $h_v \sim \text{Gamma}\big(m_v, \frac{1}{m_v}\big)$ with the shape and scale parameters of h_v being m_v and $1/m_v$, respectively. Here, $v \in \{s, k\}$, where s denotes the link between the reference UAV-BS and the receiver, and k the link between the receiver and the i-th UAV-BS located at $\mathbf{p}_i$. The PDF of h_v is given by

$$f_{h_v}(x) = \frac{{m_v}^{m_v} x^{m_v-1}}{\Gamma(m_v)} \exp\left(-m_v x\right), \tag{5.3}$$

where $\Gamma(\cdot)$ is the Gamma function [40, eq. (8.310.1)]. Note that $\mathbb{E}[h_v] = m_v \frac{1}{m_v} = 1$. Also, the values of m_s are restricted to integers for analytical tractability. The SINR at the receiver

[1] Although the worst-case interference scenario is considered, it can be easily extended to other values of q and consider more tiers of the 3D network.

[2] As stated in [76], the most natural choice for modeling small-scale fading in UAV-assisted communications is Rician fading, which makes a clear distinction between the direct and the scattered paths. This is mainly due to the high probability of LoS links in aerial networks. However, the Rician PDF does not lend itself to further analysis since it entails the modified Bessel function. Therefore, Nakagami-m model is chosen, which is quite common in the literature thanks to its mathematical tractability. Furthermore, the Rician distribution with factor K can be well approximated with the Nakagami-m distribution using $m = \frac{(K+1)^2}{2K+1}$.

is given by

$$\text{SINR} = \frac{p_0 h_s r_n^{-\alpha}}{I + \sigma^2}, \tag{5.4}$$

where σ^2 is the additive white Gaussian noise power, and α is the path-loss exponent. Finally, I refers to the aggregate interference power and is given by $I = \sum_{i=1}^{N_c} p_0 h_i U_i^{-\alpha}$.

5.2.2 Binomial-Voronoi Network

Consider a 3D UAV network with UAV-UEs whose spatial location is modeled as a 3D PPP with intensity λ. Moreover, consider a BPP Ψ, which models the spatial locations of N UAV-BSs. In this setup, the N UAV-BS are assumed to be uniformly and independently distributed in a finite 3D ball $b_3(\mathbf{o}, D)$ centered at the origin $\mathbf{o} = [0, 0, 0]^T$ with radius D. Again, the forward link from the UAV-BSs to the UAV-UEs is considered. The wireless backhaul connectivity for the UAV-BSs is supposed to be provided by high altitude platforms (HAPs). By using the criteria of the nearest neighbor association, each UAV-UE is directly associated with the closest UAV-BS and 3D binomial-Voronoi cells are therefore formed. Without loss of generality, the UAV-UE receiver is assumed to be located at the origin o, and it is served by the nearest UAV-BS that is located in the corresponding Voronoi cell and is called the *serving UAV-BS*. A representative example of this model is depicted in Fig. 5.1b. Let r denote the Euclidean distance between the receiver and the serving UAV-BS. All other assumptions related to the communication and channel models follow the same lines as the ones presented in the previous subsection. Once the link between the receiver and the serving UAV-BS has been established, the remaining $(N-1)$ UAV-BS interfere to the receiver. Let $\{V_i\}_{i=1}^{N-1}$ denote the distance between the interfering UAV-BSs and the receiver. In this case, the SINR at the receiver is given by

$$\text{SINR} = \frac{p_0 h_s r^{-\alpha}}{I + \sigma^2}, \tag{5.5}$$

where $I = \sum_{i=1}^{N-1} p_0 h_i V_i^{-\alpha}$, is the aggregate interference.

5.2.3 Coverage Probability and Average Rate

Recalling the previous chapters, the coverage probability is defined as the probability that the SINR at the receiver, exceeds a predefined threshold γ, i.e. $\mathcal{P}_c(\gamma) \triangleq \mathbb{P}(\text{SINR} \geqslant \gamma)$. The instantaneous achievable rate of the corresponding UAV-UEs is defined as $\mathcal{R}_{inst} \triangleq B_w \log_2(1 + \text{SINR})$, where B_w is the considered bandwidth. The CDF of $\mathcal{R}_{inst}$ is defined as $\mathbb{P}[\mathcal{R}_{inst} \leq r_t]$, where r_t is the target rate. Then, the average achievable rate of the

corresponding UAV-UEs is calculated as

$$\mathcal{R} \triangleq \mathbb{E}[B_w \log_2(1+\text{SINR})]) = \frac{B_w}{\ln 2}\int_0^{\infty}\frac{\mathcal{P}_c(\gamma)}{1+\gamma}\mathrm{d}\gamma. \tag{5.6}$$

5.3 Performance Analysis

5.3.1 Coverage Probability Analysis for the Regular Network

Initially, the joint distribution of the receiver's spherical coordinates is extracted.

Lemma 5.1. *The joint PDF of the spherical coordinates of the receiver at w_n is given by*

$$f_{w_n}(r_n,\theta_n,\phi_n) = \frac{3\sin(\theta_n)}{4\pi}\frac{r_n^{3n-1}\left(\frac{4\pi\lambda}{3}\right)^n}{\Gamma(n)}\exp\Big(-\frac{4\pi\lambda r_n^3}{3}\Big). \tag{5.7}$$

Proof: See Appendix D.1. □

The Laplace transform of I is now derived as an intermediate step in the coverage probability analysis. However, the direct statistical characterization of the distance U_i is complicated. Conditioned on w_n, the distance U_i is no longer a random variable.

Lemma 5.2. *The Laplace transform of the interference power distribution conditioned on the location w_n is*

$$\mathcal{L}_I(s|w_n) = \prod_{i=1}^{N_c}\Big(1+\frac{sp_0U_i^{-\alpha}}{m_k}\Big)^{-m_k}. \tag{5.8}$$

Proof. The proof follows similar lines as the one presented in [57, Appendix E] and hence it is omitted here for brevity. □

Now, by exploiting Lemma 5.1 and Lemma 5.2, the coverage probability can now be derived.

Theorem 5.3. *The coverage probability of a receiver in the reference cell W is given by*

$$\begin{aligned}\mathcal{P}_c(\gamma) = \int_0^{\infty}\int_0^{\pi}\int_0^{2\pi}\sum_{k=0}^{m_s-1}\frac{(-1)^k}{k!}\left(\frac{m_s\gamma r_n^{\alpha}}{p_0}\right)^k\left[\frac{\partial^k\mathcal{L}_{I_{tot}}(s|w_n)}{\partial s^k}\right]_s \\ \times f_{w_n}(r_n,\theta_n,\phi)rmd\phi_n rmd\theta_n rmdr_n,\end{aligned} \tag{5.9}$$

where $s=\frac{m_s\gamma r_n^{\alpha}}{p_0}$ and $\mathcal{L}_{I_{tot}}(s|w_n) = \exp(-\sigma^2 s)\mathcal{L}_I(s|w_n)$.

Proof: See Appendix D.2. □

While the reduced analytical complexity of our framework is of great interest, an accurate approximation of Theorem 5.3 with reduced complexity is presented next.

Corollary 5.4. *The approximated coverage probability of a receiver in W is given by*

$$\mathcal{P}_c^{approx}(\gamma) \approx \int_0^{\infty}\int_0^{\pi}\int_0^{2\pi}\sum_{k=1}^{m_s}(-1)^{k+1}\binom{m_s}{k}\mathcal{L}_{I_{tot}}\left(\frac{km_s(m_s!)^{-\frac{1}{m_s}}\gamma r^{\alpha}}{p_0}\middle| w_n\right) \times f_{w_n}(r_n,\theta_n,\phi_n)\mathrm{d}\phi_n\mathrm{d}\theta_n\mathrm{d}r_n. \tag{5.10}$$

Proof. The proof builds on the lower bounds of a complementary CDF of a Gamma-distributed random variable, provided in [47]. Thus, it is omitted here. □

5.3.2 Coverage Probability Analysis for the binomial-Voronoi network

In this subsection, the Laplace transform of the aggregate interference I is first derived in closed form as intermediate step in the coverage probability analysis. The PDF of the serving distance r is obtained directly by [2] as

$$f_r(r) = 3Nr^2\frac{(D^3-r^3)^{N-1}}{D^{3N}}, 0 \leq r \leq D. \tag{5.11}$$

However, the distances $\{V_i\}_{i=1}^{N-1}$ are dependent due to the common serving distance r. Conditioned on r, the PDF of $\{V_i\}_{i=1}^{N-1}$ is derived in the following Lemma.

Lemma 5.5. *Conditioned on the serving distance r, the distances $\{V_i\}_{i=1}^{N-1}$ are i.i.d with PDF given by*

$$f_{V_i|r}(v_i) = \frac{3v_i^2}{D^3-r^3}, \quad r \leq v_i \leq D. \tag{5.12}$$

Proof. Please refer to the Appendix D.3 for the proof. Note that this is an alternate proof to the one provided in [6], as it is not based on theory of order statistics. □

The Laplace transform of I conditioned on r can now be calculated in order to derive the overall coverage probability.

Lemma 5.6. *The Laplace transform of the interference power distribution conditioned on the serving distance r is given by*

$$\mathcal{L}_I(s|r) = (\Theta(s,D) - \Theta(s,r))^{N-1}, \tag{5.13}$$

where $\Theta(\cdot,\cdot)$ *is given by*

$$\Theta(s,x) = \frac{x^3}{D^3 - r^3}\, {}_2F_1\left(-\frac{3}{a}, m_k; \frac{a-3}{a}; -\frac{sp_0x^{-a}}{m_k}\right), \tag{5.14}$$

and ${}_2F_1(\cdot)$ *denotes the Gauss hypergeometric function given in [40, eq. (9.100)].*

Proof: See Appendix D.4. □

By exploiting Lemma 5.5 and Lemma 5.6, the coverage probability of the binomial-Voronoi network can now be derived.

Theorem 5.7. *The coverage probability of the receiver in a binomial-Voronoi network is given by*

$$\mathcal{P}_c(\gamma) = \int_0^D \sum_{k=0}^{m_s-1} \left(\frac{-m_s\gamma r^\alpha}{p_0}\right)^k \frac{f_r(r)}{k!} \left[\frac{\partial^k \mathcal{L}_{I_{tot}}(s|r)}{\partial s^k}\right]_s \mathrm{d}r, \tag{5.15}$$

where $s = \frac{m_s\gamma r^\alpha}{p_0}$, $\mathcal{L}_{I_{tot}}(s|r) = \exp(-\sigma^2 s)\mathcal{L}_I(s|r)$, *and* $f_r(r)$ *is given by* (5.11).

Proof. The proof for deriving Theorem 5.7 follows similar lines as the one presented in Theorem 5.3. □

5.3.3 Average Rate Analysis

Given the expressions for the coverage probability derived in Theorems 5.3 and 5.7, the average achievable rate of the receiver in the two networks is now obtained, in a way similar to [47], as

$$\begin{aligned}\mathcal{R} &= \frac{B_w}{\ln 2}\int_0^\infty \mathcal{P}_c(e^t - 1)dt \\ &\approx \frac{B_w}{\ln 2}\sum_{k=1}^{M} \frac{\mathcal{P}_c(T_k)}{T_k+1}\frac{\pi^2 sin\left(\frac{2k-1}{2M}\pi\right)}{4M\cos^2\left(\frac{\pi}{4}\cos\left(\frac{2k-1}{2M}\pi\right)+\frac{\pi}{4}\right)},\end{aligned} \tag{5.16}$$

where M is a parameter to be adjusted for high accuracy and $T_k = \tan\left(\frac{\pi}{4}\cos\left(\frac{2k-1}{2M}\pi\right)+\frac{\pi}{4}\right)$. The approximation yields low complexity and it is based on the Gauss-Chebysev Quadrature as in [77].

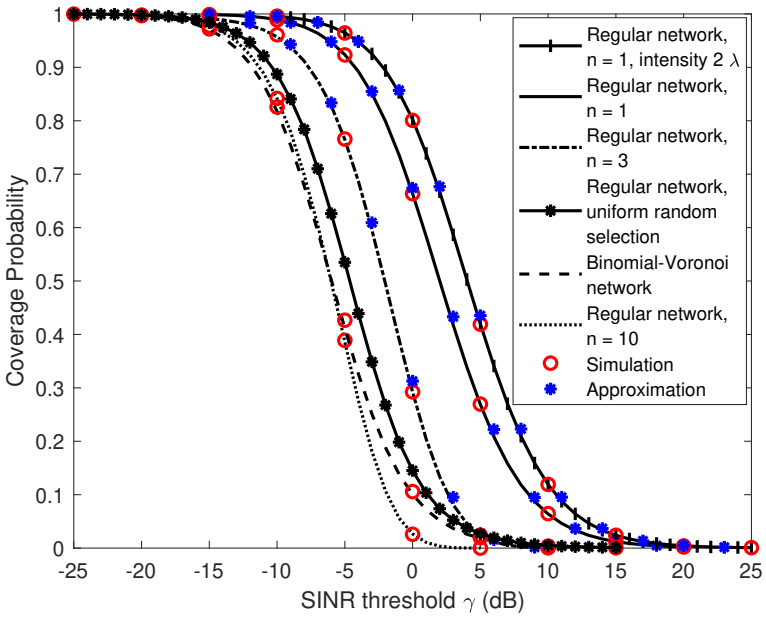

Figure 5.2: Coverage probability versus SINR threshold.

5.4 Numerical Results and Discussions

In this section, simulation and numerical results are presented to evaluate and compare the performance achieved by the two 3D cellular UAV network models. For the simulation results, unless otherwise stated, $\lambda = 10^{-5}$ UAV-UEs/m^3, $N = 15$ UAV-BSs, $R = 50$ meters, $D = 212$ meters, $p_0 = 30$ dBm, $m_v = 2$, $\alpha = 2$, and $\sigma^2 = -113$ dBm. Note that $b_3(\mathbf{o}, D)$ includes all the 15 cells of the regular network.

In Fig. 5.2, the coverage probability versus the SINR threshold is illustrated for i) a regular network with n-th nearest receiver selection policy and ii) a binomial-Voronoi network. For the former case, it is observed that as n increases, the coverage performance is significantly degraded and the curves become steepest. Also, when the deployment density of the UAV-UEs increases, the coverage performance increases, since the receiver comes closer to the reference UAV-BS. The coverage probability of the binomial-Voronoi network is also compared, via Monte-Carlo simulation, to that of a regular network with uniformly random receiver selection policy. It is interestingly observed that the performance of the binomial-Voronoi network is slightly degraded. This is because of the geometry of the regular network, where the UAV-BSs hover at the center of the cells and the receiver is not equally affected from all interfering UAV-BSs. In all cases, the simulation results verify the accuracy of Theorems 5.3 and 5.7, as well as the accuracy of the approximate expression of Corollary 5.4.

Fig. 5.3, presents the empirical, via simulation, CDF of the instantaneous spectral efficiency

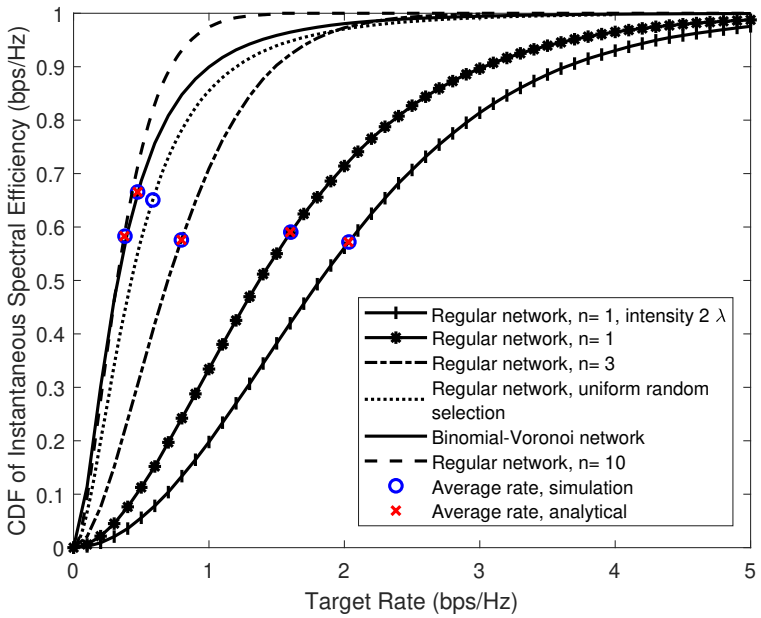

Figure 5.3: CDF of the instantaneous spectral efficiency versus target rate.

versus the instantaneous target rate. The average achievable rate for each curve is also illustrated, as evaluated both analytically using (5.16) and via simulation. Subsequently, the probability that the instantaneous spectral efficiency is below the average achievable rate is simulated. A first observation is that as n increases, the probability that the instantaneous spectral efficiency falls below a target rate, significantly increases. When the tenth nearest UAV-UE is selected as the receiver, the CDF curve is close to those of the binomial-Voronoi network and the regular network with uniformly random receiver selection policy. An interesting observation is that the right most curves preserve larger spectral efficiency but significantly increased variance. Finally, it is noticed that the average spectral efficiency of the binomial-Voronoi network and the regular network with uniformly random receiver selection policy are close. However, the probability of achieving the average value is smaller as compared to the other cases.

5.5 Chapter Summary

In this Chapter, downlink performance analysis of two 3D cellular UAV networks was conducted. Analytical and simulation results were demonstrated for a regular network with n-th nearest receiver selection policy, and a binomial-Voronoi network. Simulation results were also presented for the performance in a regular network with uniformly random receiver selection policy. The coverage performance of this network slightly outperforms the

corresponding one in a binomial-Voronoi network. The achievable average rate of the two networks is close but the probability of achieving the average rate is smaller as compared to the one in a 3D cellular network with n-th nearest receiver selection policy. Finally, it can be concluded from the analytical expressions that the binomial-Voronoi network maintains mathematical tractability and lower complexity.

Chapter 6

Conclusion and Open Research Directions

In this dissertation, various fundamental challenges related to 6G key enabling technologies, namely the mmWave and the UAV technology, were investigated. While the mathematical results derived throughout the dissertation are obviously of primary interest to wireless and stochastic geometry communities in academia, several of the design insights can be considered exploitable from the industrial community, too. For example, as far as Chapter 2 is concerned, it is clear that the theoretical framework can help in the design and the estimation of the performance of heterogeneous mmWave-enabling networks under the exploitation of realistic 3GPP-based antenna patterns. Finally, in Chapter 3, the concept of the proposed binomial 3D cellular network, can motivate the practical spatial deployment of UAV-BSs in the 3D space while on the same time ensures that minimum number of 3D cells is required.

In the following, some conclusions are drawn for the 6G enabling technologies which were investigated in this dissertation namely, the mmWave and the UAV-based technology. Potential future challenges and research directions are also presented.

6.1 Conclusions

6.1.1 Design Insights & Guidelines for mmWave Networks

Based on the insights obtained from Chapter 2 some system level insights can be drawn:

- Due to blockage and the frequent misalignment errors of the highly-directional mmWave beams, fluctuations of the channel capacity and outages are often. By recalling the analytical complexity of the 5G NR-based exhaustive scanning procedures presented in Chapter 2, it is clear that the aforementioned challenges cannot be straightforwardly solved by utilizing physical-layer functionalities. Consequently, more efficient tools, e.g. machine learning/artificial intelligence techniques can be applied to compensate the increased complexity issues.
- With the introduction of the highly directional characteristics implied by mmWave networks, the angular distances should be essentially considered in order to have i) a more

nuanced user association policy based on the 5G NR beam management procedure, and ii) a more realistic calculation of the received power.

- Considering merely the directional characteristics in the receiver's association policy severely underestimates the coverage performance. In other words, the effect of path-loss in mmWave networks has a dominant role in the cell association procedure.
- Under a single dominant interferer assumption, the coverage performance with a merely angular distance-based association policy, yields a closer approximation of the network's coverage performance under aggregate interference as compared to considering a merely Euclidean distance-based SINR metric. This trend becomes more obvious when the number of UE's sectors is small.

6.1.2 Design Insights & Guidelines for Beyond 5G 3D Cellular Networks

Based on the insights obtained from Chapters 3, 4 and the performance comparison results drawn from Chapter 5, some key system level insights can be derived:

- By considering a finite number of cellular-connected UAV-UEs in 3D cellular networks, the spherical model provides a more optimistic performance trend in terms of coverage probability, as compared to the binomial 3D cellular network. Nevertheless, although the binomial 3D cellular network can lead to full tessellation of the 3D space by deploying the minimum number of cells, the analytical complexity of the latter is particularly high and one should consider alternative 6G enabling tools such as optimization and machine learning techniques for the design and investigation of the performance of such networks.
- A binomial-Voronoi 3D network with the UAV-BSs being randomly distributed according to a 3D BPP achieves slightly higher coverage performance as compared to the regular truncated octahedron-based 3D cellular network with the locations of the UAV-BSs being well-defined and the UAV-UEs forming a 3D PPP.
- In a binomial-Voronoi 3D network, a key design parameter for determining its performance is the number of deployed UAV-BSs, which also determines the number of Voronoi cells. Increasing the number of deployed UAV-BSs will increase the received power but will also increase the interference power at the receiver. In this case, CoMP and interference coordination schemes should further be investigated.
- In a regular truncated octahedron-based 3D cellular network, the key design parameters which strongly affect its performance are the number and the size of the cells. In this case proper frequency reuse planning is necessary to reduce the interference power at the receiver. Moreover, the performance at the receiver is location-dependent and

therefore trajectory optimization schemes for finding optimal locations which maximize the performance, should be investigated. Finally, increasing the size of the cells also increases the distances between the UAV-BSs in the well-defined lattice. One technique for increasing the coverage performance at the receiver would be to involve all of the 14 neighboring UAV-BSs of the first tier of the cellular network into a CoMP scheme. The interference power from the interfering cells will then be extremely low due to the high path-loss.

6.2 Future Work

Inspired by this dissertation research, some open problems and future directions are now discussed.

The proposed generic framework for mmWave communications can serve as baseline framework for integrating further 6G key enabling technologies such as the JCAS and/or power transfer capability. However, as it has already been argued, due to the strong directivity and rapid attenuation of mmWave signals, the coverage of mmWave sensing is very limited. As RIS can reconfigure the mmWave signal direction, it can guide the mmWave signal to the originally inaccessible positions to enhance the sensing coverage. The investigation of fundamental performance limits of frameworks that combine all these 6G-related technologies are of high interest from both industry and academia.

On another front, although promising, the UAV technology comes with several open challenges and there is still a lot of research work to be done before UAVs become part of the 6G cellular network. Building on the tractable 3D stochastic geometry frameworks presented in this dissertation, several future directions can be investigated as follows.

- RIS-assisted UAV communications: A UAV equipped with RIS offers all the advantages of RIs technology while on the same time yields high flexibility die to the UAVs' capability of adjusting their position. Nevertheless, electromagnetic signal modeling and performance evaluation of such a framework is not a straightforward task.

- UAV-enabled JCAS: JCAS networks can also be utilized to monitor and manage cellular-connected UAVs, especially UAVs at low altitudes. For cellular-connected UAVs, JCAS signals emitted by ground BSs can be used for tracking the UAVs and thus enhancing the communication performance through efficient beam prediction. Since communication is generally continuously required while sensing tasks are often performed periodically specific JCAS stochastic geometry frameworks should be designed to facilitate the resource allocation and trajectory planning. Nevertheless, UAVs usually operate in swarms to execute a task which makes the design of proper mobility patterns challenging. In order to properly model the UAV mobility and traffic i) aerial corridors can be envisaged or ii) the Poisson line Cox process deployed above

the ground may be exploited to conceptualize aerial roads similar to current vehicular communication networks. Subsequently, fundamental performance limits in terms of Cramer-Rao lower bound be investigated.

- mmWave Cell-free Architectures: To overcome the complex 3D cellular structures, cell-free architectures which eliminate inter-cell interference by turning it into useful signal which mostly benefits UAVs in downlink, can be exploited. On the same time, the integration of mmWave band into cell-free architectures will increase the capacity due to highly directional 3D antennas. Stochastic geometry-based performance analysis can subsequently be conducted to reveal key design insights.

Appendices

Appendix A

Proofs of Chapter 2

A.1 Proof of Lemma 2.1

Let $W(\phi, r)$ denote a disk sector with dihedral angle ϕ and radius r. The area of the disk sector is $|W(\phi, r)| = \frac{\phi r^2}{2}$. The CCDF of ϕ_n is given by

$$\begin{aligned}\tilde{F}_{\phi_n|\mathcal{A}_{r,n}}(\phi) &= \mathbb{P}[\Phi(W) < n | \Phi(b(\mathbf{o}, r)) \geq n] \\ &= \frac{\mathbb{P}[\Phi(W) < n, \Phi(b(\mathbf{o}, r)) \geq n]}{\mathbb{P}[\Phi(b(\mathbf{o}, r)) \geq n]} \\ &= \frac{\sum_{k=0}^{n-1} P_k(\phi, r)\Big(1 - \sum_{l=0}^{n-k-1} Q_l(\phi, r)\Big)}{\sum_{k=n}^{\infty} P_k(2\pi, r)},\end{aligned} \tag{A.1}$$

where $P_k(\phi, r) = e^{-\frac{\lambda\phi r^2}{2}} \frac{(\frac{\lambda\phi r^2}{2})^k}{k!}$, $Q_l(\phi, r) = e^{-\lambda(\pi r^2 - \frac{\phi r^2}{2})} \frac{(\lambda r^2(\pi - \frac{\phi}{2}))^l}{l!}$ and $\Phi(\cdot)$ is a counting measure denoting the number of points of the point process Φ falling in an area. Now, the PDF of the conditional distance distribution is given by $f_{\phi_n|\mathcal{A}_{r,n}}(\phi) = -\frac{\mathrm{d}\tilde{F}_{\phi_n|\mathcal{A}_{r,n}}(\phi)}{\mathrm{d}\phi}$. Along similar conceptual lines as the proof presented in [46, Corollary 2.3], $f_{\phi_n|\mathcal{A}_{r,n}}(\phi)$ can be obtained as

$$f_{\phi_n|\mathcal{A}_{r,n}}(\phi) = \frac{\frac{\lambda r^2}{2} P_{n-1}(\phi, r) \sum_{k=0}^{\infty} Q_k(\phi, r)}{\sum_{k=n}^{\infty} P_k(2\pi, r)}. \tag{A.2}$$

By noticing that $\sum_{k=0}^{\infty} \frac{x^k}{k!} \triangleq e^x$, $\sum\limits_{\substack{k=n \\ n>0}}^{\infty} \frac{x^k}{k!} \triangleq \frac{e^x(\Gamma(n) - \Gamma(n,x))}{\Gamma(n)}$ and after applying some manipulations, we obtain Lemma 2.1.

A.2 Proof of Lemma 2.3

Consider the event $\mathcal{A}_{r,2}$. Following the properties of a PPP, the spatial locations of the K points in $b(\mathbf{o}, r)$ form a finite PPP and the number of points falling in $b(\mathbf{o}, r)$ follows a Poisson distribution with mean $\lambda|b(\mathbf{o}, r)|$. The set of the unordered absolute angular distances $\{|\phi_k|\}_{k=1:K}$ for the kth angular distance of kth point, is uniformly distributed on

$[0,\pi]$, i.e., $|\phi_k| \sim U[0,\pi]$. By order statistics [78], let $Z_{r,k}$ define the event that k BSs exist in $b(\mathbf{o},r)$. The joint PDF of the smallest two random variables X_1, X_2, given $Z_{r,K}$, is given by $f_{X_1,X_2}(x,y \,|\, Z_{r,K}) = K(K-1)[1-F_{X_1}(y)]^{K-2} f_{X_1}(x) f_{X_1}(y)$. Let $X_1 = |\varphi_1|$, $X_2 = |\varphi_2|$. Then, $f_{|\varphi_1|,|\varphi_2|}(|\varphi_1|,|\varphi_2| \,|\, Z_{r,K})$ is given by $f_{|\varphi_1|,|\varphi_2|}(|\varphi_1|,|\varphi_2| \,|\, Z_{r,K}) = \frac{K(K-1)}{\pi^2}\left(1-\frac{|\varphi_2|}{\pi}\right)^{K-2}$, and corresponding CDF is given by

$$\begin{aligned} &F_{|\varphi_1|,|\varphi_2|}(|\varphi_1^0|,|\varphi_2^0| \,|\, Z_{r,K}) \\ &= \int_0^{|\varphi_1^0|} \int_{|\varphi_1|}^{|\varphi_2^0|} f_{|\varphi_1|,|\varphi_2|}(|\varphi_1|,|\varphi_2||Z_{r,K})\, \mathrm{d}|\varphi_2|\, \mathrm{d}|\varphi_1| \\ &= \frac{K}{\pi^K}\Big(\frac{\pi^K - (\pi-|\varphi_1^0|)^K - K|\varphi_1^0|(\pi-|\varphi_2^0|)^{K-1}}{K}\Big). \end{aligned} \tag{A.3}$$

Then, for the PPP case over a finite region, $F_{|\varphi_1|,|\varphi_2||\mathcal{A}_{r,2}}(|\varphi_1^0|,|\varphi_2^0|)$ can be obtained as

$$F_{|\varphi_1|,|\varphi_2||\mathcal{A}_{r,2}}(|\varphi_1^0|,|\varphi_2^0|) = \frac{\mathbb{P}[|\varphi_1|<|\varphi_1^0|,|\varphi_2|<|\varphi_2^0|,\mathcal{A}_{r,2}]}{\mathbb{P}[\mathcal{A}_{r,2}]}. \tag{A.4}$$

Now, the probability that the event $\{|\varphi_1|<|\varphi_1^0|,|\varphi_2|<|\varphi_2^0|,\mathcal{A}_{r,2}\}$ occurs, can be obtained by averaging over $\mathcal{A}_{r,2}$, that is

$$\begin{aligned} &\mathbb{P}[|\varphi_1|<|\varphi_1^0|,|\varphi_2|<|\varphi_2^0|,\mathcal{A}_{r,2}] \\ &= \sum_{k=2}^{\infty} F_{|\varphi_1|,|\varphi_2|}(|\varphi_1^0|,|\varphi_2^0| \,|\, Z_{r,k}) \frac{(\lambda\pi r^2)^k}{k!} e^{-\lambda\pi r^2} \\ &= 1 - e^{-\lambda r^2|\varphi_1^0|} - \lambda r^2 |\varphi_1^0| e^{-\lambda r^2|\varphi_2^0|}. \end{aligned} \tag{A.5}$$

Next, $\mathbb{P}[\mathcal{A}_{r,2}] = 1 - \frac{\Gamma(2,\lambda\pi r^2)}{\Gamma(2)}$. By substituting in (52), $F_{|\varphi_1|,|\varphi_2||\mathcal{A}_{r,2}}(|\varphi_1^0|,|\varphi_2^0|)$ is given by

$$F_{|\varphi_1|,|\varphi_2||\mathcal{A}_{r,2}}(|\varphi_1^0|,|\varphi_2^0|) = \frac{1 - e^{-\lambda r^2|\varphi_1^0|} - \lambda r^2|\varphi_1^0| e^{-\lambda r^2|\varphi_2^0|}}{1 - \frac{\Gamma(2,\lambda\pi r^2)}{\Gamma(2)}}. \tag{A.6}$$

Finally, $f_{|\varphi_1|,|\varphi_2||\mathcal{A}_{r,2}}(|\varphi_1|,|\varphi_2|)$ can be obtained after differentiating (A.6) w.r.t $|\varphi_1^0|,|\varphi_2^0|$ as $f_{|\varphi_1|,|\varphi_2||\mathcal{A}_{r,2}}(|\varphi_1|,|\varphi_2|) = \frac{\partial^2 F_{|\varphi_1|,|\varphi_2||\mathcal{A}_{r,2}}(|\varphi_1^0|,|\varphi_2^0|)}{\partial|\varphi_1^0|\partial|\varphi_2^0|}$, which directly results to Lemma 2.3.

A.3 Proof of Lemma 2.4

The PDF of S_x is first derived. Since $\varphi_r \sim U[0, \frac{\phi_{3dB}}{2}]$, $g(\varphi^x) = 10^{\frac{G_{max}-12\left(\frac{\varphi^x}{\phi_{3dB}}\right)^2}{10}}$. Then, $g(\varphi^x)$ is a function of the random variable φ^x. Building on φ^x and applying successive change of

variables, the PDF $f_{g(\varphi^x)}(g)$ is given by $f_{g(\varphi^x)}(g) = \frac{1}{ln(10)x}\frac{10}{12\sqrt{\frac{Gmax-10log(x)}{12}}}, \quad x \in [g_{3dB}, g_{max}]$. Subsequently, the PDF of $r_x^{-\alpha_L}$ is expressed in terms of the corresponding CDF as

$$\begin{aligned}\mathbb{P}[r_x^{-\alpha_L} \leq x] &= \mathbb{P}\Big[r_x^{\alpha_L} \geq \frac{1}{x}\Big] = 1 - \mathbb{P}\Big[r_x \leq \Big(\frac{1}{x}\Big)^{\frac{1}{\alpha_L}}\Big] \\ &= 1 - F_{r_x}\Big(\Big(\frac{1}{x}\Big)^{\frac{1}{\alpha_L}}\Big), \quad F_{r_x}(r) = \frac{r^2}{R_L^2}.\end{aligned} \tag{A.7}$$

Now, $f_{r_x^{-\alpha_L}}(x)$ is obtained after differentiating (A.7) w.r.t the appropriate range of x, that is, $f_{r_x^{-\alpha_L}}(x) = \frac{2\left(\frac{1}{x}\right)^{\frac{\alpha_L+2}{\alpha_L}}}{\alpha_L R_L^2}, x \in [R_L^{-\alpha_L}, \infty)$. The PDF and the CDF of S_x can now be written as

$$f_{S_x}(w) = \int_{g_{3dB}}^{\psi(w)} \frac{1}{x} f_{g(\varphi^x)}(x) f_{r_x^{-\alpha_L}}\Big(\frac{w}{x}\Big)\mathrm{d}x, \tag{A.8}$$

$$F_{S_x}(w_0) = \int_{g_{3dB}R_L^{-\alpha_L}}^{w_0} \int_{g_{3dB}}^{\psi(w)} \frac{1}{x} f_{g(\varphi^x)}(x) f_{r_x^{-\alpha_L}}\Big(\frac{w}{x}\Big)\mathrm{d}x\mathrm{d}w, \tag{A.9}$$

The PDF of $S = \max_{x\in(\Psi_{bs}\cap b(\mathbf{o},R_L))}\{S_x\}$ can now be obtained by exploiting results from Order Statistics [78]. However, S is meaningfully defined conditioned on $\mathcal{A}_{R_L,1}$. Accordingly, let $Z_{R_L,k}$, with $k \geq 1$, define the event that k BSs exist in $b(\mathbf{o}, R_L)$. Then, from the definition of $\Psi_{bs} \cap b(\mathbf{o}, R_L)$, $\mathbb{P}[\mathcal{A}_{R_L,k}] = e^{-\lambda_{bs}\pi R_L^2}(\lambda_{bs}\pi R_L^2)^k/k!$. Given $Z_{R_L,k}$ and since the elements of S_x are i.i.d., the probability that $S \leq s_0$ is given by $\mathbb{P}[S \leq s_0|Z_{R_L,k}] = F_S(s_0|Z_{R_L,k}) = (F_{S_x}(w))^k$. Now, in a similar vein to the proof presented in Appendix A, $F_{S|\mathcal{A}_{R_L,1}}(s_0)$ can be obtained as $F_{S|\mathcal{A}_{R_L,1}}(s_0) = \frac{\mathbb{P}[S\leq s_0, \mathcal{A}_{R_L,1}]}{\mathbb{P}[\mathcal{A}_{R_L,1}]}$. Accordingly, $\mathbb{P}[S \leq s_0, \mathcal{A}_{R_L,1}]$ can be derived by averaging $\mathbb{P}[S \leq s_0|\mathcal{A}_{R_L,k}]$ over $\mathcal{A}_{R_L,k}$, that is

$$\begin{aligned}&\mathbb{P}[S \leq s_0, \mathcal{A}_{R_L,1}] \\ &\overset{(a)}{=} \sum_{k=1}^{\infty} (F_{S_x}(w))^k e^{-\lambda_{bs}\pi R_L^2} \frac{(\lambda_{bs}\pi R_L^2)^k}{k!} \\ &\overset{(b)}{=} e^{\lambda_{bs}\pi R_L^2\left(1-F_{S_x}(s_0)\right)} - e^{-\lambda_{bs}\pi R_L^2}, \quad s_0 \in [w_{min}, \infty),\end{aligned} \tag{A.10}$$

where (a) follows after averaging over k and (b) follows from $\sum_{k=1}^{\infty}\frac{a^k b^k}{k!} \overset{\triangle}{=} e^{ab} - 1$. Next, $\mathbb{P}[\mathcal{A}_{R_L,1}] = 1 - e^{-\lambda\pi R_L^2}$. By substituting all the above in the definition of $F_{S|\mathcal{A}_{R_L,1}}(s_0)$, $F_{S|\mathcal{A}_{R_L,1}}(s_0)$ yields. Finally, the PDF $f_{S|\mathcal{A}_{R_L,1}}(s_0)$ is obtained directly as $f_{S|\mathcal{A}_{R_L,1}}(s_0) = \frac{dF_{S|\mathcal{A}_{R_L,1}}(s_0)}{ds_0} = \frac{\lambda_{bs}\pi R_L^2 f_{S_x}(s_0) e^{\lambda_{bs}\pi R_L^2\left(F_{S_x}(s_0)-1\right)}}{1-e^{-\lambda\pi R_L^2}}$.

A.4 Proof of Lemma 2.6

Conditioned on $S = g(\varphi_r)r_s^{-\alpha_L}$, the location x_0 of the serving BS and the maxima ϕ_0^r of the receiving beam are known. Once the serving BS has been determined, by appealing to Slivnyak's Theorem, $\Psi_{bs}^!$ is a HPPP restricted to the set $\{\boldsymbol{\Omega} \cup \boldsymbol{\Omega}'\}$. The set $\{\boldsymbol{\Omega} \cup \boldsymbol{\Omega}'\}$ is defined by all possible locations of the interfering BSs, being those locations which lie outside the exclusion zone. Note that the exclusion zone is defined by all possible locations of x_0. However, the location x_0, given through φ_r, r_s, is a function of the maximum received power S_{th}. In Fig. A.1a, a representative powersurface example of the maximum received power S from x_0 in terms of φ_r and r_s, is illustrated, by assuming a 4-sectored antenna, i.e, $\phi_{3dB} = \pi/2$. In Fig. 3b, the corresponding powersurface of the received power $S_x = g(|\phi_0^r - \phi_x|)r_x^{-\alpha_L}$ from $x \in (\Psi_{bs} \cap \boldsymbol{b}(\boldsymbol{o}, R_L))$ in terms of r_x, ϕ_x, is shown, by assuming that the third beam has been chosen as the receiving beam and therefore $\phi_0^r = \pi/4 + \pi/2 + \pi/2$. Notice that for a given value of $S = S_{th}$ in Fig. A.1a, the received power from the interfering BSs should be smaller than S_{th} and the locations of $x \in \Psi_{bs}^!$ must lie outside the exclusion zone indicated by the yellow markers. Also, notice that in Fig. A.1b, S_{th} indicates the maximum received power of an interfering BS. Considering the aforementioned, the minimum distance r_x^{min} is given by

$$\begin{aligned} & g_{3gpp}(|\phi_0^r - \phi_x|)r_x^{min\,-\alpha_L} < \underbrace{g(\varphi_r)r_s^{-\alpha_L}}_{S_{th}} \\ \Leftrightarrow\ & \frac{g_{3gpp}(|\phi_0^r - \phi_x|)}{S_{th}} < r_x^{min\,-\alpha_L} \\ \Leftrightarrow\ & r_x^{min} > \left(\frac{g_{3gpp}(|\phi_0^r - \phi_x|)}{S_{th}}\right)^{\frac{1}{\alpha_L}}, \end{aligned} \tag{A.11}$$

as $\phi_x \in [0, 2\pi]$. Now, by observing from Fig. 3b that $r_x > R_L$ for some values of S, r_x^{min} is rewritten as $r_x^{min} = \min\left\{\left(\frac{g_{3gpp}(|\phi_0^r - \phi_x|)}{S_{th}}\right)^{\frac{1}{\alpha_L}}, R_L\right\}$. Now, along similar conceptual lines, r_x^{max} can be derived. Next, the Laplace transform of I conditioned on S and ϕ_0^r is given by

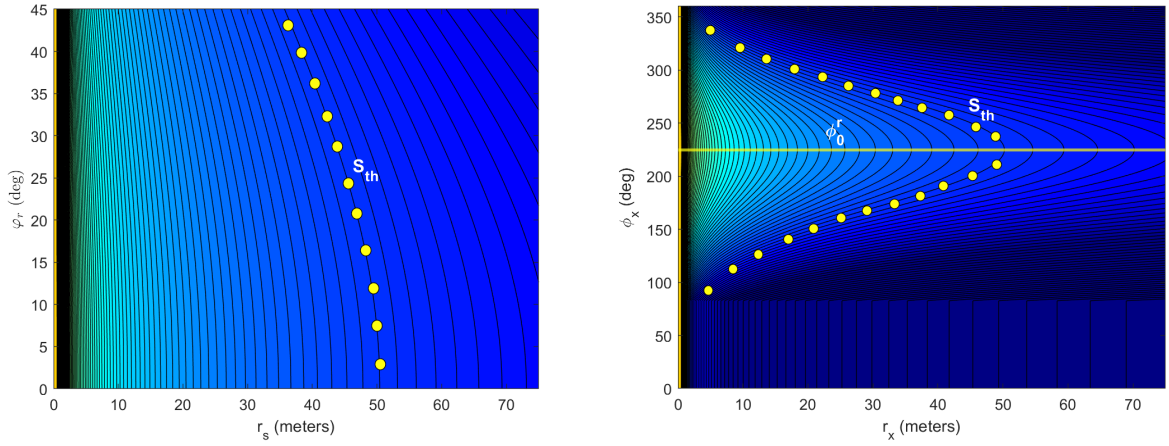

(a) Powersurface of maximum received power S, versus r_s and φ_r.

(b) Powersurface of received power $S_x = g(|\phi_0^r - \phi_x|)r_x^{-\alpha_L}$, versus r_x and ϕ_x.

Figure A.1: Representative example of powersurfaces for the serving and interfering BSs corresponding to a receiver equipped with a 4-sectored antenna, $\phi_0^r = \pi/4 + \pi/2 + \pi/2$ and $S = S_{th}$.

$$
\begin{aligned}
\mathcal{L}_I(s|S_{th},\phi_0^r) &= \mathbb{E}_{\Psi_{bs}^!}\left[e^{-sI}\right] = \mathbb{E}_{\Psi_{bs}^!}\left[e^{-s\sum_{x\in\Psi_{bs}^!} ph_x g_{max} g_{3gpp}(|\phi_0^r-\phi_x|)l(\|x\|)}\middle| S_{th},\phi_0^r\right] \\
&\overset{(a)}{=} \mathbb{E}_{\Psi_{bs}^!}\left[\prod_{x\in\Psi_{bs}^!}\left(1+\frac{s\,p\,g_{max}\,g_{3gpp}(|\phi_0^r-\phi_x|)l(\|x\|)}{m_x}\right)^{-m_x}\middle| S_{th},\phi_0^r\right] \\
&\overset{(b)}{=} \exp\left(-\lambda_{bs}\iint_{\mathbf{\Omega}}\left(1-\left(1+\frac{s\,p\,g_{max}\,g_{3gpp}(|\phi_0^r-\phi_x|)\,K r_x^{-\alpha_L}}{m_x}\right)^{-m_x}\right) r_x \mathrm{d}\phi_x \mathrm{d}r_x\right) \\
&\times \exp\left(-\lambda_{bs}\iint_{\mathbf{\Omega}'}\left(1-\left(1+\frac{s\,p\,g_{max}\,g_{3gpp}(|\phi_0^r-\phi_x|)\,K r_x^{-\alpha_N}}{m_x}\right)^{-m_x}\right) r_x \mathrm{d}\phi_x \mathrm{d}r_x\right) \\
&\overset{(c)}{=} \exp\left(-\lambda_{bs}\int_{r_x^{min}}^{R_L}\int_0^{2\pi}\left(1-\left(1+\frac{s\,p\,g_{max}\,g_{3gpp}(|\phi_0^r-\phi_x|)K r_x^{-\alpha_L}}{m_x}\right)^{-m_x}\right) r_x \mathrm{d}\phi_x \mathrm{d}r_x\right) \\
&\times \exp\left(-\lambda_{bs}\int_{R_L}^{r_x^{max}}\int_0^{2\pi}\left(1-\left(1+\frac{s\,p\,g_{max}\,g_{3gpp}(|\phi_0^r-\phi_x|)K r_x^{-\alpha_N}}{m_x}\right)^{-m_x}\right) r_x \mathrm{d}\phi_x \mathrm{d}r_x,\right.
\end{aligned}
\tag{A.12}
$$

where (a) follows from the MGF of h_x, (b) follows from the PGFL of the PPP and from independence between the locations of LOS and NLOS interfering BSs, and (c) follows from integration over the set of the region $\mathbf{\Omega}$ and $\mathbf{\Omega}'$.

A.5 Proof of Theorem 2.7

The conditional coverage probability is first given by

$$\begin{aligned}\mathcal{P}_c(\gamma) &= \mathbb{P}\Big[\frac{p\,h_s\,g_{max}\,g(\varphi_r)\,l(\|x_0\|)}{I+\sigma^2} > \gamma \Big| r_s, \phi_s, \phi_0^r\Big] = \mathbb{P}\Big[\frac{p\,h_s\,g_{max}\,K\,S_{th}}{I+\sigma^2} > \gamma \Big| S_{th}, \phi_0^r\Big] \\ &= \mathbb{P}\Big[h_s > \frac{\gamma(I+\sigma^2)}{p\,g_{max}\,K\,S_{th}} \Big| S_{th}, \phi_0^r\Big] \\ &\overset{(a)}{=} \sum_{k=0}^{m_s-1} \frac{(-s)^k}{k!}\left[\frac{\partial^k \mathcal{L}_{I_{tot}}(s|S_{th},\phi_0^r)}{\partial s^k}\right]_s \\ &\overset{(b)}{=} \sum_{i=1}^{2^m}\sum_{k=0}^{m_s-1}\int_{w_{min}}^{\infty} \frac{(-s)^k}{k!}\left[\frac{\partial^k \mathcal{L}_{I_{tot}}(s|S_{th},\phi_0^i)}{\partial s^k}\right]_s f_S(S_{th}) p_\phi \mathrm{d}S_{th},\end{aligned} \tag{A.13}$$

where (a) follows from the CCDF of h_s, the definition of incomplete gamma function for integer values of m_s and by using $\mathbb{E}_{I_{tot}}[\exp(-sI_{tot})(sI_{tot})^k] = (-s)^k \frac{\partial^k \mathcal{L}_{I_{tot}}(s)}{\partial s^k}$, and (b) follows from deconditioning over the maximum power S and all possible receiving beam's maxima ϕ_0^r, with the PDF $f_S(s_0)$ and the pmf p_ϕ, respectively.

A.6 Proof of Lemma 2.9

Through manipulation of Corollary 2.2, let $r = R_L$, $\lambda = \lambda_{bs}$, $\phi = 2^{m+1}\varphi_c$, $n = 1$ and $\varphi_c \in [0, \frac{\pi}{2^m}]$ so that $\phi \in [0, 2\pi]$. Then, $W(\phi, r) = \frac{\phi r^2}{2} = 2^m \varphi_c R_L^2$. Next, the proof follows the same steps as the proof for deriving Lemma 2.1.

A.7 Proof of Lemma 2.10

As the distance of x_0 is independent of the association scheme, the locations of $x \in \Psi_{bs}^!$ can be anywhere in angular distance larger than the serving angular distance φ_c, and therefore let $\mathbf{V} = \{(r_x, \phi_x) \in \mathbb{R}^2 | 0 \le r_x \le R_L,\ \varphi_c \le \phi_x \le 2\pi\}$. Then, the proof follows the same steps shown in Appendix A.4 and hence it is omitted here.

A.8 Proof of Theorem 2.11

Similar to the proof for deriving Theorem 2.7,

$$\begin{aligned}\mathcal{P}_c(\gamma) &= \mathbb{P}\Big[\frac{p\,h_s\,g_{max}\,g(\varphi_c)\,l(\|x_0\|)}{I+\sigma^2} > \gamma \Big| \varphi_c, \phi_0^r, d_0\Big] \\ &\overset{(a)}{=} \sum_{i=1}^{2^m}\sum_{k=0}^{m_s-1}\int_0^{\frac{\pi}{2^m}}\int_0^{R_L}\frac{(-s)^k}{k!}\left[\frac{\partial^k \mathcal{L}_{I_{tot}}(s|\varphi_c,\phi_0^i)}{\partial s^k}\right]_s p_\phi f_{d_0}(d_0) f_{\varphi_c|\mathcal{A}_{R_L,1}}(\varphi_c)\mathrm{d}d_0\mathrm{d}\varphi_c,\end{aligned} \tag{A.14}$$

where (a) follows from deconditioning over the conditioned random variables φ_c, ϕ_0^r, d_0 of the conditional coverage probability.

A.9 Proof of Lemma 2.14

By exploiting theory of Order Statistics [78], and given that k BSs ($k \geq 2$) exist in $b(\mathbf{o}, R_L)$, the joint PDF is first given by

$$f_{Pr_0,Pr_I|k}(s_0, s_I) = k(k-1)(F_{S_x}(s_0)^{k-2} f_{S_x}(s_0) f_{S_x}(s_I). \tag{A.15}$$

Then, $f_{Pr_0,Pr_I|\mathcal{A}_{R_L,2}}(s_0, s_I)$ can be obtained along similar lines as the proof presented in Appendix A.2 and thus it is omitted here.

A.10 Proof of Proposition 2.17

The PDF of the SIR results directly from expressing the SIR given as a product of two random variables

$$f_{SIR}(x) = \int_1^\infty \frac{1}{x} f_{P|\mathcal{A}_{R_L,2}}(x) f_{Q||\mathcal{A}_{R_L,2}}(\frac{x}{p_0})\mathrm{d}p_0. \tag{A.16}$$

Then, $F_{SIR}(\gamma) = \int_0^\gamma f_{SIR}(x)\mathrm{d}x$.

A.11 Proof of Lemma 2.18

Since $|\varphi_1|, |\varphi_2|$ are dependent and conditioned on $T_{\phi_A,2}$, the PDF $f_{|\varphi_1|,|\varphi_2||T_{\phi_A,2}}(|\varphi_1|, |\varphi_2|)$ of $|\varphi_1|, |\varphi_2|$ is given as

$$f_{|\varphi_1|,|\varphi_2||T_{\phi_A,2}}(|\varphi_1|, |\varphi_2|) = \frac{1}{\mathbb{P}[T_{\phi_A,2}]}\frac{\partial^2 F_{|\varphi_1|,|\varphi_2||T_{\phi_A,2}}(|\varphi_1^0|, |\varphi_2^0|)}{\partial|\varphi_1^0|\partial|\varphi_2^0|}, \tag{A.17}$$

where $F_{|\varphi_1|,|\varphi_2||T_{\phi_A,2}}(|\varphi_1^0|,|\varphi_2^0|)$ is obtained through (A.6) for $|\varphi_1^0|<\phi_A, |\varphi_2^0|<\phi_A$ and $\mathbb{P}[T_{\phi_A,2}] = \frac{1-e^{-\lambda R_L^2\phi_A}-\lambda R_L^2\phi_A e^{-\lambda R_L^2\phi_A}}{1-\frac{\Gamma(2,\lambda\pi R_L^2)}{\Gamma(2)}}$. Presenting (A.17) through Lemma 2.3,

$$\begin{aligned} f_{|\varphi_1|,|\varphi_2||T_{\phi_A,2}}(|\varphi_1|,|\varphi_2|) &= \frac{f_{|\varphi_1|,|\varphi_2|}(|\varphi_1|,|\varphi_2|,T_{\phi_A,2})}{\mathbb{P}[T_{\phi_A,2}]} \\ &= \frac{(\lambda_{bs}R_L^2)^2 e^{-\lambda_{bs}R_L^2(|\varphi_2|-\pi)}}{e^{\lambda_{bs}\pi R_L^2}-\lambda_{bs}R_L^2\phi_A e^{\lambda_{bs}R_L^2(\pi-\phi_A)}-e^{\lambda_{bs}R_L^2(\pi-\phi_A)}}, \end{aligned} \tag{A.18}$$

for $|\varphi_1|\in[0,\phi_A]$ and $|\varphi_2|\in[|\varphi_1|,\phi_A]$. Now, notice that $g(|\varphi_1|), g(|\varphi_2|)$ are functions of a random variable, i.e., $g(|\varphi_i|) = g_{max}10^{-\frac{10}{3}\left(\frac{2|\varphi_i|}{\phi_{3dB}}\right)^2}$, $i\in\{1,2\}$. Building on $|\varphi_1|, |\varphi_2|$ and applying successive change of variables and simplifications, the joint PDF $f_{g(|\varphi_1|),g(|\varphi_2|)|T_{\phi_A,2}}(g_1,g_2)$ is

$$\begin{aligned} &f_{g(|\varphi_1|),g(|\varphi_2||T_{\phi_A,2})}(g_1,g_2) \\ &= \frac{5\,(\lambda_{bs}R_L^2\phi_{3dB})^2}{24\;g_1\,g_2}\frac{\sqrt{\log_{10}(\frac{g_{max}}{g_2})\log_{10}(\frac{g_{max}}{g_1})}}{\ln(\frac{g_{max}}{g_2})\ln(\frac{g_{max}}{g_1})}\frac{\exp\left(\lambda_{bs}R_L^2\phi_{3dB}\sqrt{10\log_{10}(g_{max}/g_2)}/(2\sqrt{3})\right)}{1-e^{-\lambda_{bs}R_L^2\phi_A}-\lambda_{bs}R_L^2\phi_A e^{-\lambda_{bs}R_L^2\phi_A}}, \end{aligned} \tag{A.19}$$

for $g(|\varphi_1|)\in[g_s,g_{max}]$ and $g(|\varphi_2|)\in[g_s,g(|\varphi_1|)]$. Let $g(|\varphi_1|)=g_1$ and $g(|\varphi_2|)=g_2$. Through $G=\frac{g_1}{g_2}$, it comes that $g_1 = Gg_2$, where $g_s\le g_1\le g_{max}$. Therefore, $g_2\in[g_s, g_{max}/z]$. Then, the PDF of G can be expressed as $f_{G|T_{\phi_A,2}}(g) = \int_{g_s}^{\frac{g_{max}}{g}} g_2\, f_{g(|\varphi_1|),g(|\varphi_2|)|T_{\phi_A,2}}(g\,g_2,g_2)\,\mathrm{d}g_2$, for $g\in[1,g_{max}/g_s]$. After some simplifications Lemma 2.18 yields.

A.12 Proof of Lemma 2.19

The PDF of $W_i = h_i r_i^{-\alpha_L}$, $i\in\{1,2\}$ is given by

$$\begin{aligned} f_{W_i}(w_i) &= \int_{R_L^{-\alpha_L}}^{\infty}\frac{1}{y}f_{d_i^{-\alpha_L}}(y)f_{h_i}(w_i/y)\mathrm{d}y \\ &= \frac{2m_u^{-\frac{2}{\alpha_L}}w_i^{-\frac{2}{\alpha_L}-1}\left[\Gamma\left(\frac{2}{\alpha_L}+m_u\right)-\Gamma\left(\frac{2}{\alpha_L}+m_u,\frac{m_u w_i}{R_L^{-\alpha_L}}\right)\right]}{\alpha_L R_L^2\Gamma(m_u)}. \end{aligned} \tag{A.20}$$

By setting $W_1 = WW_2$, the PDF of W is given by

$$f_{W||\mathcal{A}_{R_L,2}}(w) = \int_0^{\infty} w_2 f_{W_1}(w\,w_2)f_{W_2}(w_2)\mathrm{d}w_2. \tag{A.21}$$

After applying some simplifications, Lemma 2.19 yields.

A.13 Proof of Proposition 2.20

First, recall that $T_{\phi_A,2} \subseteq \mathcal{A}_{R_L,2}$, which means that $f_{G|\mathcal{A}_{R_L,2},T_{\phi_A,2}}(g) = f_{G|T_{\phi_A,2}}(g)$.Second, it is easy to argue in this setting that W is conditionally independent of $T_{\phi_A,2}$ when conditioned on $\mathcal{A}_{R_L,2}$. Therefore, the PDF of the SIR results directly from expressing the SIR given as a product of two random variables

$$f_{SIR}(x) = \int_1^{\frac{g_{max}}{g_s}} \frac{1}{g} f_{W|\mathcal{A}_{R_L,2}}(x/g) f_{G|T_{\phi_A,2}}(g) \mathrm{d}g. \tag{A.22}$$

Then, $F_{SIR}(\gamma) = \int_0^{\gamma} f_{SIR}(x)\mathrm{d}x$.

A.14 Proof of Lemma 2.21

The PDF $f_{g(|\varphi_2|)}(g_2)$ is given by

$$f_{g(|\varphi_2|)}(g_2) = \frac{5\sqrt{3}\,\phi_{3dB}}{6\sqrt{10}\ln(10)\phi_A\, g\sqrt{\log_{10}(g_{max}/g)}}, \tag{A.23}$$

$g \in [g_s, g_{max}]$. Then, $f_{G|\mathcal{A}_{R_L,2}}(g)$ can be obtained by following similar steps with the proof for Lemma 2.19.

A.15 Proof of Lemma 2.22

The joint PDF of $f_{r_1,r_2|\mathcal{A}_{R_L,2}}(r_1, r_2)$ is first derived. By exploiting theory of order statistics and following similar procedure as in Appendix A.1, the joint PDF of $f_{r_1,r_2|\mathcal{A}_{R_L,2}}(r_1, r_2)$ is given by

$$f_{r_1,r_2|\mathcal{A}_{R_L,2}}(r_1, r_2) = \frac{4(\pi\lambda_{bs})^2 r_1 r_2 e^{-\lambda_{bs}\pi r_2^2}}{1 - \frac{\Gamma(2,\lambda_{bs}\pi R_L^2)}{\Gamma(2)}}, \tag{A.24}$$

for $r_1 \in [0, R_L], r_2 \in [r_1, R_L]$. Then, the PDF of W is obtained by first obtaining the PDF of $v = r_1/r_2$ through the formula for the PDF of the ratio of two dependent random variables and then through the transformation $W = v^{-\alpha_L}$.

A.16 Proof of Lemma 2.24

The PDF $f_{|\phi_1|}(|\phi_1|, |\phi_1| < \phi_A)$ can be obtained from [38] w.r.t the range of $|\phi_1|$ when $|\phi_1| < \phi_A$ as

$$f_{|\phi_1|}(|\phi_1|, |\phi_1| < \phi_A) = \frac{N}{\pi^N}(\pi - |\phi_1|)^{N-1}, \tag{A.25}$$

$|\phi_1| \in [0, \phi_A]$. In this case, notice that $g(|\phi_1|, |\phi_1| < \phi_A)$ is a function of a random variable, i.e.,

$$g(|\phi_1|, |\phi_1| < \phi_A) = g_{max} 10^{-\frac{10}{3}\left(\frac{2|\phi_1|}{\phi_{3dB}}\right)^2}, \tag{A.26}$$

Building on $|\phi_1|$ and applying successive change of variables, the PDF $f(g, |\phi_1| < \phi_A)$ is obtained directly as in (2.47), for $g \in \left[\frac{g_{max}}{10^{\frac{3}{10}\left(\frac{2\phi_A}{\phi_{3dB}}\right)^2}}, g_{max}\right] = [g_s, g_{max}]$. Now, $F(g||\phi_1| < \phi_A)$ is first obtained as the ratio of the joint CDF of (2.47), to the probability that the event $|\phi_1| < \phi_A$ occurs,

$$\begin{aligned} F(g||\phi_1| < \phi_A) &= \frac{F_g(g, |\phi_1| < \phi_A)}{F_{|\phi_1|}(|\phi_A|)} \\ &= \frac{F_{g_{3gpp}}(g, |\phi_1| < \phi_A)}{p_{|\phi_1|<\phi_A}}, \end{aligned} \tag{A.27}$$

where $F_{|\phi_1|}(|\phi_A|) = p_{|\phi_1|<\phi_A} = 1 - \pi^{-N}(\pi - \phi_A)^N$ is obtained directly from the CDF of (A.25). After differentiating (A.27), Lemma 2.24 yields and this completes the proof.

A.17 Proof of Proposition 2.25

By setting $g(|\phi_1||\phi_1| < \phi_A) = g_{rx}(|\phi_1|)$ for convenience, the coverage probability is given through its definition as

$$\begin{aligned} \mathcal{P}_c(\gamma) &= \mathbb{E}\left[\mathbb{P}\left(\frac{c_{bs}\, g_{max}\, r_1^{-\alpha_L}}{c_{bs}\, g_{rx}(|\phi_1|)\, r_2^{-\alpha_L} + \sigma^2} > \gamma\right)\right] \\ &= \mathbb{E}\left[\mathbb{P}\left(g_{rx}(|\phi_1|) < \frac{c_{bs}\, g_{max}\, r_1^{-\alpha_L} - \gamma\, \sigma^2}{c_{bs}\, \gamma\, r_2^{-\alpha_L}}\right)\right] \\ &\overset{(a)}{=} \mathbb{E}\left[F(g_0(r_1, r_2, \gamma, \sigma^2), |\phi_1| < \phi_A)\right] \\ &\overset{(b)}{=} \int_{g_s}^{g_0(r_1,r_2,\gamma,\sigma^2)} \int_{r_1}^{R_L} \int_{0}^{R_L} f_{r_1,r_2}(r_1, r_2) f(g, |\phi_1| < \phi_A) \mathrm{d}r_1 \mathrm{d}r_2 \mathrm{d}g, \end{aligned} \tag{A.28}$$

where (a) is derived through the CDF of (2.46), obtained through integration and by considering the independence between the gains and the distances r_1, r_2, and (b) is obtained after applying the expectation w.r.t the appropriate range of g. By order statistics [78], the joint PDF $f_{r_1,r_2}(r_1, r_2)$ of r_1, r_2, is provided in Proposition 2.25 and this completes the proof.

A.18 Proof of Lemma 2.26

The PDF of d_i is given by [10] $f_{d_i}(d_i|r_1) = \frac{2d_i}{R_L^2 - r_1^2}$. Then, the PDF of $d_i^{-\alpha_L}$ is given in terms of the corresponding CDF as

$$\begin{aligned} &\mathbb{P}(d_i^{-\alpha_L} \leq d|r_1) = \mathbb{P}\Big(d_i^{\alpha_L} \geq \frac{1}{d}\Big) = 1 - \mathbb{P}\Big(d_i \leq \Big(\frac{1}{d}\Big)^{\alpha_L}\Big) \\ &= 1 - F_{d_i}\Big(\Big(\frac{1}{d}\Big)^{\alpha_L}\Big), \quad F_{d_i}(d_i) = \frac{d_i^2}{R_L^2 - r_1^2}. \end{aligned} \tag{A.29}$$

Now, $f_{d_i^{-\alpha_L}}(d|r_1)$ is obtained after differentiating (A.29) w.r.t the appropriate range of d, i.e., $d \in [R_L^{-\alpha_L}, r_1^{-\alpha_L}]$. The final PDF $f_P(x||\phi_1| < \phi_A, r_1)$ of P can now be obtained directly from the well-known formula for the PDF of the product of two independent random variables [79], w.r.t the appropriate range for the dummy variable y. The proof is now complete.

A.19 Proof of Lemma 2.28

The Laplace transform of the interference power distribution conditioned on r_1 is given by

$$\begin{aligned} &\mathcal{L}_I(s|r_1) = \mathbb{E}_I[\exp(-sI)] \\ &\overset{(a)}{=} \mathbb{E}_{h_i}\Big[\mathbb{E}_{U_i}\Big[\mathbb{E}_{|\varphi_i|}\Big[e^{-s\sum_{i=1}^{N-1} p_0 h_i g_{max} g_{3gpp}(|\varphi_i|) K U_i^{-\alpha_L}}\Big|r_1\Big]\Big]\Big] \\ &\overset{(b)}{=} \left(\mathbb{E}_{U_i}\left[\mathbb{E}_{|\varphi_i|}\left[\left(1 + \frac{s\, c_{bs}\, g_{3gpp}(|\varphi_i|)\, u_i^{-\alpha_L}}{m_I}\right)^{-m_I}\middle|r_1\right]\right]\right)^{N-1}, \end{aligned} \tag{A.30}$$

where (a) follows from the independence between $h_i, U_i, |\varphi_i|$ and (b) follows from the MGF of h_i and the conditionally independent and i.i.d. $U_i, |\varphi_i|$. By applying the definition of expectation and using the conditional PDF [10] $f_{U_i}(u_i|r_1) = \frac{2u_i}{R_L^2 - r_1^2}$ and $f_{|\varphi_i|}(|\varphi_i|) = \frac{1}{\pi}$, Lemma 2.28 yields and this completes the proof.

Appendix B

Proofs of Chapter 3

B.1 Proof of Lemma 3.3

B.1.1 Truncated Octahedron Geometry

Without loss of generality, it is assumed that the truncated octahedron W of edge length R is centered at the origin $\mathbf{o}$ of the 3D Cartesian coordinate system with the z-axis passing through the centroid of one hexagonal face of W. According to the geometrical characteristics of W [**?**], the inner radius R_{hex} of W is given by $R_{hex} = R\sqrt{\frac{3}{2}}$, while the outer radius R_{sq} is given by $R_{sq} = R\sqrt{2}$. The inner and the outer radius of W touch the hexagonal and square faces of W, respectively. The circumscribed radius R_c of W is given by $R_c = R\sqrt{\frac{5}{2}}$ and touches all the 24 vertices of W. Note that the aforementioned parameters are shown in Fig. B.1. The overall volume of W is given by $|W| = 8\sqrt{2}R^3$.

B.1.2 Evaluation of $O(\mathbf{o}, r)$

The evaluation of the volume $O(\mathbf{o}, r)$ requires the computation of the overlap region between a 3D ball $b_3(\mathbf{o}, r)$ and W. In other words, as $b_3(\mathbf{o}, r)$ increases, the task is to evaluate $O(\mathbf{o}, r)$ until W has been entirely enclosed within $b_3(\mathbf{o}, r)$. In order to evaluate $O(\mathbf{o}, r)$ for all possible values of the radius r, the analysis is split into 5 *cases*.

Let $\mathcal{B}_{(i)}(r)$ denote the overall volume of the segments lying outside W with respect to the corresponding case i. Then, $O(\mathbf{o}, r)$ can be evaluated by considering the volume segments of $b_3(\mathbf{o}, r)$ lying outside the faces of W, i.e., $O_{(i)}(\mathbf{o}, r) = |b_3(\mathbf{o}, r)| - \mathcal{B}_{(i)}(r)$ with respect to the case i and $|b_3(\mathbf{o}, r)| = \frac{4\pi}{3}r^3$. The problem is reduced to the evaluation of $\mathcal{B}_{(i)}(r)$.

Case 1, corresponds to $0 \leqslant r \leqslant R_{hex}$, i.e., $b_3(\mathbf{o}, r)$ lies completely within W resulting to $\mathcal{B}_{(1)}(r) = 0$, as shown in Fig. B.2a.

Case 2, shown in Fig. B.2b, corresponds to $R_{hex} < r \leqslant R_{sq}$. In this case, volume segments of $b_3(\mathbf{o}, r)$ start lying outside W. While the distance $R_{sq} \geqslant R_{hex}$, $b_3(\mathbf{o}, r)$ does not cross the square faces of W. Fortunately, these volume segments are *spherical caps*, lying upon the hexagonal faces of W. The volume V_{cap}^{hex} of a spherical cap is given by $V_{cap}^{hex}(r) =$

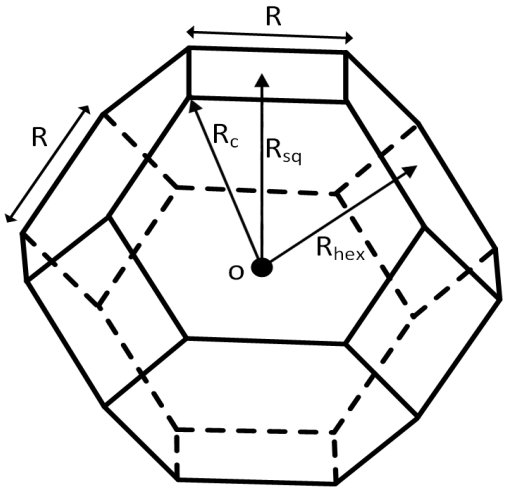

Figure B.1: The truncated octahedron cell-shape.

$\frac{\pi}{3}(r - R_{hex})^2(2r + R_{hex})$ and consequently $\mathcal{B}_{(2)}(r)$ can be evaluated as $\mathcal{B}_{(2)}(r) = 8V_{cap}^{hex}(r)$.

Case 3, shown in Fig. B.2c, corresponds to $R_{sq} < r \leqslant R_{mid}$. As the radius r of $b_3(\mathbf{o}, r)$ exceeds R_{sq}, volume segments of $b_3(\mathbf{o}, r)$ start crossing the 14 faces of W. Notice that the limiting values of the third case are defined for $r = R_{mid}$, as shown in Fig. 11d. The radius $R_{mid} = \frac{3}{2}R$, is called midradius of W and it indicates the maximum r for which the spherical caps are *simultaneously* inscribed in the hexagonal and square faces of W. The volume $V_{cap}^{sq}(r)$ of a spherical cap lying upon a square face of W is given by $V_{cap}^{sq}(r) = \frac{\pi}{3}(r - R_{sq})^2(2r + R_{sq})$ and consequently $\mathcal{B}_{(3)}(r)$ can be evaluated as $\mathcal{B}_{(3)}(r) = 8V_{cap}^{hex}(r) + 6V_{cap}^{sq}(r)$.

Case 4 corresponds to $R_{mid} < r \leqslant R_c$, i.e., until W is entirely enclosed within $b_3(\mathbf{o}, r)$. While spherical caps still lie upon the hexagonal and square faces of W, they extend beyond the perimeter of the faces of W and thus cannot be used for evaluation. In this case, there is an *overlap* between the volume segments formed outside W, which complicates the task of finding $O(\mathbf{o}, r)$.

Let $a_{ext}^{hex}(r), a_{ext}^{sq}(r)$ denote the base radius of the extending spherical cap lying upon a hexagonal and a square face of W, respectively, as shown in Fig. B.4a and Fig. B.4b. The key idea is to remove that volume segments of the spherical caps that lie outside the hexagonal and square faces of W. Let $\Delta_{hex}(r)$ and $\Delta_{sq}(r)$ denote the volume segments of a spherical cap formed outside the hexagonal and square faces of W, respectively, and extend above the plane in which the face belongs. As seen from top, these segments are illustrated in Fig. B.4 with faded grey. The remaining caps, are called *truncated caps*, and are illustrated in Fig. B.4 with dark grey. Let $T_{cap}^{hex}(r), T_{cap}^{sq}(r)$ denote the volume of a truncated cap lying upon a hexagonal and square face of W, respectively.

$\mathcal{B}_{(4)}(r)$ can then be approximately evaluated as the sum of the truncated caps and the remaining volume segments of $b_3(\mathbf{o}, r)$ lying between adjacent truncated caps, as shown with

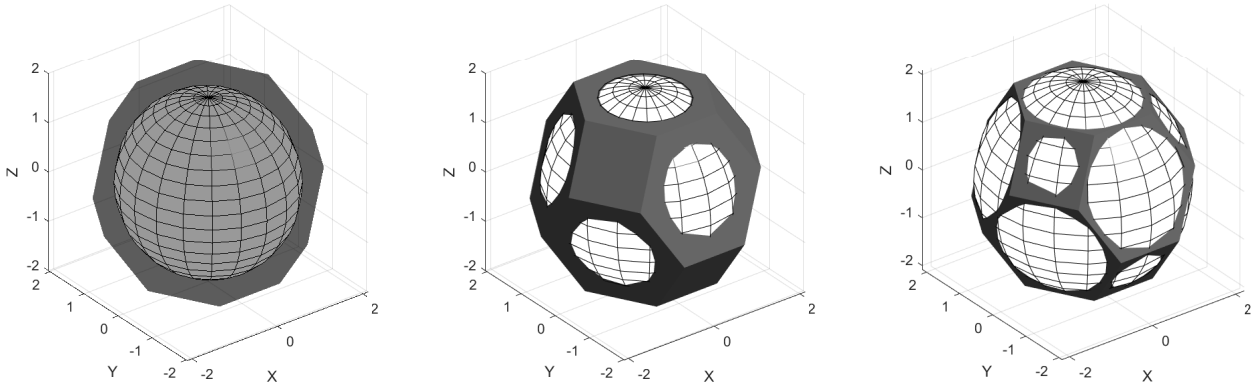

(a) $r \leqslant R_{hex}$ (b) $R_{hex} < r \leqslant R_{sq}$ (c) $R_{sq} < r \leqslant R_{mid}$

(d) $r = R_{mid}$ (e) $R_{mid} < r \leqslant R_c$ (f) $r > R_c$

Figure B.2: Illustration of the overlap between $b_3(\mathbf{o}, r)$ and W for different values of the radius r.

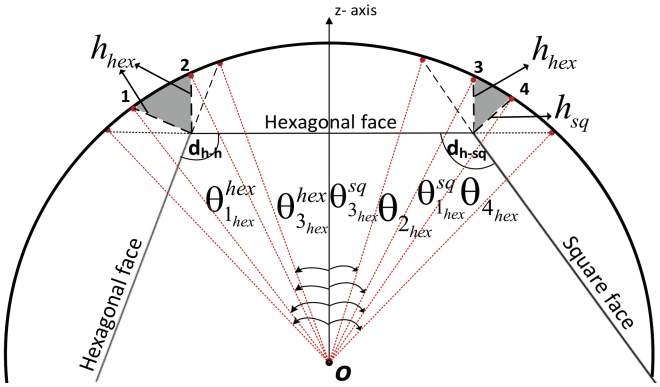

Figure B.3: Side view of truncated octahedron.

grey color in Fig. B.3. Let $S^{hex}_{hex}(r), S^{sq}_{hex}(r)$ denote the volume segments, whose side view are limited by the points 1 and 2, and 3 and 4, respectively. Then, $\mathcal{B}_{(4)}(r) = 8T^{hex}_{cap}(r) + 6T^{sq}_{cap}(r)+12S^{hex}_{hex}(r)+24S^{sq}_{hex}(r)$, where $T^{hex}_{cap}(r) = V^{hex}_{cap}(r)-6\Delta_{hex}(r)+3S^{hex}_{hex}(r)+3S^{sq}_{hex}(r)$ and $T^{sq}_{cap}(r) = V^{sq}_{cap}(r)-4\Delta_{sq}(r)+4S^{sq}_{hex}(r)$ are the volumes of a truncated cap lying upon hexagonal and square face of W, respectively. Notice that $\Delta_{hex}(r), \Delta_{sq}(r)$ incorporate $S^{hex}_{hex}(r), S^{sq}_{hex}(r)$, which need to be added in the expressions of $T^{hex}_{cap}(r), T^{sq}_{cap}(r)$ in order to avoid considering twice the volume segments $S^{sq}_{hex}(r), S^{sq}_{hex}(r)$ in the evaluation of $\mathcal{B}_{(4)}(r)$.

The problem is reduced to the evaluation of the volume segments $S^{hex}_{hex}(r), S^{sq}_{hex}(r), \Delta_{hex}(r), \Delta_{sq}(r)$. Fortunately, these volume segments are *spherical volume elements*. Consequently, they can be easily calculated by integrating the spherical volume elements with respect to the appropriate ranges for the spherical coordinates $(\bar{r},\ \theta,\ \phi\ )$. Note that θ, ϕ are used in order to indicate the set of the polar and azimuthal angles shown in Fig. B.3 and Fig. B.4, respectively. The requested volume segments are then given by

$$S^{hex}_{hex}(r) = \int_{\theta_{2_{hex}}}^{\theta^{hex}_{1_{hex}}} \int_0^{2\phi_{hex}} \int_r^{R_c} \bar{r}^2 \sin\theta \, \mathrm{d}\bar{r} \, \mathrm{d}\phi \, \mathrm{d}\theta, \tag{B.1}$$

$$S^{sq}_{hex}(r) = \int_{\theta_{2_{hex}}}^{\theta^{sq}_{1_{hex}}} \int_0^{2\phi_{hex}} \int_r^{R_c} \bar{r}^2 \sin\theta \, \mathrm{d}\bar{r} \, \mathrm{d}\phi \, \mathrm{d}\theta, \tag{B.2}$$

$$\Delta_{hex}(r) = \int_{\theta_{2_{hex}}}^{\theta_{4_{hex}}} \int_0^{2\phi_{hex}} \int_r^{R_c} \bar{r}^2 \sin\theta \, \mathrm{d}\bar{r} \, \mathrm{d}\phi \, \mathrm{d}\theta, \tag{B.3}$$

$$\Delta_{sq}(r) = \int_{\theta^{sq}_{3_{hex}}}^{\theta^{sq}_{1_{hex}}} \int_0^{2\phi_{hex}} \int_r^{R_c} \bar{r}^2 \sin\theta \, \mathrm{d}\bar{r} \, \mathrm{d}\phi \, \mathrm{d}\theta. \tag{B.4}$$

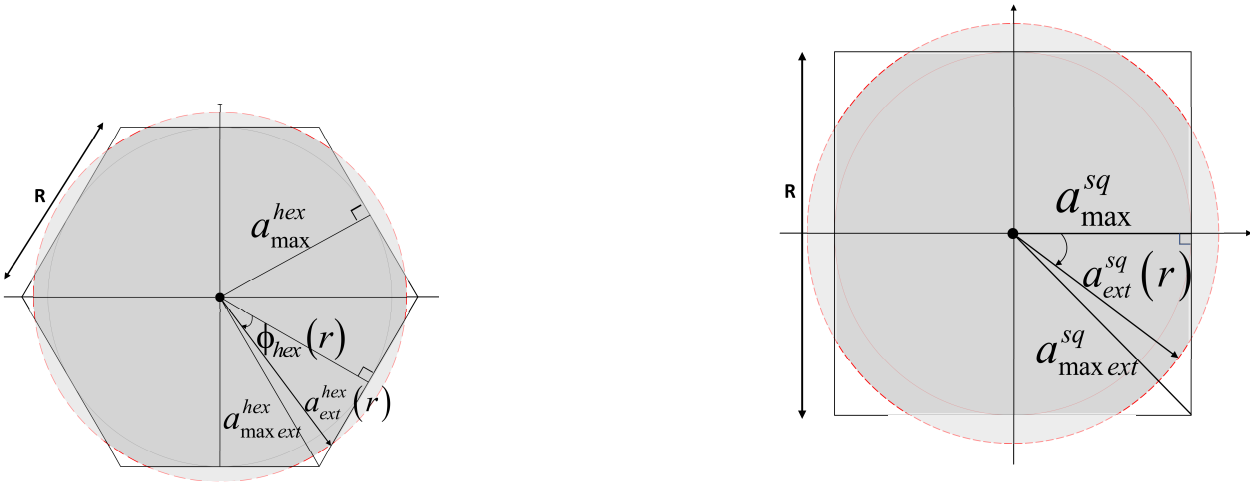

(a) Hexagonal face. (b) Square face.

Figure B.4: Top view of the truncated caps formed upon the faces of the truncated octahedron.

The angles under investigation (shown in Fig. B.3 and in Fig. B.4) are given by

$$\theta_{2_{hex}} = \arcsin\left(\frac{a^{hex}_{\max}}{r}\right), \quad \theta_{4_{hex}} = \arcsin\left(\frac{a^{hex}_{\text{ext}}}{r}\right), \tag{B.5}$$

$$\theta^{hex}_{1_{hex}} = \arcsin\left(\frac{a^{hex}_{max} + \sin(d_{h-h})h_{hex}}{r}\right), \tag{B.6}$$

$$\theta^{sq}_{1_{hex}} = \arcsin\left(\frac{a^{hex}_{max} + \sin(d_{h-sq})h_{sq}}{r}\right), \tag{B.7}$$

$$\theta^{sq}_{3_{hex}} = \arccos\left(\frac{R_{hex} + \sin(d_{6-4})(a^{sq}_{ext} - a^{sq}_{max})}{r}\right), \tag{B.8}$$

$$\phi_{hex} = \arccos\left(\frac{a^{hex}_{max}}{\sqrt{r^2 - R^2_{hex}}}\right), \tag{B.9}$$

where $a^{hex}_{max} = R\frac{\sqrt{3}}{2}$, $a^{sq}_{max} = \frac{R}{2}$, $a^{hex}_{ext} = \sqrt{r^2 - R^2_{hex}}$, $a^{sq}_{ext} = \sqrt{r^2 - R^2_{sq}}$, $d_{h-h} = \arccos(-\frac{1}{3})$, $d_{h-sq} = \arccos(-\frac{1}{\sqrt{3}})$, $h_{hex} = \sqrt{r^2 - (a^{hex}_{max})^2} - R_{hex}$, $h_{sq} = \sqrt{r^2 - (a^{sq}_{max})^2} - R_{sq}$. After evaluating (B.1)- (B.4) in closed form and after some algebraic manipulations and simplifications

$\mathcal{B}_{(4)}(r)$ is given by

$$\mathcal{B}_{(4)}(r) = \mathcal{B}_{(3)}(r) + \frac{8\,(r^3 - R_{mid}^3)}{3}\Bigg(\frac{\sqrt{6}R}{r} + 4\sqrt{3}\sqrt{1-\left(\frac{a_{max}^{sq}}{r}\right)^2} - 12\sqrt{1-\left(\frac{a_{max}^{hex}}{r}\right)^2} + 2\sqrt{6}\sqrt{1-\left(\frac{R_{sq}}{r}\right)^2}\Bigg)\arccos\left(\frac{a_{max}^{hex}}{\sqrt{r^2-R_{hex}^2}}\right). \tag{B.10}$$

Case 5 is identified for $r > R_c$, i.e., W becomes entirely enclosed within $b_3(\mathbf{o}, r)$, as shown in Fig. B.2f. In this case, it is clear that $O(\mathbf{o}, r) = |W|$ and this also completes the proof.

B.2 Proof of Theorem 3.5

The proof for deriving (3.4) follows the same lines as in [46] and hence it is omitted here. Now, having derived $O(\mathbf{o}, r)$, (3.6)-(3.8) can be obtained after taking the derivative of $O(\mathbf{o}, r)$ with respect to the appropriate range of r and applying algebraic manipulations. □

B.3 Proof of Corollary 3.7

Based on the approach presented in [80], the complementary CDF of R_n is the probability that there are less than n UAV-UEs closer than r, for $0 \leq r \leq R_c$, and it is given directly through (3.12) as

$$\bar{F}_{R_n}(r) = \sum_{k=0}^{n-1} T_k e^{-\lambda O(\mathbf{o},r)}. \tag{B.11}$$

The PDF of R_n can now be obtained as $f_{R_n}(r) = -\frac{\mathrm{d}\bar{F}_{R_n}(r)}{\mathrm{d}r}$, which after some computations results in

$$\begin{aligned} f_{R_n}(r) &= \lambda\frac{\mathrm{d}O(\mathbf{o},r)}{\mathrm{d}r}\Big(\sum_{k=0}^{n-1} T_k - \sum_{k=1}^{n-1} T_{k-1}\Big)e^{-\lambda O(\mathbf{o},r)} \\ &= \lambda\frac{\mathrm{d}O(\mathbf{o},r)}{\mathrm{d}r} T_{n-1} e^{-\lambda O(\mathbf{o},r)} \\ &= \underbrace{n\frac{\mathrm{d}O(\mathbf{o},r)}{\mathrm{d}r} O(\mathbf{o},r)^{n-1}}_{\frac{\mathrm{d}(O(\mathbf{o},r)^n)}{\mathrm{d}r}} \frac{\lambda^n e^{-\lambda O(\mathbf{o},r)}}{n\Gamma(n)}, \end{aligned} \tag{B.12}$$

which is identical to (3.15). Then, (3.16) is directly obtained as the complementary of B.11, and this completes the proof.

B.4 Proof of Lemma 3.12

Conditioned the serving distance r_s, the Laplace transform of the interference received from the UAV-UEs in W is given by

$$\begin{aligned}
&\mathcal{L}_{I_{oct}}(s|r_s) = \mathbb{E}_{I_{oct}}[\exp(-sI_{oct})] = \mathbb{E}_{I_{oct}^{near},I_{oct}^{far}}[\exp(-s(I_{oct}^{near}+I_{oct}^{far}))] \\
&\overset{(a)}{=} \mathbb{E}_{I_{oct}^{near}}[\exp(-sI_{oct}^{near})]\cdot\mathbb{E}_{I_{oct}^{far}}[\exp(-sI_{oct}^{far})] \\
&\overset{(b)}{=} \mathbb{E}_{U_i^{near}}\Big[\prod_{i=1}^{n-1}\mathbb{E}_{h_i}[\exp(-sh_i(U_i^{near}|r_s)^{-\alpha})]\Big]\mathbb{E}_{U_i^{far}}\Big[\prod_{i=1}^{N-n}\mathbb{E}_{h_i}[\exp(-sh_i(D_i^{near}|r_s)^{-\alpha})]\Big] \\
&\overset{(c)}{=} \mathbb{E}_{U_i^{near}}\Big[\prod_{i=1}^{n-1}\Big(1+\frac{su_i^{-\alpha}}{m_I}\Big)^{-m_I}\Big]\mathbb{E}_{U_i^{far}}\Big[\prod_{i=1}^{N-n}\Big(1+\frac{su_i^{-\alpha}}{m_I}\Big)^{-m_I}\Big] \\
&= \Big[\mathbb{E}_{U_i^{near}}\Big[\Big(1+\frac{su_i^{-\alpha}}{m_I}\Big)^{-m_I}\Big]\Big]^{n-1}\Big[\mathbb{E}_{U_i^{far}}\Big[\Big(1+\frac{su_i^{-\alpha}}{m_I}\Big)^{-m_I}\Big]\Big]^{N-n},
\end{aligned} \tag{B.13}$$

In (B.13), (a) follows from the independence between the interference power I_{oct}^{near} experienced in the near zone and the interference power I_{oct}^{far} experienced in the far zone, (b) follows from the independence of channel gains and the distances of interferers from the reference UAV-BS and by expressing the sum as a product, and (c) follows from the MGF of gamma random variable h_i. By applying the definition of expectation and using the conditional PDFs of U_i^{near}, U_i^{far}, (3.30) yields. Following the same procedure, (3.31) is derived. Moreover, using the formula $\int(1+px^{-q})^{-m}x^k\,\mathrm{d}x = \frac{x^{k+1}}{k+1}\,{}_2F_1\left(m,-\frac{k+1}{q};1-\frac{k+1}{q};-px^{-q}\right)$, the closed-form solution of (3.31) yields and this completes the proof.

B.5 Simulation Methodology for the Deployment of a 3D BPP of N Points in W

A truncated octahedron W of edge length $R = 1$ centered at the origin $\mathbf{o}$ has vertex coordinates given by all permutations of $\big(\pm\sqrt{2},\pm\frac{\sqrt{2}}{2},0\big)$. The key idea is to deploy a point uniformly distributed in $b_3(\mathbf{o},R_c)$. Then the decision about whether the particular point lies within the 14 planes forming W, is made. The algorithm for distributing N points uniformly and independently inside W is as follows

Algorithm 1: Simulating a 3D BPP of N points in W.

Step 1: Define the vertex coordinates of all 8 hexagons and 6 squares of W.
Step 2: For a considered face of W, take 2 vectors $\vec{v_1}, \vec{v_2}$ that belong to the respective face. Derive the normal vector $\vec{n}$ as the cross product of the 2 vectors $\vec{v_1}, \vec{v_2}$, i.e., $\vec{n} = \vec{v_1} \times \vec{v_2}$. Note that the direction of $\vec{n}$ should point inside, towards the center **o** .
Step 3: For the same face of W, consider an arbitrary vertex **V** of the face and derive its position vector $\vec{v}$.
Step 4: Draw a point **P** uniformly and randomly distributed inside $b_3(\mathbf{o}, R_c)$. Derive $\vec{p}$ as the position vector of **P**.
Step 5: Derive the vector $\vec{d}$ as $\vec{d} = \vec{p} - \vec{v}$.
Step 6: Decide whether to keep point **P** or not.
if $\vec{n} \cdot \vec{d} \geqslant 0$ **then**
| keep **P**
else
| discard **P**
end
Step 7: Repeat the steps 1-6 for each one of the 14 faces of W, by ignoring step 4. If $\vec{n} \cdot \vec{d} \geqslant 0$ for all of the faces of W, the point **P** lies within W.
Step 8: Repeat steps 1-7 until N points lie within W.

Appendix C

Proofs of Chapter 4

C.1 Proof of Lemma 4.1

The conditional PDF of RV I is given by

$$f_I(x|R_s=s)=\int_s^R f_{I|R_I}(x|r_I,R_s=s)f_{R_I}(r_I|R_s=s)\mathrm{d}r_I. \tag{C.1}$$

By substituting (4.6), (4.1) in (C.1) and applying the Binomial expansion in the term $(R^3-r_I^3)^{N-2}$, the following integral appears

$$I_1=\int_s^R r_I^{am_I+3k+2}\exp\left(-\frac{xr_I^a}{\theta_I P_I}\right)\mathrm{d}r_I, \tag{C.2}$$

which using [40, eq. (3.381.8)], results in a subtraction of the lower incomplete gamma function, $I_1=\gamma\left(\frac{3+3k+am_I}{a},\frac{xs^a}{P_I\theta_I}\right)-\gamma\left(\frac{3+3k+am_I}{a},\frac{xR^a}{P_I\theta_I}\right)$ [40, eq. (8.350.1)]. Through transformation of I_1 to exponential integral using [68, eq. (06.06.27.0003.01)] and adoption of the Binomial expansion, (4.7) yields and that completes the proof.

C.2 Proof of Lemma 4.2

The PDF $f_{SIR}^{fix}(\gamma|R_s=s)$, after a change of variable is given by

$$f_{SIR}^{fix}(\gamma|R_s=s)=\int_0^\infty f_S(y\gamma)f_I(y|R_s=s)y\mathrm{d}y. \tag{C.3}$$

After substituting $f_S(y\gamma)$, which is of the form given by (4.6), and (4.7) in (C.3), the only integral existing is

$$\begin{aligned}I_2=&\int_0^\infty y^{m_I+m_s-1}\exp\left(-\frac{y\gamma}{s^{-a}\theta_s P_s}\right)E_{1-\frac{3(1+k)}{a}-m_I}\left(\frac{s^a y}{\theta_I P_I}\right)\mathrm{d}y\\&-\int_0^\infty y^{m_I+m_s-1}\exp\left(-\frac{y\gamma}{s^{-a}\theta_s P_s}\right)E_{1-\frac{3(1+k)}{a}-m_I}\left(\frac{R^a y}{\theta_I P_I}\right)\mathrm{d}y.\end{aligned} \tag{C.4}$$

By expressing the exponential function and the exponential integral function through the Meijer G-function according to [68, eq. (01.03.26.0004.01)] and [68, eq. (06.34.26.0005.01)], respectively, the integral I_2 can be directly evaluated in closed form using [68, eq. (07.34.21.0011.01)]. The resulting Meijer G-function can be expressed in terms of the Gauss hypergeometric function using [40, eq. (9.34.8)]. After applying some simplifications, finally yields (4.8).

C.3 Proof of Lemma 4.3

Disregarding any constant value for brevity, the CDF is expressed as a difference of integrals

$$\begin{aligned} F_{SIR}^{fix}(\gamma|R_s=s) &= \int_0^{\gamma} f_{SIR}^{fix}(z|R_s=s)\mathrm{d}z \\ &= \int_0^{\gamma} z^{m_s-1}\,{}_2F_1\left(\cdot,\cdot;\cdot;-\frac{P_I\theta_I}{P_s\theta_s}z\right)dz - \int_0^{\gamma} z^{m_s-1}\,{}_2F_1\left(\cdot,\cdot;\cdot;-\frac{P_IR^{-a}\theta_I}{P_ss^{-a}\theta_s}z\right)\mathrm{d}z \\ &\overset{(a)}{=} \frac{\gamma^{m_s}}{m_s}\,{}_3F_2\left(\cdot,\cdot,\cdot;\cdot,\cdot;-\frac{P_I\theta_I}{P_s\theta_s}\gamma\right) - \frac{\gamma^{m_s}}{m_s}\,{}_3F_2\left(\cdot,\cdot,\cdot;\cdot,\cdot;-\frac{P_IR^{-a}\theta_I}{P_ss^{-a}\theta_s}\gamma\right). \end{aligned} \tag{C.5}$$

In (C.5), a follows from [68, eq. (07.23.21.0002.01)]. After substituting (C.5) in the initial expression and applying some simplifications, (4.10) yields immediately.

C.4 Proof of Lemma 4.4

The CDF of V yields from double integration of the joint distance PDF with respect to the limits of r_s, r_I and consequently

$$F_V(v) = \int_0^{Rv}\int_{r_s/v}^{R} f_{R_I}(r_I|R_s=r_s)f_{R_s}(r_s)\mathrm{d}r_I\mathrm{d}r_s, \tag{C.6}$$

where $v \in [0,1]$. By substituting the distance distributions in the above integral and applying the Binomial expansion, $F_V(v)$ is derived. The PDF $f_V(v)$ is then obtained by simply taking the derivative of $F_V(v)$ and that completes the proof.

C.5 Proof of Lemma 4.5

Begin from the CDF $F_{SIR}^{rand}(\gamma)= \mathbb{P}(SIR \le \gamma) = \mathbb{E}_V\left\{F_H(\gamma V^a)\right\} = \int_0^1 F_H(\gamma v^a)f_V(v)dv$. Making the change of variable $y = v^a$ and afterwards a second change of variable by setting

$x = \frac{\theta_I \gamma y}{\theta_s}$, the only remaining integral to be solved is I_3, given by

$$I_3 = \int_0^{\frac{\theta_I \gamma}{\theta_s}} x^{m_s + \frac{3}{a} - 1} \, {}_2F_1(m_s, m_s + m_I; 1 + m_s; -x) \, \mathrm{d}x. \tag{C.7}$$

Using [68, eq. (07.23.21.0004.01)], (4.16) yields immediately. The respective PDF given by (4.17) is now given directly by simply taking the derivative of (4.16).

C.6 Proof of Proposition 4.8

If any constant value is neglected, by substituting (4.10) and the derivative of $P_e(\gamma)$ in (4.19), $\bar{P}_{e,fix}^{BPSK}$ results in

$$\begin{aligned}\bar{P}_{e,fix}^{BPSK} = &\int_0^\infty \gamma^{m_s - \frac{1}{2}} e^{-\gamma} \, {}_3F_2\Big(\frac{am_s - 3k - 3}{a}, m_s + m_I, m_s; \frac{am_s - 3k - 3}{a}, m_s + 1; -\frac{P_I \theta_I}{P_s \theta_s}\gamma\Big) \mathrm{d}\gamma \\ &- \int_0^\infty \gamma^{m_s - \frac{1}{2}} e^{-\gamma} \, {}_3F_2\Big(\frac{am_s - 3k - 3}{a}, m_s + m_I, m_s; \frac{am_s - 3k - 3}{a}, m_s + 1; -\frac{P_I R^{-a} \theta_I}{P_s s^{-a} \theta_s}\gamma\Big) \mathrm{d}\gamma.\end{aligned} \tag{C.8}$$

Through a simple change of variables $c_1 = \frac{P_I \theta_I}{P_s \theta_s}\gamma$, $c_2 = \frac{P_I R^{-a} \theta_I}{P_s s^{-a} \theta_s}\gamma$ and using [40, eq. (9.34.8)], (C.8) results to

$$\begin{aligned}\bar{P}_{e,fix}^{BPSK} = &\frac{\Gamma\left(\frac{-3+a-3k+am_s}{a}\right)\Gamma(1+m_s)}{\Gamma\left(\frac{-3-3k+am_s}{a}\right)\Gamma(m_s+m_I)\Gamma(m_s)} \\ &\times \left\{ \int_0^\infty \gamma^{m_s - \frac{1}{2}} e^{-\frac{\gamma}{c_1}} G_{3,3}^{1,3}\left(\gamma \,\middle|\, \begin{matrix} 1 + \frac{3+3k-am_s}{a}, 1 - m_s - m_I, 1 - m_s \\ 0, 1 - \frac{-3+a-3k+am_s}{a}, 1 - m_s \end{matrix}\right) \mathrm{d}\gamma \right. \\ &\left. - \int_0^\infty \gamma^{m_s - \frac{1}{2}} e^{-\frac{\gamma}{c_2}} G_{3,3}^{1,3}\left(\gamma \,\middle|\, \begin{matrix} 1 + \frac{3+3k-am_s}{a}, 1 - m_s - m_I, 1 - m_s \\ 0, 1 - \frac{-3+a-3k+am_s}{a}, 1 - m_s \end{matrix}\right) \mathrm{d}\gamma \right\}.\end{aligned} \tag{C.9}$$

By using [40, eq. (7.813.1)], the integrals in (C.9) can now be easily derived in closed form as in (4.20). The same procedure is also followed for the derivation of the average BER for the DBPSK scheme.

C.7 Proof of Proposition 4.11

After expressing the $\log_2(\cdot)$ and the hypergeometric functions of (4.25) in terms of the Meijer G- function, by using [68, eq. (01.05.26.0002.01)] and [68, eq. (07.23.26.0004.01)],

respectively, (4.25) results in

$$\bar{C} = BW \times$$
$$\int_0^\infty \frac{3\gamma^{m_s}\left(\frac{P_I\theta_I}{P_s\theta_s}\right)^{m_s+1}\frac{\Gamma(1+\frac{3}{a}+m_s)}{\Gamma(\frac{3}{a}+m_s)}}{\ln(2)\Gamma(m_s)\Gamma(m_I)(am_s+3)} G_{2,2}^{1,2}\left(\frac{P_I\theta_I}{P_s\theta_s}\gamma\middle| \begin{matrix} -\left(\frac{3}{a}+m\right), -(m_s+m_I) \\ -1, -\left(1+\frac{3}{a}+m_s\right)\end{matrix}\right) G_{2,2}^{1,2}\left(\gamma\middle| \begin{matrix} 1,1 \\ 1,0\end{matrix}\right) \mathrm{d}\gamma. \tag{C.10}$$

Now, (C.10) can directly be derived in closed form by using [68, eq. (07.34.21.0011.01)]. After applying some simplifications, (4.26) is deduced.

Appendix D

Proofs of Chapter 5

D.1 Proof of Lemma 5.1

The joint PDF $f_{r_n,\theta_n,\phi_n}(r_n,\theta_n,\phi_n)$ is given by

$$\begin{aligned} f_{r_n,\theta_n,\phi_n}(r_n,\theta_n,\phi_n) &\overset{(a)}{=} f_{r_n}(r_n) f_{\theta_n}(\theta_n) f_{\phi}(\phi_n) \\ &\overset{(b)}{=} \frac{\sin(\theta_n)}{4\pi} \frac{3 r_n^{3n-1} c_\lambda^n}{\Gamma(n)} \exp(-c_\lambda r_n^3), \end{aligned} \tag{D.1}$$

where (a) follows from the independence between r_n, θ_n, ϕ_n, and (b) is derived given that $f_{r_n}(r_n)$ is given by [2, eq. (11)], $f_{\theta_n}(\theta_n) = \frac{\sin(\theta_n)}{2}$, $f_{\phi_n}(\phi_n) = \frac{1}{2\pi}$, and $c_\lambda = \frac{4\pi\lambda}{3}$.

D.2 Proof of Theorem 5.3

The conditional coverage probability is given by [57],

$$\begin{aligned} &\mathcal{P}_c^{cond}(\gamma|w_n) \\ &= \sum_{k=0}^{m_s-1} \frac{(-1)^k}{k!} \left(\frac{m_s \gamma r_n^\alpha}{p_0} \right)^k \left[\frac{\partial^k \mathcal{L}_{I_{tot}}(s|w_n)}{\partial s^k} \right]_{s=\frac{m_s\gamma r_n^\alpha}{p_0}}. \end{aligned} \tag{D.2}$$

Then, $\mathcal{P}_c(\gamma)$ is obtained by deconditioning $\mathcal{P}_c^{cond}(\gamma|w_n)$ over the spatial location w_n of the receiver.

D.3 Proof of Lemma 5.5

Conditioned on the serving distance r, the $(N-1)$ UAV-BSs are uniformly distributed in the spherical shell $\mathcal{S} = b_3(\mathbf{o}, D) - b_3(\mathbf{o}, r)$ with volume $V_{\mathcal{S}} = \frac{4\pi}{3}(D^3 - r^3)$. The joint PDF

$f_{x_i,y_i,z_i}(x,y,z)$ of the i-th UAV-BS is given by

$$f_{x_i,y_i,z_i}(x,y,z) = \frac{1}{V_{\mathcal{S}}}, \quad r \leq x_i^2 + y_i^2 + z_i^2 \leq D. \tag{D.3}$$

By applying the transformation of changing coordinate system to (v_i, θ_i, ϕ_i), yields the following equality

$$\int_r^D \int_0^{\pi} \int_0^{2\pi} \underbrace{\frac{1}{V_{\mathcal{S}}} v_i^2 \sin(\theta_i)}_{f_{V_i,\theta_i,\phi_i}(v_i,\theta_i,\phi_i)} \mathrm{d}\phi_i \mathrm{d}\theta_i \mathrm{d}v_i = 1, \tag{D.4}$$

where $\theta \in [0,\pi]$ and $\phi \in [0,2\pi]$ are the elevation and azimuth angles of the i-th UAV-BS with PDFs given by $f_{\theta_i}(\theta_i) = \frac{\sin(\theta_i)}{2}$, and $f_{\phi_i}(\phi_i) = \frac{1}{2\pi}$, respectively. Due to independence between v_i, θ_i, ϕ_i, $f_{V_i,\theta_i,\phi_i}(v_i,\theta_i,\phi_i) = f_{V_i}(v_i) f_{\theta_i}(\theta_i) f_{\phi_i}(\phi_i)$. By solving w.r.t. $f_{V_i}(v_i)$, (5.12) yields.

D.4 Proof of Lemma 5.6

Following similar lines as in [57, Appendix E],

$$\mathcal{L}_I(s|r) = \left[\int_r^D \left(1 + \frac{s p_0 v_i^{-\alpha}}{m_k}\right)^{-m_k} \frac{3v_i^2}{D^3 - r^3} \, dv_i \right]^{N-1}. \tag{D.5}$$

By using [68, eq. (01.02.26.0007.01)] and [68, eq. (07.34.21.0002.01)] along with some mathematical manipulations, (D.5) reduces to

$$\mathcal{L}_I(s|r) = (H(r) - H(D))^{N-1}, \tag{D.6}$$

$$H(x) = \frac{\frac{3}{a}\left(\frac{s p_0}{m_k}\right)^{3/a}}{\Gamma(m_k)(D^3 - r^3)} G_{2,2}^{1,2}\left(\frac{s p_0}{m_k x^a} \middle| \begin{matrix} 1, 1 - \frac{3}{a} - m_k \\ -\frac{3}{a}, 0 \end{matrix} \right), \tag{D.7}$$

By using [40, eq. (9.34.7)] and after applying some simplifications, (D.6) reduces to (5.13).

Bibliography

[1] D. Moltchanov, E. Sopin, V. Begishev, A. Samuylov, Y. Koucheryavy and K. Samouylov, "A Tutorial on Mathematical Modeling of 5G/6G Millimeter Wave and Terahertz Cellular Systems," *IEEE Commun. Surv. Tutor*, vol. 24, no. 2, pp. 1072-1116, Second quarter 2022.

[2] H. Wei, N. Deng and M. Haenggi, "Performance Analysis of Inter-Cell Interference Coordination in mm-Wave Cellular Networks," *IEEE Trans. Wireless Commun.*, vol. 21, no. 2, pp. 726-738, Feb. 2022.

[3] T. Bai and R. W. Heath, "Coverage and rate analysis for millimeter-wave cellular networks," *IEEE Trans. Wireless Commun.*, vol. 14, no. 2, pp. 1100–1114, Feb. 2015.

[4] N. R. Olson, J. G. Andrews and R. W. Heath, "Coverage and Capacity of Terahertz Cellular Networks With Joint Transmission," *IEEE Trans. Wireless Commun.*, vol. 21, no. 11, pp. 9865-9878, Nov. 2022.

[5] M. Mozaffari, A. Taleb Zadeh Kasgari, W. Saad, M. Bennis and M. Debbah, "Beyond 5G with UAVs: Foundations of a 3D wireless cellular network," *IEEE Trans. Wireless Commun.*, vol. 18, no. 1, pp. 357-372, Jan. 2019.

[6] Y. Li, N. I. Miridakis, T. A. Tsiftsis, G. Yang and M. Xia, "Air-to-air communications beyond 5G: A novel 3D CoMP transmission scheme," *IEEE Trans. Wireless Commun.*, vol. 19, no. 11, pp. 7324-7338, Nov. 2020.

[7] C. K. Armeniakos, P. S. Bithas and A. G. Kanatas, "SIR analysis in 3D UAV networks: A stochastic geometry approach," *IEEE Access*, vol. 8, pp. 204963-204973, Nov. 2020.

[8] T. Hou, Y. Liu, Z. Song, X. Sun, and Y. Chen, "UAV-to-Everything (U2X) networks relying on NOMA: A stochastic geometry model," *IEEE Trans. on Veh. Technol.*, vol. 69, no. 7, pp. 7558-7568, Jul. 2020.

[9] *NR; User Equipment (UE) Radio Transmission and Reception; Part 1: Range 1 Standalone*, document 3GPP, TS 38.101-1, Version 15.9.0, Apr. 2020.

[10] V. V. Chetlur and H. S. Dhillon, "Coverage and Rate Analysis of Downlink Cellular Vehicle-to-Everything (C-V2X) Communication," *IEEE Trans. Wireless Commun.*, vol. 19, no. 3, pp. 1738-1753, Mar. 2020.

[11] S. M. Azimi-Abarghouyi, B. Makki, M. Nasiri-Kenari and T. Svensson, "Stochastic Geometry Modeling and Analysis of Finite Millimeter Wave Wireless Networks," *IEEE Trans. on Veh. Technol.*, vol. 68, no. 2, pp. 1378-1393, Feb. 2019.

[12] J. Fan, L. Han, X. Luo, Y. Zhang and J. Joung, "Beamwidth Design for Beam Scanning in Millimeter-Wave Cellular Networks," *IEEE Trans. Veh. Technol.*, vol. 69, no. 1, pp. 1111-1116, Jan. 2020.

[13] Z. Gu, H. Lu, M. Zhang, H. Sun and C. W. Chen, "Association and Caching in Relay-Assisted mmWave Networks: A Stochastic Geometry Perspective,"*IEEE Trans. Wireless Commun.*, vol. 20, no. 12, pp. 8316-8332, Dec. 2021.

[14] X. Shi, N. Deng, N. Zhao and D. Niyato, "Coverage Enhancement in Millimeter-Wave Cellular Networks via Distributed IRSs," *IEEE Trans. Commun.*, doi: 10.1109/T-COMM.2022.3228298.

[15] T. -X. Zheng et al., "Physical-Layer Security of Uplink mmWave Transmissions in Cellular V2X Networks," *IEEE Trans. Wireless Commun.*, vol. 21, no. 11, pp. 9818-9833, Nov. 2022.

[16] M. S. Zia, D. M. Blough and M. A. Weitnauer, "Effects of SNR-Dependent Beam Alignment Errors on Millimeter-Wave Cellular Networks," *IEEE Trans. on Veh. Technol.*, vol. 71, no. 5, pp. 5216-5230, May 2022.

[17] S. Fang, G. Chen, X. Xu, S. Han and J. Tang, "Millimeter-Wave Coordinated Beamforming Enabled Cooperative Network: A Stochastic Geometry Approach," *IEEE Trans. Wireless Commun.*, vol. 69, no. 2, pp. 1068-1079, Feb. 2021.

[18] C. Zhang, W. Yi, Y. Liu, K. Yang and Z. Ding, "Reconfigurable Intelligent Surfaces Aided Multi-Cell NOMA Networks: A Stochastic Geometry Model," *IEEE Trans. Commun.*, vol. 70, no. 2, pp. 951-966, Feb. 2022.

[19] M. Haenggi, J. G. Andrews, F. Baccelli, O. Dousse, and M. Franceschetti, "Stochastic geometry and random graphs for the analysis and design of wireless networks", *IEEE J. Sel. Areas Commun.*, vol. 27, no. 7, pp. 1029–1046, Sep. 2009.

[20] J. G. Andrews, A. K. Gupta, A. M. Alammouri and H. S. Dhillon, *An Introduction to Cellular Network Analysis Using Stochastic Geometry*. Synthesis Lectures on Learning, Networks, and Algorithms (Springer), Jul. 2023.

[21] J. G. Andrews, F. Baccelli, and R. K. Ganti, "A tractable approach to coverage and rate in cellular networks", *IEEE Trans. Commun.*, vol. 59, no. 11, pp. 3122–3134, Nov. 2011.

[22] H. ElSawy, E. Hossain, and M. Haenggi, "Stochastic geometry for modeling, analysis, and design of multi-tier and cognitive cellular wireless networks: A survey", *IEEE Commun. Surveys Tuts.*, vol. 15, no. 3, pp. 996–1019, 3rd Quart., 2013.

[23] Z. Li and W. Wang, "Handover performance in dense mmWave cellular networks," in *Proc. 10th Int. Conf. Wireless Commun. Signal Process. (WCSP)*, Oct. 2018, pp. 1–7.

[24] S. S. Kalamkar, F. Baccelli, F. M. Abinader, A. S. Marcano Fani and L. G. Uzeda Garcia, "Beam Management in 5G: A Stochastic Geometry Analysis," *IEEE Trans. Wireless Commun.*, doi: 10.1109/TWC.2021.3110785.

[25] S. Aghashahi, S. Aghashahi, Z. Zeinalpour-Yazdi, A. Tadaion and A. Asadi, "Stochastic Modeling of Beam Management in mmWave Vehicular Networks," *IEEE Trans. Mob. Comput.*, doi: 10.1109/TMC.2021.3138449.

[26] W. Chen, L. Li, Z. Chen, H. H. Yang and T. Q. S. Quek, "Mobility and Blockage-induced Beam Misalignment and Throughput Analysis for THz Networks," *IEEE Global Commun. Conf. (GLOBECOM)*, pp. 1-6, Dec. 2021.

[27] M. Giordani et al., "A tutorial on beam management for 3GPP NR at mmWave frequencies," *IEEE Commun. Surveys Tuts.*, vol. 21, no. 1, pp. 173–196, 1st Quart., 2018.

[28] C. Pradhan , A. Li, L. Zhuo, Y. Li and B. Vucetic, "Hybrid-Precoding for mmWave Multi-User Communications in the Presence of Beam-Misalignment," *IEEE Trans. Wireless Commun.*, vol. 19, no. 9, pp. 6083-6099, Sep. 2020.

[29] M. Rebato, J. Park, P. Popovski, E. De Carvalho and M. Zorzi, "Stochastic Geometric Coverage Analysis in mmWave Cellular Networks With Realistic Channel and Antenna Radiation Models," *IEEE Trans. Commun.*, vol. 67, no. 5, pp. 3736-3752, May 2019.

[30] M. Banagar and H. S. Dhillon, "3D Two-Hop Cellular Networks With Wireless Backhauled UAVs: Modeling and Fundamentals," *IEEE Trans. Wireless Commun.*, vol. 21, no. 8, pp. 6417-6433, Aug. 2022.

[31] X. Yu, J. Zhang, M. Haenggi, and K. B. Letaief, "Coverage analysis for millimeter wave networks: The impact of directional antenna arrays," *IEEE J. Sel. Areas Commun.*, vol. 35, no. 7, pp. 1498–1512, Jul. 2017.

[32] N. Deng and M. Haenggi, "A Novel Approximate Antenna Pattern for Directional Antenna Arrays," *IEEE Wireless Commun. Lett.* , vol. 7, no. 5, pp. 832-835, Oct. 2018.

[33] W. Yi, Y. Liu, Y. Deng and A. Nallanathan, "Clustered UAV Networks With Millimeter Wave Communications: A Stochastic Geometry View," *IEEE Trans. Wireless Commun.*, vol. 68, no. 7, pp. 4342-4357, Jul. 2020.

[34] J. Schloemann, H. S. Dhillon, and R. M. Buehrer, "Toward a tractable analysis of localization fundamentals in cellular networks," *IEEE Trans. Wireless Commun.*, vol. 15, no. 3, pp. 1768–1782, Mar. 2016.

[35] V. V. Chetlur and H. S. Dhillon, "Downlink Coverage Analysis for a Finite 3-D Wireless Network of Unmanned Aerial Vehicles," *IEEE Trans. Commun.*, vol. 65, no. 10, pp. 4543-4558, Oct. 2017.

[36] T. Bhandari, H. S. Dhillon, and R. M. Buehrer, "The impact of proximate base station measurements on localizability in cellular systems," *in Proc. IEEE SPAWC*, Edinburgh, U.K., Jul. 2016.

[37] M. A. Kishk and H. S. Dhillon, "Joint Uplink and Downlink Coverage Analysis of Cellular-based RF-powered IoT Network", *IEEE Trans. Green Commun. Netw.*, vol. 2, no. 2, pp. 446-459, Jun. 2018.

[38] A. G. Kanatas, "Coordinates Distributions in Finite Uniformly Random Networks," *IEEE Access*, vol. 10, pp. 49005-49014, 2022.

[39] C. K. Armeniakos and A. G. Kanatas, "Angular Distance-Based Performance Analysis of mmWave Cellular Networks," *IEEE Global Commun. Conf. (GLOBECOM)*, pp. 5432-5437, Dec. 2022.

[40] I. Gradshteyn and I. M. Ryzhik, "*Tables of Integrals, Series, and Products*," 7th ed. New York, NY, USA: Academic, 2007.

[41] J. García-Rois et al., "On the Analysis of Scheduling in Dynamic Duplex Multihop mmWave Cellular Systems," *IEEE Trans. Wireless Commun.*, vol. 14, no. 11, pp. 6028-6042, Nov. 2015

[42] M. Rebato, L. Resteghini, C. Mazzucco and M. Zorzi, "Study of Realistic Antenna Patterns in 5G mmWave Cellular Scenarios," *in IEEE Int. Conf. Commun.*, 2018, pp. 1-6

[43] J. Wildman, P. H. J. Nardelli, M. Latva-aho and S. Weber, "On the Joint Impact of Beamwidth and Orientation Error on Throughput in Directional Wireless Poisson Networks," *IEEE Trans. Wireless Commun.*, vol. 13, no. 12, pp. 7072-7085, Dec. 2014.

[44] A. Thornburg, T. Bai and R. W. Heath, "Performance Analysis of Outdoor mmWave Ad Hoc Networks," *IEEE Trans. Signal Process.*, vol. 64, no. 15, pp. 4065-4079, Aug. 2016.

[45] J. G. Andrews, T. Bai, M. N. Kulkarni, A. Alkhateeb, A. K. Gupta, and R. W. Heath, "Modeling and analyzing millimeter wave cellular systems," *IEEE Trans. Commun.*, vol. 65, no. 1, pp. 403–430, Jan. 2017.

[46] S. Srinivasa and M. Haenggi, "Distance distributions in finite uniformly random networks: Theory and applications," *IEEE Trans. Veh. Technol.*, vol. 59, no. 2, pp. 940-949, Feb. 2010.

[47] N. Cherif, M. Alzenad, H. Yanikomeroglu and A. Yongacoglu, "Downlink Coverage and Rate Analysis of an Aerial User in Vertical Heterogeneous Networks (VHetNets)," *IEEE Trans. Wireless Commun.*, vol. 20, no. 3, pp. 1501-1516, Mar. 2021.

[48] 3GPP TR 38.831, "*User Equipment (UE) Radio Frequency (RF) Requirements for Frequency Range 2 (FR2)*", V16.1.0.

[49] M. Mozaffari, W. Saad, M. Bennis, Y. Nam and M. Debbah, "A tutorial on UAVs for wireless networks: applications, challenges, and open problems," *IEEE Commun. Surveys Tuts.*, vol. 21, no. 3, pp. 2334-2360, 2019

[50] Y. Zeng, Q. Wu, and R. Zhang, "Accessing from the sky: A tutorial on UAV communications for 5G and beyond," *Proceedings of the IEEE*, vol. 107, no. 12, pp. 2327–2375, Dec. 2019.

[51] M. Alzenad and H. Yanikomeroglu, "Coverage and rate analysis for unmanned aerial vehicle base stations with LoS/NLoS propagation," *IEEE Globecom Workshops* , pp. 1-7, 2018.

[52] M. M. Azari, G. Geraci, A. Garcia-Rodriguez and S. Pollin, "UAV-to-UAV Communications in Cellular Networks," *IEEE Trans. Wireless Commun.*, vol. 19, no. 9, pp. 6130-6144, Sep. 2020.

[53] M. Banagar and H. S. Dhillon, "Performance characterization of canonical mobility models in drone cellular networks," *IEEE Trans. Wireless Commun.*, vol. 19, no. 7, pp. 4994-5009, Jul. 2020.

[54] X. Wang and M. C. Gursoy, "Coverage analysis for energy-harvesting uav-assisted mmWave cellular networks," *IEEE J.Select. Areas Commun.*, vol. 37, no. 12, pp. 2832-2850, Dec. 2019.

[55] W. Yi, Y. Liu, E. Bodanese, A. Nallanathan, and G. K. Karagiannidis, "A unified spatial framework for uav-aided mmWave networks," *IEEE Trans. Commun.*, vol. 67, no. 12, pp. 8801-8817, Dec. 2019.

[56] T. Hou, Y. Liu, Z. Song, X. Sun and Y. Chen, "Multiple Antenna Aided NOMA in UAV Networks: A Stochastic Geometry Approach," *IEEE Trans. Commun.*, vol. 67, no. 2, pp. 1031-1044, Feb. 2019

[57] V. V. Chetlur and H. S. Dhillon, "Downlink coverage analysis for a finite 3-D wireless network of unmanned aerial vehicles," *IEEE Trans. Commun.*, vol. 65, no. 10, pp. 4543-4558, Oct. 2017

[58] X. Wang, H. Zhang, Y. Tian, and V. C. M. Leung, "Modeling and analysis of aerial base station-assisted cellular networks in finite areas under LoS and NLoS propagation," *IEEE Trans. Wireless Commun.*, vol. 17, no. 10, pp. 6985-7000, Oct. 2018.

[59] S. Enayati, H. Saeedi, H. Pishro-Nik, and H. Yanikomeroglu, "Moving aerial base station networks: A stochastic geometry analysis and design perspective," *IEEE Trans. Wireless Commun.*, vol. 18, no. 6, pp. 2977-2988, Jun. 2019.

[60] T. Z. H. Ernest, A. S. Madhukumar, R. P. Sirigina and A. K. Krishna, "NOMA-aided UAV communications over correlated rician shadowed fading channels," *IEEE Trans. Signal Process.* , vol. 68, pp. 3103-3116, May 2020.

[61] P. S. Bithas, V. Nikolaidis, A. G. Kanatas, and G. K. Karagiannidis, "UAV-to-ground communications: Channel modeling and UAV selection," *IEEE Trans. Commun.*, vol. 68, no. 8, pp. 5135-5144, Aug. 2020.

[62] M. A. Kishk, A. Bader and M. -S. Alouini, "On the 3-D placement of airborne base stations using tethered UAVs," *IEEE Trans. Commun.*, vol. 68, no. 8, pp. 5202-5215, Aug. 2020.

[63] Q. Wu, J. Xu and R. Zhang, "Capacity characterization of UAV-enabled two-user broadcast channel," *IEEE J. Select. Areas Commun.*, vol. 36, no. 9, pp. 1955-1971, Sep. 2018.

[64] K. Meng et al., "UAV-Enabled Integrated Sensing and Communication: Opportunities and Challenges," *IEEE Wireless Commun.*, vol. 31, no. 2, pp. 97-104, Apr. 2024.

[65] X. Yuan, Z. Feng, W. Ni, Z. Wei, R. P. Liu and C. Xu, "Connectivity of UAV Swarms in 3D Spherical Spaces under (Un)intentional Ground Interference," *IEEE Trans. Veh. Technol.*, vol. 69, no. 8, pp. 8792-8804, Aug. 2020.

[66] M. Kim and J. Lee, "Outage Probability of UAV Communications in the Presence of Interference," *IEEE Global Commun. Conf. (GLOBECOM)*, pp. 1-6, Dec. 2018.

[67] Ermolova, Natalia Y. and Olav Tirkkonen. "Using Beta Distributions for Modeling Distances in Random Finite Networks." *IEEE Commun. Letters*, vol. 20, no. 2, pp. 308-311, Feb. 2016.

[68] The Wolfram Functions Site, 2020. [Online]. Available: http://functions.wolfram.com

[69] M. K. Simon and M.-S. Alouini, *Digital Communication over Fading Channels*, 2nd ed. New York: Wiley, 2005.

[70] B. Ji, Y. Li, B. Zhou, C. Li, K. Song and H. Wen, "Performance Analysis of UAV Relay Assisted IoT Communication Network Enhanced With Energy Harvesting," IEEE Access, vol. 7, pp. 38738-38747, Mar. 2019

[71] L. Yang, F. Meng, J. Zhang, M. O. Hasna and M. Di Renzo, "On the Performance of RIS-Assisted Dual-Hop UAV Communication Systems," *IEEE Trans. Veh. Technol.*, doi: 10.1109/TVT.2020.3004598, Jun. 2020

[72] Y. Chen and C. Tellambura, "Distribution functions of selection combiner output in equally correlated Rayleigh, rician, and Nakagami-m fading channels," *IEEE Trans. Commun.*, vol. 52, no. 11, pp. 1948–1956, Nov. 2004.

[73] J. G. Proakis, *Digital Communications*, 3rd ed. New York: McGrawHill, 1995.

[74] R. Amer, W. Saad, B. Galkin and N. Marchetti, "Performance Analysis of Mobile Cellular-Connected Drones under Practical Antenna Configurations," in *IEEE Int. Conf. Commun. (ICC)*, pp. 1-7, Jul. 2020.

[75] X. Yuan et al., "Capacity Analysis of UAV Communications: Cases of Random Trajectories," *IEEE Trans. Veh. Technol.*, vol. 67, no. 8, pp. 7564-7576, Aug. 2018.

[76] M. Monemi and H. Tabassum, "Performance of UAV-Assisted D2D Networks in the Finite Block-Length Regime," *IEEE Trans. Commun.*, vol. 68, no. 11, pp. 7270-7285, Nov. 2020.

[77] W. K. New, C. Y. Leow, K. Navaie, Y. Sun and Z. Ding, "Interference-Aware NOMA for Cellular-Connected UAVs: Stochastic Geometry Analysis," *IEEE J. Sel. Areas Commun.*, vol. 39, no. 10, pp. 3067-3080, Oct. 2021.

[78] M. Ahsanullah, V. Nevzorov and M. Shakil, *An Introduction to Order Statistics*. Atlantis Press, 2013.

[79] A. Papoulis and S. U. Pillai, "*Probability, Random Variables, and Stochastic Processes*," Boston: McGraw Hill, 2002.

[80] M. Haenggi, "On distances in uniformly random networks," *IEEE Trans. Inf. Theory*, vol. 51, no. 10, pp. 3584-3586, Oct. 2005.